

Spray-flame-synthesized $\text{LaCo}_{1-x}\text{Fe}_x\text{O}_{3\pm\delta}$ perovskites for electrocatalysis

Von der Fakultät für Ingenieurwissenschaften, Abteilung Maschinenbau und
Verfahrenstechnik der

Universität Duisburg-Essen

zur Erlangung des akademischen Grades

eines/einer

Doktors der Ingenieurwissenschaften

Dr.-Ing

genehmigte Dissertation

von

Baris Alkan

aus

Ankara

Gutachter: Prof. Dr. Christof Schulz

Gutachter: Prof. Dr. Martin Muhler

Tag der mündlichen Prüfung: 04.06.2020

Parts of this thesis have already been published:

B. Alkan, S. Cychy, S. Varhade, M. Muhler, C. Schulz, W. Schuhmann, H. Wiggers, C. Andronescu, Spray-flame synthesized $\text{LaCo}_{1-x}\text{Fe}_x\text{O}_3$ perovskite nanoparticles as electrocatalysts for water and ethanol oxidation, *ChemElectroChem* 6, 4266-4274 (2019).

D. Waffel, B. Alkan, Q. Fu, Y. T. Chen, C. Schulz, H. Wiggers, M. Muhler, B. Peng, Towards mechanistic understanding of liquid-phase cinnamyl alcohol oxidation with tert-butyl hydroperoxide over noble-metal free $\text{LaCo}_{1-x}\text{Fe}_x\text{O}_3$ perovskites, *ChemPlusChem* 84, 1155-1163 (2019).

B. Alkan, D. Medina, J. Landers, M. Heidelmann, U. Hagemann, S. Salamon, C. Andronescu, H. Wende, C. Schulz, W. Schuhmann, H. Wiggers, Spray-flame made $\text{LaCo}_{1-x}\text{Fe}_x\text{O}_3$ perovskite nanoparticles as active OER catalysts: Influence of Fe content and low-temperature heating, *ChemElectroChem*, (2020), accepted.

Contents

Abbreviations.....	iv
Physical Symbols	vi
Abstract / Kurzzusammenfassung	1
1 Introduction.....	3
2 Background.....	5
2.1 Perovskite type structures.....	5
2.1.1 Single and double perovskites.....	6
2.1.2 Oxygen-deficient and layered perovskites	8
2.1.3 Surface properties of perovskite type structures.....	9
2.2 Transition metal-based oxides and perovskites as oxidation catalyst.....	10
2.2.1 Perovskites as water oxidation catalyst	11
2.2.2 Perovskites as ethanol oxidation catalysts.....	14
2.3 Spray-flame synthesis of nanoparticles.....	16
3 Analytical Methods	22
3.1 ATR-FTIR spectroscopy	22
3.2 X-ray diffraction.....	24
3.3 X-ray photoelectron spectroscopy	26
3.4 Transmission electron microscopy.....	27
3.5 Mößbauer spectroscopy.....	28
3.6 Brunauer-Emmett-Teller analysis.....	30
3.7 Linear sweep and cyclic voltammetry, rotating disk electrode measurements	30
4 Experimental Procedure.....	33
4.1 Spray-flame synthesis of the $\text{LaCo}_{1-x}\text{Fe}_x\text{O}_{3\pm\delta}$ perovskites.....	33
5 Results and Discussion	35
5.1 Materials characterization of as-prepared $\text{LaCo}_{1-x}\text{Fe}_x\text{O}_{3\pm\delta}$ nanoparticles.....	35
5.1.1 Qualitative phase analyses	35
5.1.2 Particle size and distribution, atomic structure and bulk composition.....	36
5.1.3 Surface chemical structure, composition and oxidation states	40

5.1.4	Electrocatalytic activity for water and ethanol oxidation	42
5.1.5	Operando electrochemistry/ATR-FTIR measurements	44
5.2	Investigation of the spray-flame process parameters	46
5.2.1	Correlation of spray-flame synthesis parameters and phase purity	47
5.2.2	The heat-treated $\text{LaCo}_{1-x}\text{Fe}_x\text{O}_3$	51
5.3	High-purity as-prepared and heated $\text{LaCo}_{1-x}\text{Fe}_x\text{O}_{3\pm\delta}$ nanoparticles	71
5.3.1	As-prepared $\text{LaCo}_{1-x}\text{Fe}_x\text{O}_3$ perovskites	73
5.3.2	Heat-treated $\text{LaCo}_{1-x}\text{Fe}_x\text{O}_3$ perovskites	76
5.3.3	Comparison of the OER activity of as-prepared and heated perovskites	84
6	Outlook	88
7	Summary and Conclusions.....	90
8	References.....	93
9	Appendix	103
9.1	Characterization results.....	103
Acknowledgement		112

Abbreviations

A.C.	Anodic current
ATR-FTIR	Attenuated total reflectance Fourier transformed infrared radiation
AFM	Antiferromagnetic
BET	Brunauer-Emmett-Teller
C.C.	Cathodic current
CV	Cyclic voltammetry
d-spacing	Interplanar spacing
DG	Dispersion gas
DSC	Differential scanning calorimetry
ECSA	Electrochemical surface area
EDX	Energy dispersive X-ray spectroscopy
EHA	2-Ethylhexanoic acid
EtOR	Ethanol oxidation reaction
FWHM	Full width half maximum
GSAS	General structure analyses system
HER	Hydrogen evolution reaction
HAADF	High annular angular dark field
HRTEM	High-resolution transmission electron microscopy
ICSD	International crystal structure database
LCO	LaCoO ₃
LEIS	Low energy ion spectroscopy
LSV	Linear sweep voltammetry
OER	Oxygen evolution reaction
OCP	Open circuit potential
ORR	Oxygen reduction reaction
PXRD	Powder X-ray diffraction
PFR	Precursor flow rate
RDE	Rotating disk electrode
RDS	Rate-determining step

RHE	Reversible hydrogen electrode
RP	Ruddlesden-Popper
RUB	Ruhr-Universität Bochum
QMS	Quadrupole mass spectroscopy
SAED	Selected area electron diffraction
SG	Space group
STEM	Scanning transmission electron microscopy
TEM	Transmission electron microscopy
TGA	Thermogravimetric analyses
WE	Working electrode
XPS	X-ray photoelectron spectroscopy
XRD	X-ray diffraction
VESTA	Visualization for electronic and structural analysis
V_{RHE}	Reversible hydrogen electrode potential

Physical Symbols

δ	Extent of oxygen vacancy, isomer shift in Mößbauer spectroscopy
e_g	Twofold degenerate and higher energy state forming after d-orbital splitting
i_s	Surface area-normalized kinetic current density, specific activity
n_{mono}	Amount of an adsorbed monolayer of gas on the materials surface
h	Plank's constant
ν	Photon frequency
ϕ	Work function, the minimum amount of energy required to induce photoemission of electrons from a specific metal surface
E_b	Binding energy
H	Magnetic hyperfine field
γ	Gamma radiation
ΔE_Q	Quadrupole splitting
ρ	Particle bulk density
a_g	Multiplication of the adsorbed gas amount by the area occupied by one adsorbed gas molecule
A_{BET}	Brunauer-Emmett-Teller surface area
C_{DL}	Double layer capacitance
R	Solution resistance
ν	Potential scan rate
i	Current
C_s	Specific capacitance
χ	Goodness of fit
σ_g	Geometric standard deviation
d_p	Count mean diameter

Abstract / Kurzzusammenfassung

This dissertation is based on experiments to research the potential of spray-flame-synthesized $\text{LaCo}_{1-x}\text{Fe}_x\text{O}_3$ perovskite as non-precious-metal based electrocatalysts towards OER and EtOR. These complex oxide perovskites were successfully synthesized before by numerous synthesis techniques such as the Pechini sol-gel method, co-precipitation, and reactive grinding; and Co- and Fe-based perovskites were put forward as highly active OER catalyst in numerous studies. However, few research studies were oriented to develop methods to produce high-surface area, nanosized perovskite catalysts that could be used in large-scale production. Therefore, the rationale behind this research is to show that spray-flame synthesis can be the suitable technique to produce high-surface area perovskite nanoparticles as electrocatalysts in a continuous scalable process. A series of $\text{LaCo}_{1-x}\text{Fe}_x\text{O}_3$ nanoparticles with different Fe contents were synthesized by spray-flame synthesis by varying process parameters and precursor solution compositions. With the aid of heat-treatment of the as-synthesized nanoparticles in O_2 , the physical properties of the as-synthesized nanoparticles were further modified. Comparative analyses on the bulk, surface, morphological, and magnetic properties of the perovskites were performed to determine the influence of Fe substitution on the OER catalytic activity.

All experiments and analyses are a result of the collaborative research study of several research groups; namely, the synthesis and materials characterizations by the author in collaboration with the Interdisciplinary Center for Analytics on the Nanoscale (ICAN) and the Wende group in the University of Duisburg-Essen. Electrochemical and *operando* electrochemistry investigations were performed in the Schuhmann and Muhler Groups at the Ruhruniversität Bochum. Based on this collaborative effort, spray-flame synthesis, nanoparticle characterization, and the investigation of the OER and EtOR catalytic activity of Fe-substituted LaCoO_3 nanoparticles was combined with *operando* electrochemistry/ATR-FTIR measurements giving insight into the influence of Fe substitution on electrochemical properties of LaCoO_3 . The focus of this work is on optimizing of spray-flame synthesis parameters and heat treatment processes for improving the stoichiometric perovskite phase content while decreasing carbon contamination. Overall, the synthesis and analyses methodology, applied for the specific materials system of $\text{LaCo}_{1-x}\text{Fe}_x\text{O}_3$ perovskites in this dissertation, was intended to be made useful for a wide range of other spray-flame made perovskites and complex oxide nanoparticles for electrocatalytic and other catalytic applications.

Diese Dissertation basiert auf Experimenten zur Erforschung des Potenzials der Sprayflammensynthesen zur Herstellung von $\text{LaCo}_{1-x}\text{Fe}_x\text{O}_3$ Perowskit als Elektrokatalysatoren auf Nicht-Edelmetallbasis für Sauerstoffevolutions- (OER) und Ethanoloxidations-Reaktionen (EtOR). Diese komplexen Oxid-Perowskite wurden zuvor bereits durch zahlreiche Synthesetechniken wie die Pechini-Sol-Gel-Methode, Kofällung und reaktive Mahlverfahren hergestellt, Co- und Fe-basierte Perowskite wurden dabei in zahlreichen Studien als hochaktive OER-Katalysatoren erkannt. Nur wenige Studien waren jedoch darauf ausgerichtet, eine Methode zur Herstellung von nanoskaligen Perowskit-Katalysatoren mit großer spezifischer Oberfläche zu entwickeln, die auch in der Großproduktion eingesetzt werden können. Daher ist der Grund für diese Forschung, zu zeigen, dass die Sprayflammensynthese geeignet ist, um Perowskit-Nanopartikel als Elektrokatalysatoren in skalierbaren Verfahren herzustellen. In diesem Zusammenhang wurde eine Reihe von nanopartikulären $\text{LaCo}_{1-x}\text{Fe}_x\text{O}_3$ Materialien mit unterschiedlichen Fe-Gehalten unter Verwendung verschiedener Sprayflammen-Prozessparameter und Prekursor-Lösungszusammensetzungen synthetisiert. Durch Temperaturbehandlung der synthetisierten Nanopartikel in O_2 wurden die physikalischen Eigenschaften der erzeugten Nanopartikel weiter modifiziert. Es wurden vergleichende Analysen der Volumen-, Oberflächen-, morphologischen und magnetischen Eigenschaften der Perowskite durchgeführt, um den Einfluss der Fe-Substitution auf die katalytische Aktivität der LaCoO_3 -Perowskite in OER zu bestimmen.

Alle Experimente und Analysen in Kapitel 5 sind das Ergebnis der gemeinsamen Forschungsarbeit mehrerer Arbeitsgruppen, nämlich der Synthese- und Materialcharakterisierung durch den Autor in Kooperation mit dem Interdisziplinären Zentrum für Analytik auf der Nanoskala (ICAN) und der Gruppe von Prof. Dr. Wende an der Universität Duisburg-Essen, sowie der elektrokatalytischen und operando elektrochemischen Untersuchung in den Gruppen von Prof. Dr. Schuhmann und Prof. Dr. Muhler an der Ruhruniversität Bochum. Darauf aufbauend wurden Sprayflammensynthese, Nanopartikelcharakterisierung, die OER- und EtOR-katalytische Aktivität von Fe-substituierten LaCoO_3 -Nanopartikeln mit Operando-Elektrochemie/ATR-FTIR-Messungen kombiniert und ein Einblick in den Einfluss der Fe-Substitution auf die elektrochemischen Eigenschaften von LaCoO_3 gegeben. Ein Schwerpunkt der Arbeit ist die Optimierung der Sprayflammensynthese und der thermischen Nachbehandlung zur Verbesserung des Anteils der stöchiometrischen Perowskitphasen im Produkt bei gleichzeitiger Verringerung der Kontamination mit Kohlenstoff. Insgesamt wurde die Synthese- und Analysemethodik, die für das spezielle Materialsystem der $\text{LaCo}_{1-x}\text{Fe}_x\text{O}_3$ Perowskite in dieser Dissertation angewandt wurde, für eine breite Palette anderer Perowskiten und komplexer Oxid-Nanopartikel aus der Sprayflammensynthese für elektrokatalytische und andere katalytische Anwendungen ertüchtigt.

1 Introduction

One of the most critical technological priorities of today is related to the transition from conventional fossil fuel-based energy resources to renewable energy resources such as hydropower, solar, wind, bio-energy and geothermal. The increasing demand for renewable energy sources are mainly due to fossil fuels are limited resources of fossil fuels and the emission of carbon dioxide from the combustion of fossil fuel leading to an increase in global warming. Yet, since the renewables in energy supply have intermittent natures, the development of energy conversion and storage technologies is needed to make renewable energy resources substitute for fossilized sources in terms of energy supply at reasonable costs. The important driver for utilizing electrochemical conversion technologies is mainly associated with the environmentally friendly and sustainable hydrogen production. When produced electrochemically, hydrogen is considered a promising energy carrier. In order to produce hydrogen in an economical way, electrolytic water-splitting, also known as water electrolysis, plays a key role as it allows production of molecular hydrogen directly from water under the driving force of electrical energy coming from renewables. Yet, efficiency of hydrogen production from water diminishes significantly due to the thermodynamic potential requirement for the other half reaction, namely the oxygen evolution reaction. To cope with this limitation, substituting water with more oxidizable chemical species, such as ethanol or ammonia, has been suggested. More importantly, new heterogeneous oxidation catalysts with large specific surface area are continually developed with the use of nanotechnological methods to increase the kinetics of the oxygen evolution reaction.

Among newly developed electrocatalytic nanomaterials, transition metals and their oxides are regarded as promising candidates. The main reason is that they have been found to lie at the top of the volcano-shaped curves, meaning they satisfy the optimal bond strength between metal and oxygen needed for oxidation catalysis. Lately, perovskite- and spinel-structured transition metal-based oxides have been considered promising electrocatalysts for water oxidation reaction. Thanks to their flexible crystal and electronic structures together with their chemical versatility, perovskites and spinels have shown the ability to preserve different oxidation states of transition metals and thus to uncover novel oxidation properties while keeping their structural stability.¹ The controlled synthesis of the above-mentioned oxidation catalysts with improved catalytic activity based on transition metals is also essential and necessitates the synthesis of high surface area nanosized particles of possible candidate materials. Spray-flame synthesis is, in this sense, a well-developed method to produce catalytically active nanoparticles using cost-effective precursors². This technology allows tuning the properties of catalysts such as composition, particle size, and morphology over a wide range and in a controlled way and therefore being an appropriate synthesis method for developing new catalytic materials.

For electrochemical applications, it was already demonstrated that particle sizes down to 10 nm can be obtained for Pd-doped LaCoO₃ perovskites by spray flame synthesis.³ Compared to the catalyst prepared by impregnating Pd into LaCoO₃, spray-flame made Pd-doped LaCoO₃ were shown to be more active and selective catalysts for converting NO_x from lean-burn systems to N₂ gases by using H₂ as a fuel.⁴ Besides that, using an acetylene/O₂ flame instead of methane/O₂ flame, the synthesis of complex perovskite compositions was also achieved for developing cathode materials for intermediate temperature solid oxide fuel cells.⁵ E.g., highly phase pure La_{0.6}Sr_{0.4}Co_{0.2}Fe_{0.8}O_{3-δ} and Ba_{0.5}Sr_{0.5}Co_{0.8}Fe_{0.2}O_{3-δ} perovskite nanoparticles were documented in a single-step spray-flame synthesis. In another study,

$\text{La}_{0.6}\text{Sr}_{0.4}\text{CoO}_3$ perovskite nanoparticles down to 17 nm were synthesized successfully with spray-flame synthesis.⁶ Spray-flame synthesis is also often used to synthesize perovskites containing precious metal dopants. Among them, Pd-substituted LaFeO_3 , LaMnO_3 , and Pd-supported $\text{YFeO}_{3+\delta}$ catalyst were synthesized with this synthesis method for methane oxidation.^{7,8} In the case of Pd-supported $\text{YFeO}_{3+\delta}$, it was observed that the flame-made catalyst improved the catalytic activity for CH_4 oxidation compared to the particles obtained by wet-chemical synthesis. Recently, thin-film deposition of $\text{La}_{0.6}\text{Sr}_{0.4}\text{CoO}_3$ perovskites was also successfully achieved. The deposited films were characterized to be amorphous and shown to transform into pure, crystalline $\text{La}_{0.6}\text{Sr}_{0.4}\text{CoO}_3$ phase after post-treatment at 700°C .⁹

Perovskite oxide nanocatalysts mentioned above are mostly produced by wet-chemical synthesis, such as sol-gel method and co-precipitation, as well as via solid-state synthesis like reactive grinding. For wet chemical techniques, several conditioning steps such as washing, filtering, drying, high calcination temperatures are required to produce the desired crystalline phase of nanoparticles. In solid-state reactions, intensive milling, grinding steps, and calcination are required. In both methods, high-temperature calcination treatment to produce phase-pure nanoparticles often causes sintering of nanoparticles and hence a lower surface area of the related nanocatalysts.¹⁰ More importantly, in the case of perovskites, widely used A-site ions such as Ba, Sr, and La ions can easily form carbonates during calcination which then can block catalytic sites of nanoparticles for catalytic applications. In this regard, spray-flame synthesis exhibits clear advantages in the fabrication of perovskite nanoparticles as it allows the synthesis of nanoparticles with well-controlled composition and size down to 10 nm without subsequent calcination.¹¹ This technology also makes the choice of constituents broadly variable and provides the possibility to adjust a desired elemental composition prior to nanoparticle formation. Moreover, it allows the modification of the oxidation state of the transition metals to a certain extent.¹² Therefore, the developments in the spray-flame synthesis of nanoparticles offer high potential for transition metal based catalysis applications.

Using Co- and Fe-based perovskite nanoparticles as oxidation catalysts has been widely researched in the catalytic field. However, synthesis of these materials using spray-flame technique is rare and requires a systematic research. The studies of Chiarello et al. have set the basis for understanding the influence of spray-flame process parameters on a test catalyst of LaCoO_3 nanoparticles. Building on all of this knowledge, the main objective in this thesis is to synthesize $\text{LaCo}_{1-x}\text{Fe}_x\text{O}_3$ nanoparticles in spray-flames. In this context, the acetate-based precursor salts were used for the synthesis of perovskite nanoparticles as these precursors showed promising properties in the literature. Also, the focus is given on the optimization of process parameters and solvent characteristics in order to obtain as-prepared nanoparticles with high phase purity. The second objective of this thesis is to explain the influence of Fe substitution on the crystal, magnetic and particle properties of LaCoO_3 perovskites. Due to limited literature data concerning the surface characterization of spray-flame made LaCoO_3 , the examination of surface composition and oxidation states of transition metals of these perovskites were particularly concentrated in this thesis. Together with that, the final objective in this thesis is to relate the physical properties of $\text{LaCo}_{1-x}\text{Fe}_x\text{O}_3$ catalyst to their catalytic properties in order to develop highly active nanocatalysts in incoming studies.

2 Background

2.1 Perovskite type structures

The name “perovskite” originally refers to a mineral deposit found in the Ural Mountains and corresponds to the parent compound of a large structural family. These minerals consist of natural perovskite crystals found to have an orthorhombic crystalline structure and they obey to the general chemical formula ABX_3 , where X is usually an anion, whereas A and B typically correspond to large and small cations, respectively.¹³ One of the key properties of these structures is that they can host a great variety of elements as shown in Figure 1. High chemical versatility in the perovskites also allows derivation of many different perovskite crystal structures. Together with them, proper tailoring of the oxidation state in the A-, B- and X-site elements also reveal the distinct electronic structures for these compounds and thus making them a promising material for electronic and magnetic applications.¹⁴

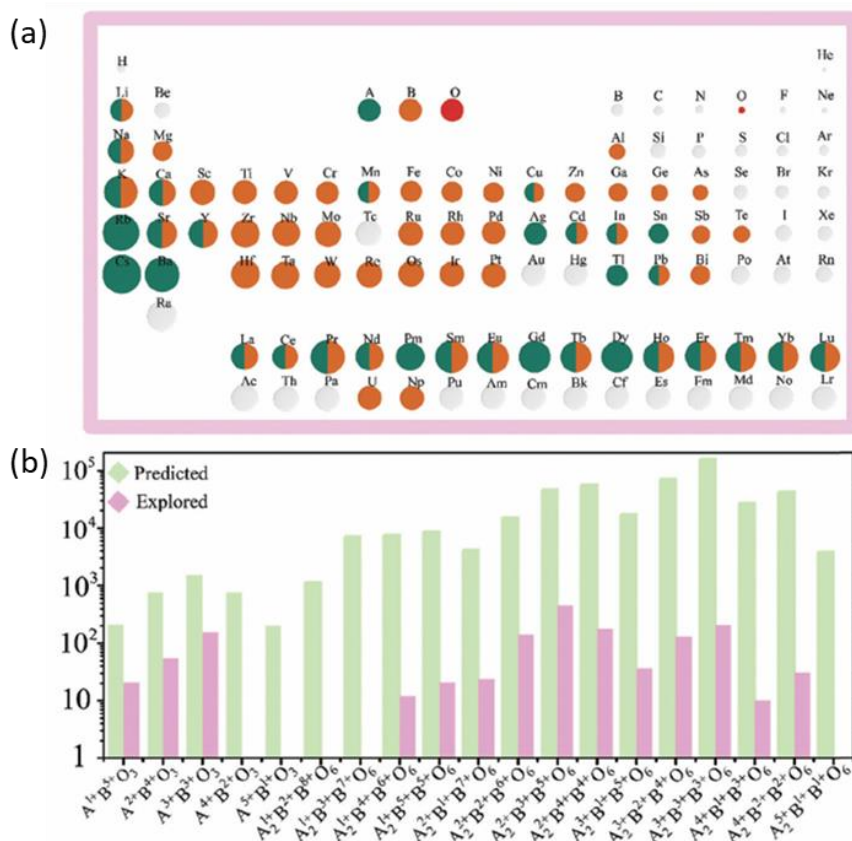


Figure 1: a) Elements that can occupy A, B, and O sites of perovskites. b) Ideal (predicted) and experimentally synthesized (explored) amounts of A- and B-site cations in single and double perovskites.¹⁴

Most recently, oxide perovskites (ABO_3) have been intensively investigated for energy-related applications such as photovoltaics, catalysis, and fuel cells.¹⁵ Especially, the use of nanotechnology and the replacement of rare earth metals with transition metal based elements offer potential for perovskite materials. In this regard, focusing more on the catalytic application of transition metal perovskite, this thesis concentrates on the understanding of the structural and chemical properties of La-, Co-, and Fe-based

perovskites in Chapter 2.1.1. After this background, the potential use of these perovskite in catalysis is presented. Finally, this chapter emphasizes the key synthesis techniques suitable for developing advanced nanostructured perovskites.

2.1.1 Single and double perovskites

The ideal perovskite structure is demonstrated in Figure 2a.¹³ It is a cubic structure, which consists of corner-sharing octahedra [BO₆] and A-site cations accommodating within the cuboctahedral vacancies between the octahedra. Inside the octahedra, B-site cations are surrounded by six oxygen ions in the unit cell structure as given in Figure 2b. The ideal cubic perovskites are usually stable at temperatures higher than 1000 K. Closer to room temperature, the cubic perovskite structure is not stable and transforms to lower-symmetry structures due to distortions occurring in the octahedral geometry.¹⁴ More specifically, the octahedra in perovskites show distorted geometries in three major ways. In the first case, when the B-site cations have too small size, they show atomic displacement within the octahedra but this does not cause a change in octahedral geometry. In the second case, when A-site cations are too small, octahedra tend to rotate or tilt while still preserving their geometry. In the last case, the electronic interaction between cation and anions within perovskite leads to octahedral distortion and this interaction is called Jahn-Teller effect. Overall, controlled tuning of octahedral geometry and displacement of B-site cations make perovskite structures important in dielectric, magnetic, electric, thermal and optical applications such as piezoelectrics, photovoltaics, thermoelectrics, electrochromics, and catalytic applications.

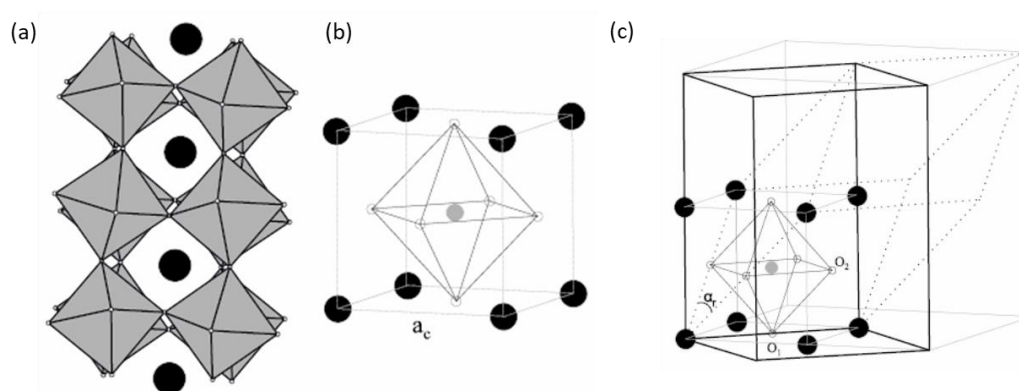


Figure 2: a) Corner-sharing CoO₆ octahedra with La ions (solid black circles). b), representative unit cell of cubic LaCoO₃ perovskite with lattice parameter a_c . c) and unit cells of rhombohedral (dotted lines) and monoclinic (solid lines) LaCoO₃ crystal structures.¹⁶

The abovementioned structural changes were investigated for a transition-metal based perovskites like LaCoO₃ perovskite. This perovskite has a cubic structure at temperatures above 1700 K.¹⁶ At lower temperatures, the CoO₆ octahedra tilt due to the small size of the La cations within the perovskite structure. Higher degree of octahedral tilting leads the CoO₆ octahedra to rotate and this rotation causes strain accumulation. Eventually, structural transition from higher-symmetry cubic structure (Space group: Pm-3m) to lower-symmetry rhombohedral structure (Space group: R-3c) occurs. For rhombohedral LaCoO₃ perovskite, the accumulated strain releases from the crystal structure by formation of twinned perovskite domains (Figure 3a), which are literately named as deformation twins. With the formation of deformation twins, some perovskite crystals preserve pseudocubic crystal structure and/or the superstructure of monoclinic domains (SG: I2/a).^{17,18} In monoclinic domains, together with the rotation/tilting of CoO₆

octahedra, orbital ordering mechanisms are considered to be active due to different Co–O bond lengths and therefore likely allow the short-range Jahn-Teller distortion.¹⁹ To illustrate, the representative TEM images of rhombohedral and monoclinic crystal structures are shown in Figure 3b and c, respectively.

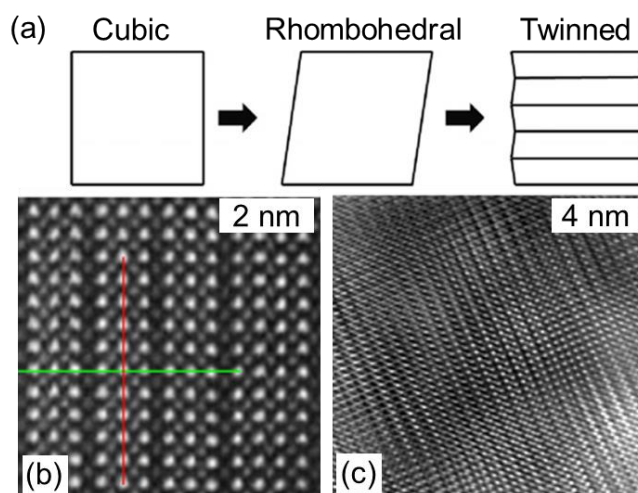


Figure 3: a) 2D scheme of cubic to rhombohedral transition and twinned formation.¹⁶ b) TEM image of rhombohedral LaCoO_3 domains with dark stripes owing to oxygen vacancies.²⁰ In-plane (green lines) and out-of-plane (red lines) La–La bond distances are indicated. c) TEM image of monoclinic $\text{La}_{0.5}\text{Sr}_{0.5}\text{Co}_{0.5}\text{Fe}_{0.5}\text{O}_{3-\delta}$ perovskite domains.¹⁷

In addition to single perovskites, double perovskites with the general formula $\text{A}'\text{A}''\text{B}'\text{B}''\text{O}_6$, have been also been investigated. Double perovskites form when other cationic substitutes incorporate into the perovskite structure. Because the ionic sizes of the substitutes usually mismatch with those of host cations in A- or B-sites, an additional strain energy evolves in such perovskite structures. To reduce this strain energy, also called Madelung energy, the cations tend to have an ordered arrangement within the structure. For instance, in the B-site substituted double perovskite, $\text{A}_2\text{B}'\text{B}''\text{O}_6$, the sublattices of the BO_6 octahedra are observed in three particular arrangements; namely, as rocksalt, layered and columnar order, which can be seen in Figure 4a.²¹ Formation of these ordered cationic arrangements lead to double perovskites to have different crystal symmetry and electronic structure than the single perovskites. With that, they offer a great potential to develop novel electronic and magnetic materials such as intrinsically active electrocatalysts, high performance magnetocaloric compounds.¹⁴

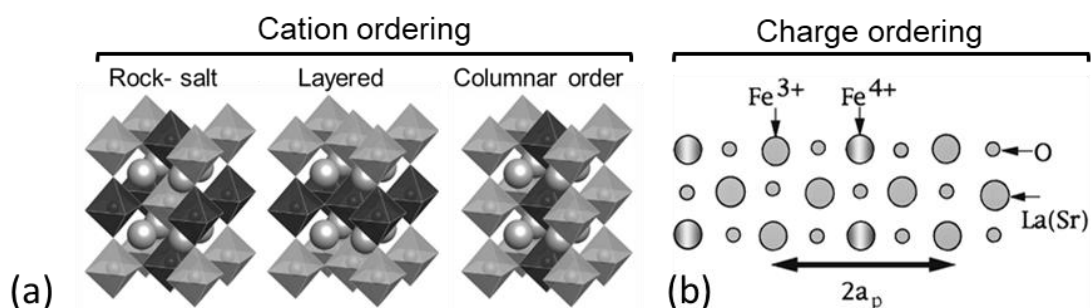


Figure 4: a) Three main cation ordering mechanism in B-site substituted double perovskites, $\text{A}_2\text{B}'\text{B}''\text{O}_6$.²¹ b) Scheme representing one possible charge ordering mechanism of Fe cations in $\text{La}_{1-x}\text{Sr}_x\text{FeO}_3$.²²

In addition to the cation ordering in the double perovskite, the transition-metal single perovskites can also show complex charge-ordering mechanisms. Figure 4b illustrates a proposed model of the ordered

arrangement of Fe^{3+} and Fe^{4+} ions in the charge-segregated regions of the $\text{La}_{1-x}\text{Sr}_x\text{FeO}_3$ perovskites at low Sr substitutions. It was stated that a sequence of charge ordering occurs between Fe^{3+} and $\text{Fe}^{4+}/\text{Fe}^{5+}$ ions depending on the content of Sr substitutes, which emphasizes flexible charge state of Fe cations in perovskites.²²

2.1.2 Oxygen-deficient and layered perovskites

Together with the cation and charge ordering, oxygen vacancy ordering is one of the most common ordering mechanisms in perovskites. Depending on the degree of oxygen vacancy, oxygen-deficient perovskite ($\text{ABO}_{3-\delta}$) and Brownmillerite ($\text{ABO}_{2.5}$ and $\text{ABO}_{2.67}$) structures are known. Beside them, structural ordering due to oxygen vacancies has been documented for layered perovskites like Ruddlesden-Popper structures with the general formula $\text{A}_{n+1}\text{B}_n\text{O}_{3n+1}$.^{13,23}

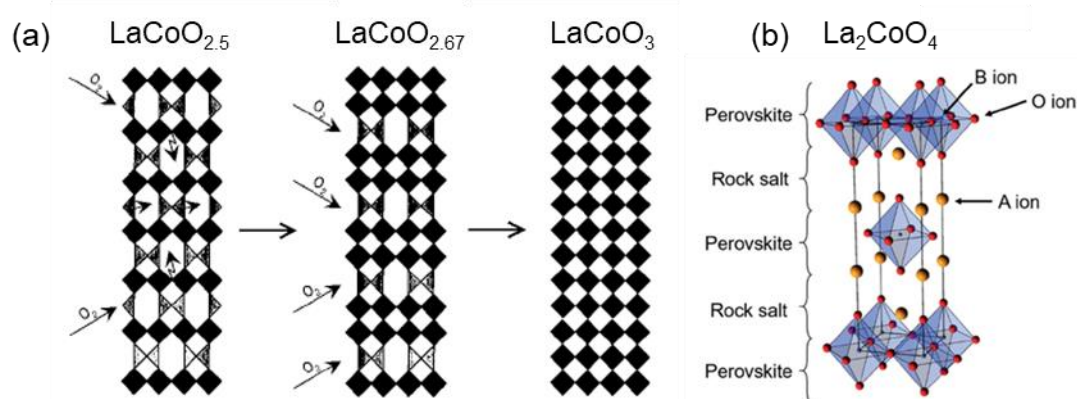


Figure 5: Oxidation of Brownmillerites (a, left, middle) to perovskites (a, right).²⁴ b) Illustration of one Ruddlesden-Popper type structure.²⁵

Oxygen-deficient perovskites preserve their perovskitic structure up to a certain degree of oxygen vacancies. When the concentration of oxygen vacancies is sufficiently high to form an ordered vacancy arrangement, perovskite crystalline structures transform to Brownmillerite type ones. Brownmillerites are made of one layer of the BO_6 octahedra connected with a layer of BO_4 tetrahedra as displayed in Figure 5. Oxygen vacancy ordering in these structures is usually stable from room temperature to 700°C . At higher temperature at ambient atmosphere, oxygen vacancy ordering begins to deform due to thermal effects and it results in the formation of mixtures of disordered and ordered oxygen vacancy states. Eventually, they fully oxidize to cubic perovskite above 900°C .^{13,26} Examples to these structures (La-Co-O type composition) include $\text{LaCoO}_{2.5}$ and $\text{LaCoO}_{2.67}$ compounds. A- and B-site substitution in Brownmillerite structures were also investigated previously. A-site cations having a valence state of 2+ (e.g., Sr^{2+} , Ca^{2+} , Ba^{2+}) and B-site cations having a valence state of 3+ (e.g., Co^{3+} and Fe^{3+}) were investigated. In the compounds having such cationic substitutions (e.g., $\text{Ca}_2\text{CoFeO}_5$), it was found that BO_4 tetrahedra are occupied by an ordered sequence of the Co^{3+} and Fe^{3+} ions while BO_6 octahedra contain random distribution of these cations.²⁷ When the oxidation state of Co ions is reduced to Co^{2+} as in LaSrCoFeO_5 , it was also asserted that high-spin Co^{2+} and Fe^{3+} ions only show random distribution at both tetrahedral and octahedral sites.²⁸

Another kind of perovskite-like structures that contain a high content of oxygen vacancies are Ruddlesden-Popper (RP) type structure. Their structure is comprised from alternating layers of cubic perovskite

and rocksalt structure as demonstrated in Figure 5b.²⁵ The layered arrangement of these structures allows oxygen ions to show high ionic conductivity. In cobalt based RP type structures, the La_2CoO_4 compound was shown to possess a high degree of bulk and surface oxygen vacancies.²⁹ The presence of vacant oxygen sites in their structure was also found to allow incorporation of hydrate, and $\text{PrSr}_3\text{Co}_{1.5}\text{Fe}_{1.5}\text{O}_8(\text{OH})_2$ was shown to have high hydration ability.³⁰ Having a layered structure with tunable oxygen vacancy content, RP type compounds are mostly investigated as mixed ionic-electronic conducting oxides and electrocatalysts.³¹

In addition to the abovementioned structures, La-deficient perovskite-like structures, which contain Co and Fe ions in B sites, were also researched as catalysts for Fischer-Tropsch synthesis. These compounds preserve a cubic crystalline structure owing to deficiency of La ions. The influence of La stoichiometry in Co- and Fe based perovskites was examined in a systematic way, and the findings reveal that surface reconstruction in La-deficient perovskites plays a key role in their high resistance to deactivation for catalytic processes.³²

Following structural details of the most widely studied perovskite crystals; the next part is focused on critical surface properties of the Co- and Fe-based perovskite compounds, which have high potential as oxidation catalysts.

2.1.3 Surface properties of perovskite type structures

Compared to the bulk properties, surface properties of perovskite crystals show notable differences at nanoscale. For example, coordination of cation polyhedra, composition and structural ordering can vary from the bulk to surface regions of perovskite nanoparticles. These variations can lead to surface segregation of some species or surface formation of phases to occur in them. Beside them, octahedral tilting in perovskite crystals can occur at perovskite surfaces to a large extent while it is rather limited in the bulk due to close-packed crystal structure. Therefore, the extent of strain at the surface of perovskite nanoparticles becomes an important parameter affecting catalytic activities of perovskite nanoparticles.

To determine surface termination and subsurface compositions in perovskites, surface-sensitive measurements techniques such as low energy ion spectroscopy (LEIS) depth profiling were applied to $\text{La}_{0.6}\text{Sr}_{0.4}\text{Co}_{0.2}\text{Fe}_{0.8}\text{O}_{3-\delta}$ single perovskites, $\text{GdBaCo}_2\text{O}_{5\pm\delta}$ double perovskite and $\text{La}_2\text{NiO}_{4+\delta}$ RP type perovskites.³³ All of these perovskite-like structures show critical surface reconstructions of the cations when they are exposed to thermal treatments. More specifically, their outermost surfaces tend to terminate with AO planes like LaO, SrO. Surface segregation of the A-site ions causes the enrichment of B-site cations in the subsurface of perovskites. Although B-site cations, catalytically active transition metal ions, do not have direct interactions with the reactants, these perovskites still exhibit high activity towards catalytic reaction such as oxygen reduction reaction (ORR). These findings were explained by the presence of surface anion defects in the segregated A-site cations, which enable interaction of B-site cations in the subsurface with the reactants. In addition, the extent of surface reorganization was shown to be controllable when nanoparticles were grown from a backbone perovskite support having initially non-stoichiometric composition.³⁴ For instance, in a reducing environment, controlled exsolution of the B-site cations from perovskite-like nanoparticles surface is shown in Figure 6b.

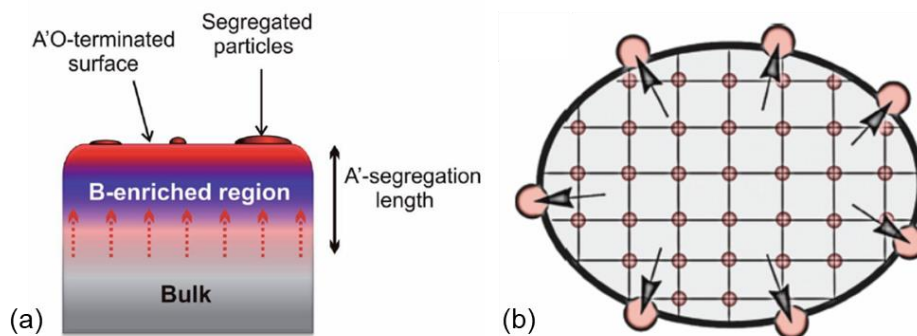


Figure 6: a) Scheme indicating both the compositional variances from the bulk to the surface region of perovskite ceramics and segregated particles.³³ b) The representative scheme showing exsolution of B-site cations (large circles) from $A_{1-x}BO_{3-\delta}$ perovskite nanoparticles (B-site rich) during their growth in a reducing atmosphere.

Another critical surface parameter regarding the catalytic activity of La-Sr-Co-Fe based oxygen-deficient perovskites is the lattice oxygen near the perovskite surface. With use of *in situ* X-ray absorption spectroscopy (XAS), the surface electronic structure of these perovskites was analyzed, and the analyses indicate the significance of the localized electronic state on the surface lattice oxygen. Together with B-site cations over which the redox reaction usually takes places, the surface lattice oxygen in oxygen-deficient perovskite ($ABO_{3-\delta}$) was additionally identified as catalytically active sites for oxygen evolution.³⁵

In addition, lattice strain is also an important factor for explaining the different surface and bulk composition of perovskite oxides. To examine this effect, transition metal based $La_{0.7}Sr_{0.3}MnO_3$ films were tensile strained in a controlled way. It was observed that Sr segregation occurs at high lattice strain in the thin films, and the energy needed for Sr segregation reduces at increasing strain levels.³⁶ The influence of lattice strain on the electronic structure of perovskites was also reviewed in a previous report, and the mechanical stress introduced to perovskite was highlighted as a tool to change the energy landscape of the catalytic reaction by changing the enthalpy for oxygen defect formation and adsorption energy as well as migration, adsorption and charge transfer barriers.³⁷ Besides the elastic strain, the surface reactivity of perovskites in regard to their surface atomic structure was investigated in detail, being found to depend on highly flexible coordination of metal–oxygen polyhedra at perovskite surfaces.³⁸

2.2 Transition metal-based oxides and perovskites as oxidation catalyst

In this part, following the bulk and surface properties of perovskite-like compounds, their use as electrocatalyst is explained. First, the basic principles of electrochemical reactions are given, and the role of electrocatalysts are stated. Then, the perovskite materials having high potential as oxidation electrocatalyst are reviewed.

In general, apart from mixed ionic electronic conductors, electrochemical systems consist of an electron conductor and an ionic conductor, which are named electrode and electrolyte, respectively. Typically, two electrodes separated with one or more electrolyte phase are used for electrochemical cells. The electrode at which oxidation takes place is named anode, while the other electrode at which reduction take place is named cathode. When anode and cathode interact with an electrolyte, electron transfer can

spontaneously occur at the electrode/electrolyte interface, and it can be followed by the transport of electrons through an external circuit. Mechanistically, the elements having a high activity for oxidation undergo an oxidation reaction at the anode. Then, the electrons released from this reaction are transferred to the cathode and reduce elements at the cathode. At the same time, the released ionic species from the oxidation reaction move in the electrolyte medium to maintain charge neutrality. The electrochemical cells where such charge transfer reactions spontaneously occur are called galvanic cells. Their overall cell potential mainly depends on the electric potential difference at respective electrode/electrolyte interfacial reactions, and increasing magnitude of this potential difference controls the enhancement of charge-transfer rates.³⁹

In addition to spontaneous charge-transfer reactions in galvanic cells, electrochemical reactions can be realized with a consumption of a certain amount of electrical energy by supplying electrons to the respective electrode at an elevated potential through an external power supply. These reactions are called electrolytic reactions and the additional potential required to be applied over the thermodynamic potential energy is defined as the overpotential. A higher value of the overpotential is associated with slower kinetics of the electrolytic reactions.

One of the most widely researched electrolytic reaction, which is industrially critical for hydrogen production but suffers from high overpotential is the electrolysis of water forming molecular hydrogen and oxygen. Fundamentally, this reaction includes the occurrence of two half-cell reactions, namely the cathodic hydrogen-evolution reaction (HER) and anodic oxygen-evolution reaction (OER). Although both redox reactions are kinetically slow due to the high overpotential, the OER reaction has been considered as the major bottleneck because of the involvement of a high number of intermediate species of surface adsorbates and a four-electron process.^{40,41} Therefore, a great deal of research has been recently focused on the development and discovery of novel electrocatalyst to enhance the reaction kinetics of the OER.

2.2.1 Perovskites as water oxidation catalyst

Among the OER catalysts, IrO₂ and RuO₂ have been considered as the benchmark catalysts due to their high OER activity.⁴² In an acidic medium, these electrocatalysts require an overpotential of ~200 mV while they require ~300 mV in an alkaline medium which can be classified the lowest overpotentials for OER reactions.⁴³ Despite their low overpotential, scarcity and high cost of these metal catalysts constrains their applicability. Thus, the need for earth-abundant, cheap and active catalyst brought transition-metal-based oxides and perovskites to the forefront. As these oxides do not show high stability in acidic media, they are investigated for reactions in alkaline media. Recently, an OER reaction mechanism over transition metal-based oxide catalysts in alkaline media was proposed. The overall oxygen evolution reaction includes four major intermediate reactions as displayed in Figure 7. Firstly, hydroxylated B-site active sites in the alkaline medium (molecule at the top of Figure 7) deprotonates, and O²⁻ adsorbates form (step 1). Then, the B–O active sites are attacked by hydroxyl ions in alkaline media forming M–OOH oxyhydroxide adsorbates (step 2). Through proton-coupled electron transfer, the oxyhydroxide groups deprotonate leading to O₂²⁻ adsorption on the B-site cations (step 3). Finally, the adsorbed O₂²⁻ are released from B-site cations through an exchange with OH⁻ ions (step 4). Based on the overall OER reaction, it has been considered that formation of the O–O bond in the OOH adsorbates and the deprotonation of OOH by proton extraction are the rate-determining steps.^{44,45}

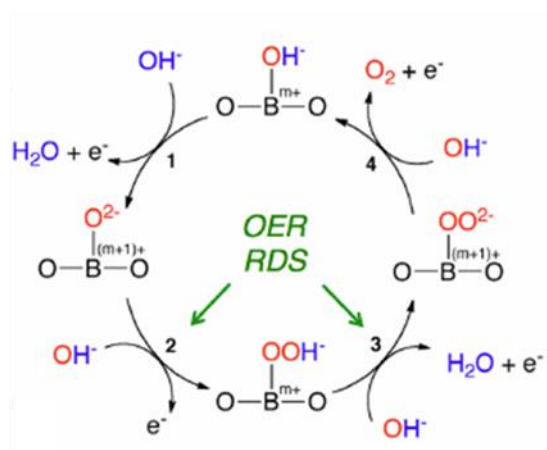


Figure 7: The proposed OER mechanism for perovskites⁴⁴, details see text.

In this respect, the bonding strengths of oxides or perovskites with OH and OOH radicals have been considered as one critical factor determining their catalytic activity towards OER.^{43,46} To illustrate the OER activity trends with respect to M–OH bond strengths, thin films of several transition metal-based oxides, namely CoO_x, NiO_x, FeO_x, and MnO_x, have been prepared by an anodic deposition method.⁴⁷ Partial substitution of the metal oxides having low M–OH bond strength (CoO_x and NiO_x) with those having strong M–OH bond strength (FeO_x and MnO_x) were shown as a methodology to tune M–OH bonds in a way to enhance the OER activities of these catalysts. Figure 8 indicates the drastic increase in the intrinsic OER activities of substituted mixed oxide catalysts, such as CoFeO_x and NiFeO_x, relative to unsubstituted FeO_x.

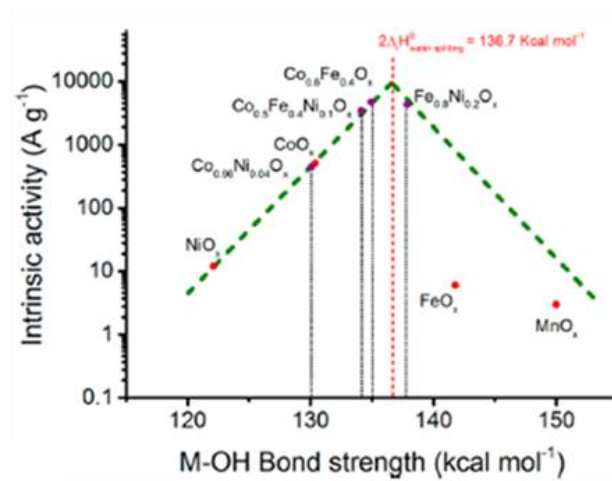


Figure 8: Dependence of intrinsic OER activity values of transition-metal-based oxides on the relative M–OH bond strength in both pristine and substituted form.⁴⁷

In addition to single oxides, transition metal-based perovskites have been largely researched as OER catalysts and several structure–property relations have been put forward.⁴⁸ One of the materials properties that is critical for these catalysts is the concentration of oxygen vacancies. For instance, partial substitution of La³⁺ ions by Sr²⁺ ions in the La_{1-x}Sr_xCoO_{3-δ} perovskites were observed to induce a notable increase in their OER activities at high Sr contents, and SrCoO_{2.7} perovskite were found as the most active OER catalysts, requiring even lower overpotentials than those of IrO₂ benchmark catalysts.⁴⁹ Such high OER activities of SrCoO_{2.7} perovskites were mainly related to the participation of lattice oxygen to

20 nm shows very high OER mass activities, which was superior to those of the IrO₂ benchmark catalysts. Therefore, the strategies to develop perovskite nanostructures at different morphologies and sizes also show high potential for improvement of their OER activities.⁵¹

In conclusion, transition-metal-based perovskites are promising oxidation catalysts towards OER when their structural and electronic properties are properly tailored. These materials also carry potential for other oxidation reactions such as alcohol oxidation. Especially, as being a model reaction of complex oxidation reaction like glycerol oxidation, ethanol oxidation has been recently investigated, and therefore the importance of this reaction and the conventional and potential catalysts used for it are summarized in the following section.

2.2.2 Perovskites as ethanol oxidation catalysts

As stated in the previous section, the water oxidation reaction inherently requires high overpotentials owing to its slow kinetics, and makes the hydrogen production by means of water electrolysis costly.⁴¹ Also, due to the fact that the overpotential is wasted on the formation of oxygen which is usually released to the atmosphere and does not inherently contribute with an economic value, the replacement of the OER with an alternative anode reaction carries potential. On the one hand, the alternative anode reaction should not only exhibit a lower overpotential than the OER with similar current densities to coupled hydrogen formation. On the other hand, the anodically formed product may possess a certain economic value and could be further used in chemical industry. In this regard, alcohol species are seen as potential substitute of water, since they have higher oxidation kinetics than water, and their oxidation products such as acetates and aldehydes can be of industrial relevance. Among alcohol species, ethanol is mostly regarded as suitable medium due to its low toxicity, renewable nature, high energy density and availability.^{52,53} In the oxidation reaction of ethanol, adsorption of hydroxyl ions on the electrocatalysts surface is considered the critical material property since it allows the further oxidation of intermediate species to final product, namely oxidation of aldehydes to acetates (see the proposed reaction mechanism of ethanol oxidation for alkaline environment in Figure 10).⁵⁴ In this respect, materials systems that enable the chemisorption of ethanol species and hydroxyl groups are essential in the electrocatalytic oxidation of ethanol.^{54,55}

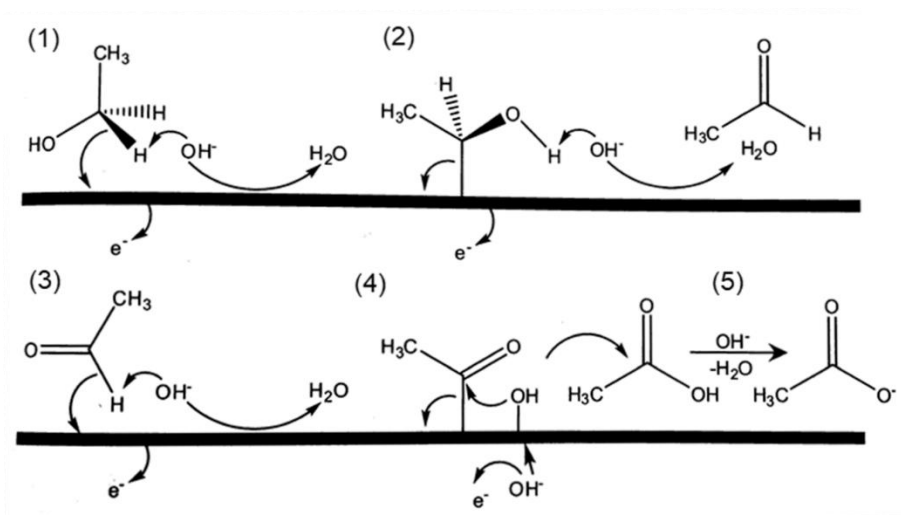


Figure 10: The scheme illustrating the mechanism of ethanol oxidation in alkaline media.⁵⁴ The typical reaction order is the following; (1) adsorption of free ethanol molecule to catalyst surface and its reaction with hydroxyl ions, delivering one e^- to the catalyst and releasing H_2O as byproduct, (2) further hydroxylation of the adsorbed ethanol molecule delivering one e^- to the catalyst and releasing H_2O , byproduct, thereby forming a free aldehyde molecule, (3) the adsorption of a free aldehyde to catalyst surface, delivering one e^- to the catalyst and releasing H_2O as byproduct (4) The adsorption of OH^- ions to the catalysts surface delivering one e^- and the reaction of adsorbed aldehydes with adsorbed hydroxyl at the catalyst surface to produce acetic acid, (5) the reaction of acetic acid with hydroxyl ions to produce acetate while releasing H_2O to the electrolyte.

As promising electrocatalysts, noble metals such as Pd and Pt typically show the highest catalytic activities toward ethanol oxidation, enabling this reaction at the potentials as low as 0.4 V vs. RHE.⁵⁶ Despite having clear advantage in terms of activity, these catalysts often suffer from poor stability and poisoning effects either by the formed CO or due to the formation of the corresponding metal oxide.⁵⁷ Alloying Pt and Pd with other metals,⁵⁶ or supporting them on suitable substrates⁵⁸ was performed aiming at improving the catalyst stability during the reaction, but despite this, only low current densities were achieved before poisoning of the electrocatalyst took place.⁵⁶ Besides the poor stability, the investigation and application of electrocatalysts using noble metals is not economically viable. Therefore, transition-metal oxides are investigated as alternative catalyst materials. To illustrate that, the ethanol electro-oxidation activity of a group of Ru-based perovskites was systematically examined, and the findings indicate promising catalytic activities of these materials with and without Pt loading.⁵⁵ It was stated in the same report that using perovskites as a supporting material reduces the required amount of Pt loading, making this materials system more economical compared to those of bimetallic catalysts. More recently, $SrCoO_{3-\delta}$ perovskite nanoparticles were combined with Pt catalysts, and the presence of the perovskites was found to significantly increase the oxidation of ethanol.⁵⁹ Therefore, synthesizing nanoparticles of perovskite and using them in nanocomposite structures were highlighted as important factors toward ethanol oxidation.

Overall, the synthesis of transition metal oxide-based perovskites in the nanosize regime was considered critical for perovskite catalysts to be used for water or ethanol oxidation. In this respect, spray flame synthesis is regarded as one of the most important techniques to produce these oxide nanoparticles. In this context, the following section explains basic principles of spray-flame synthesis and its importance in the field of catalysts development and production.

2.3 Spray-flame synthesis of nanoparticles

Spray-flame synthesis is a well-established method for production of oxide nanoparticles from the gas phase. It is based on three main processes, namely, transport of a (combustible) precursor solution to a flame, its combustion in the flame (flame temperatures range ~ 1200 - 2500 K), and the formation of nanoparticles from the precursor reagents through sequential particle nucleation in the gas phase and growth reactions⁶⁰. To put these processes into context, the following section firstly focuses on the burner design, operational aspects of the synthesis and fundamental chemical processes occurring during particle formation in flames. Then, the influence of spray-flame process parameters and precursor solution characteristics on the materials properties of the final product are briefly explained. In the end of this section, several examples of spray-flame made perovskite nanocatalysts are given.

The design of a standardized burner in the assembled form is demonstrated in Figure 11a.⁶¹ In this design, the liquid /precursor solution is delivered through a metal capillary such as a hollow needle (inner diameter of 0.4 mm). The needle is fitted to upper edge of the nozzle with aid of a fine screw (i) as indicated in Figure 11b. The position of the hollow needle is adjusted by 3 μm micrometer screws (ii) for ensuring symmetric flame conditions during operation. The annular slit surrounding the needle is used for the injection of the oxidizer gas (O_2), which has a flow velocity of about 100 m/s. This two-fluid spray nozzle is located in the center of a brass sinter plate (iv) having mean porosity about 60 μm . The sinter plate is used to support a premixed CH_4/O_2 pilot flame surrounded by a co-flow of nitrogen or oxygen for shielding the flame against the environment and stabilizing it as well as supporting the nanoparticles transport. For metering the respective flows to the burner, mass flow controllers (Bronkhorst) connected to a National Instruments Compact Field Point system are used. Analog voltage signals provided by this system is utilized to set and read-out the mass flow controllers. A short tube section (iii) is also used for separating the gas flows.

Figure 11c show the scheme of the spray flame synthesis with the SpraySyn burner.⁶² In the center of the burner, a removable two-fluid nozzle with external mixing is used to generate the spray. A metal capillary is used to supply the precursor dissolved in a combustible liquid with an exit velocity of 0.26 m/s, and a high-velocity flow of O_2 as dispersion gas is applied through the annular slit surrounding the capillary. The high relative velocity between the liquid and dispersion O_2 gas atomizes the liquid into the spray, and the spray forms the spray flame. The pilot flame supports the spray flame. The particle-laden exhaust gas is directed to a glass fiber filter, and the powder is harvested from the filter membrane. Figure 11d shows a CH_4/O_2 pilot flame and ethanol spray flame during the synthesis with the SpraySyn burner.

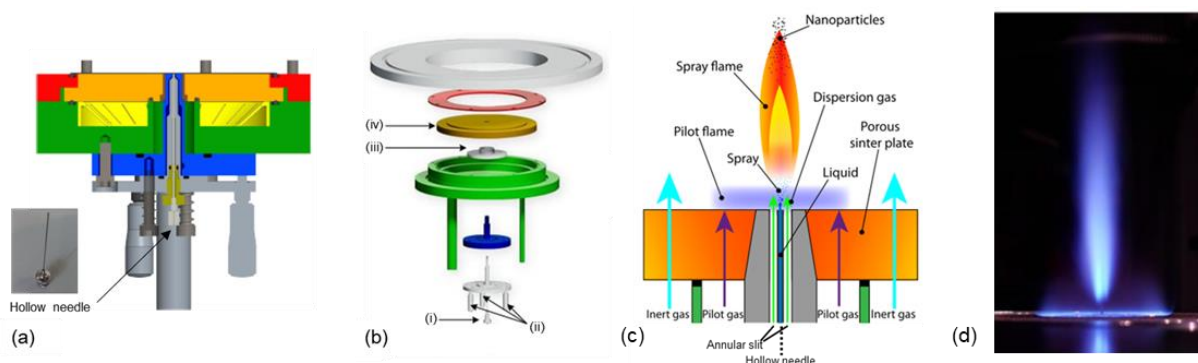


Figure 11: a) The schematic view of the standardized spray-flame synthesis burner and a metal capillary, b) The disassembled view of the burner with the components; (i) a fine pitch screw, (ii) three micrometer screws, (iii) a short tube section, (iv) a brass sintered plate. (c) The scheme of spray flame formation through SpraySyn burner (see text for details). d) The image shows a flat pilot flame of CH_4 and O_2 together with a spray flame of ethanol species.⁶³

The particle formation in the spray flame occurs by the two main reaction pathways; namely droplet-to-particle (intradroplet reactions) and gas-to-particle conversion^{60,64}. In the droplet-to-particle conversion, the solvent and precursor ligands in the precursor solution evaporate at flame temperatures leading to precipitation of solute in the droplets. This conversion process includes liquid/solid chemical reactions without any evaporation of metal precursor and formation of metal vapor. During and after the solvent evaporation, the solute precipitates undergo solid-state reactions and densification, namely coalescence and sintering, which determines the agglomeration state, size, and morphology of the primary nanoparticles. This conversion route is preferred when the precursors of the element being synthesized do not have a sufficiently high volatility to form gas-phase species. The particles formed by this route, in general, have the sizes higher than $0.1 \mu\text{m}$, being characterized in a highly agglomerated state. They also show hollow or highly porous particle morphology due to the poor control over particle formation during liquid-to-particle conversion. Therefore, this mechanism is not considered useful to produce nanosized particles suitable for the catalyst production.

In the gas-to-particle conversion, a volatile precursor intermediates are formed as a consequence of the high flame temperature when evaporation is faster than the above mentioned intra-droplet processes.⁶⁰ The chemical reactions creating new species or physical reactions like cooling that lower the vapor pressure of the gaseous species bring the species in a highly supersaturated state that drives the formation of particles by homogeneous nucleation. The nucleated particles grow through collision and solid-state reactions such as coalescence and sintering. At low particle concentrations in the flame, the primary particle sizes can be usually explained by a nucleation–condensation processes without critical coagulation. On the other hand, primary particle sizes strongly depend on the nucleation–coagulation processes at high particle concentrations, which govern their aggregation and agglomeration state. As gas-to-particle conversion includes the generation of particles from atomic/molecular species in the gas phase, it results in the generation of nanosized particles, which could show similar material characteristics.⁶⁰ This conversion mechanism is relevant for the production of nanosized catalyst materials, and thus will be mainly emphasized in the following sections.

High-purity nanoparticles with narrow particle distribution can be achieved in the gas-to-particle conversion process, but the production of multicomponent systems is a difficulty in this regime. The reason

is that reagents and/or intermediates used in the synthesis of multicomponent systems can be involatile in the gas-to-particle regime or they can have different reactivity and thermal decomposition temperatures. When reactivity and volatility of the reagents are unmatched, the individual reaction of each reagent independently takes place at different flame temperatures, which can cause formation of phase-segregated particles. The volatile intermediate of one reagent, which has higher volatility than other reagents, also form in the case when phase segregation occurs within a particle (see next paragraph for details) and the loss of these volatile intermediates can cause the formation of chemically inhomogeneous particles with incorrect stoichiometry. For instance, spray-flame made $\text{La}_{1-x}\text{Sr}_x\text{Co}_{1-y}\text{Fe}_y\text{O}_{3-\delta}$ perovskites contain $(\text{La}_{2-x}\text{Sr}_x)\text{CoO}_4$ type phases, and these La-rich secondary phases form due to the evaporation of Cobalt at high flame temperature, causing inaccurate stoichiometry in the as-prepared nanoparticles.⁵ Thus, the metal precursors containing the same ligands, the reagents and intermediates having similar thermal decomposition behavior and volatility while being phase miscible are preferred for the synthesis of phase-pure, homogeneous particles in multicomponent precursors.⁶⁰

The particle formation mechanism through the gas-to-particle conversion are generally classified in 6 main routes.⁶⁴ From the single metal precursors (route 1), crystalline simple oxide nanoparticles, such as Al_2O_3 , Fe_2O_3 , Co_3O_4 , can be produced with the formation of low amount of carbon soot on the particles under continuous and excess supply of O_2 gas to the flame and at high flame temperatures^{64,65}. In the case of incomplete combustion of all carbon species due to a lack of supplied O_2 and/or the use of inert gases surrounding the flame, carbonaceous layer could deposit on metal and block its oxidation during the synthesis.⁶⁶ This can lead to formation of metallic nanoparticles or metal oxide shell on metallic nanoparticles, as observed in the spray-flame made Co/CoO_x and Cu/CuO_x nanoparticles in the simple oxide systems.^{66,67} Beside the metal oxide encapsulation, coating of a secondary metal is possible in the multicomponent oxide system when sufficiently high amount of secondary metal is present to form a strong interfacial bonding with other metal oxide components (route 2). Otherwise, the phase segregation of secondary metal, such as Ru, Pd, Pt from the gas phase can take place, leading to their deposition and dispersion on the surface of the firstly nucleated oxide components (route 3). The formation of such supported metal oxide or metals usually occurs when metal precursors in the multicomponent system have different boiling points, which leads to their sequential nucleation and growth. The rapid quenching of the flame and short residence time of the particle in the flame allows preventing high degree of sintering in the solid-state reaction between the deposited and the supporting oxides.⁶⁴

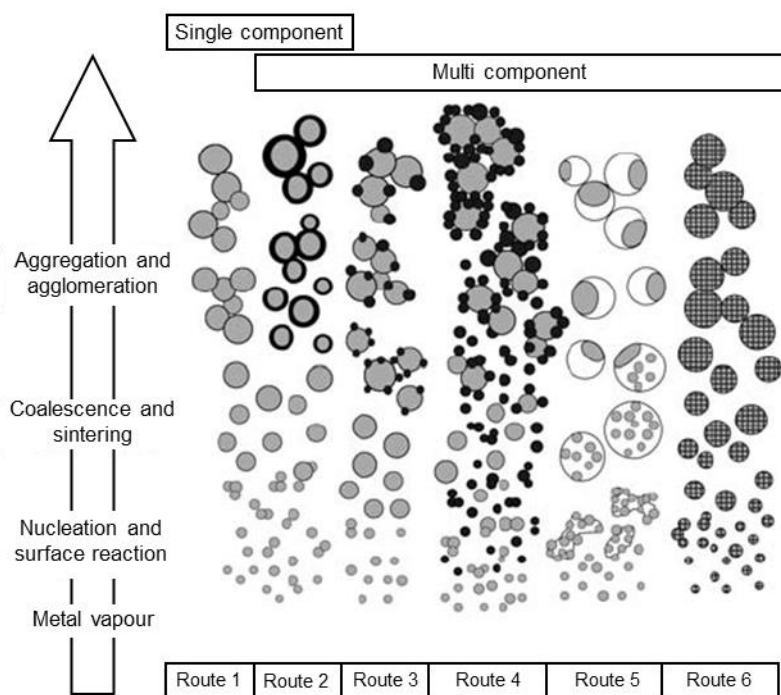


Figure 12: Scheme illustrating the main chemical reactions and particle formation mechanism in a spray-flame synthesis in gas-to-particle regime. The scheme is adapted from the previous report.⁶⁴

The miscibility degree between the segregated phases in multicomponent systems leads to other particle formation mechanism and morphologies as shown in Route 4-6. At low miscibility, only the physical inter-particle mixing between different particle phases can take place in the case that solid-state reactions are limited during spray-flame synthesis (route 4). More typically, phase segregation occurs within a host particle when the core and encapsulating host particle phases are completely immiscible and limited solid-state reactions (route 5). For highly miscible multi-component systems, a homogenous, intra-particle mixing of the single particle matrix can form (route 6). Within the particle matrix, the formation of a single phase (e.g., solid solutions) or multiphase crystallite structures (e.g., complex metal oxides, dispersed mixed oxides) can form⁶⁴. Particle formation in the complex metal oxides, substituted-doped systems (e.g., $\text{CoO}_x\text{-Al}_2\text{O}_3$ ⁶⁸, LaCoO_3 ³, MgAl_2O_4 ⁶⁹, $\text{Y}_3\text{Al}_5\text{O}_{12}$ ⁷⁰) show similarity to the particle formation mechanism in Route 6.⁶⁴

The abovementioned particle formation mechanisms during spray-flame synthesis inherently depend on the process parameters (e.g., O_2 and CH_4 flow rate for the pilot flame, velocity and mass flow of the O_2 dispersion gas, and the precursor flow rate)⁷¹ and the precursor characteristics (e.g., proper selection of precursor and solvent, the mixture of which have appropriate metal concentration, combustion enthalpies, decomposition temperatures).⁶⁴ The influence of most of these parameters on the spray-flame formation of LaCoO_3 perovskites has been empirically investigated in previous reports.^{2,72} The dependence of the particle properties on the individual effects is summarized in the following.

The feeding ratio of the CH_4 and O_2 in the pilot flame is one of the critical parameters adjusted for constant support of the spray flame. A previous report on the stability of cellular and laminar flat flames of premixed $\text{CH}_4+\text{O}_2+\text{CO}_2$ mixtures over porous plug burner show the varying structure of the pilot flame depending on the equivalence ratios.⁷³ In this report, formation of instable cellular flame was

observed at fuel-lean and fuel-rich gas mixtures (i.e., equivalence ratio (ϕ) is at 0.6-0.8 and 1.2, respectively) while perfectly flat laminar flame is stabilized at the stoichiometric gas mixtures ($\phi=1$) as well as at increasing temperature of burner plates. At a fixed feeding ratio of the pilot gas mixtures, the particle characteristics are mostly governed by the ratio between precursor solution flow rate (PFR) and dispersion gas, which influence the spray break up and therefore the droplet size, the lifetime droplets and intraparticle collisions. Previous reports emphasize that increasing PFR at the fixed O_2 feeding rates was related to the formation of larger flames, which prolongs the lifetime of the droplet and particle and therefore increasing particle collision, coalescence and sintering.^{74,75} On the other hand, higher flow rates of the dispersion O_2 gas at the fixed PFR dilute the droplet and particle concentration and thus reduce their lifetime in the flame, allowing generation of high-surface area and smaller nanoparticles.^{76,77} Excessive flow rates of the O_2 is detrimental and associated with a quenching effect on the particle formation, which can lower particle crystallinity.⁷¹ Alongside the PFR to dispersion gas ratio, linear velocity of dispersion O_2 has a significant influence on the particle size distribution. More precisely, an increase in the O_2 gas velocity is considered to trigger the change in the flow regime from laminar to turbulent. In the turbulent regime, formation of high surface area particles with more homogenous particle-size distributions was observed. The reason is that the turbulent flow regime more likely allows the residence time of particles/droplet to be uniform in the flame, and therefore leads to uniform mixing of primary particles. Overall, together with PFR to dispersion O_2 gas ratio, the linear velocity of dispersion gas deserve critical attention in the spray-flame synthesis of complex nanoparticles like perovskites.⁷¹

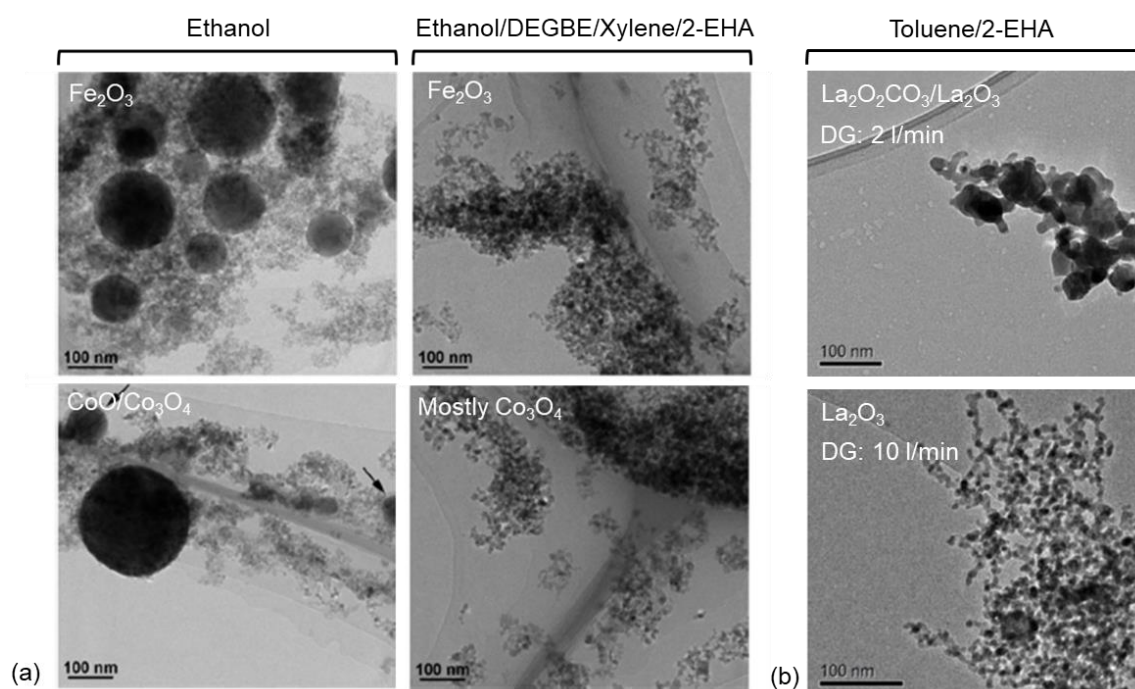


Figure 13 a) Influence of the solvent mixture on the particle morphology and phase/chemical composition of spray-flame-synthesized Fe_2O_3 and CoO/Co_3O_4 compounds from metal nitrates.⁶⁵ b) Effect of increasing dispersion O_2 gas on the particle distribution, phase and chemical composition of $La_2O_2CO_3/La_2O_3$ nanoparticles produced from La 2-ethylhexanoate precursors.⁷⁸

In addition to process parameters, precursor characteristics were well researched for spray-flame-synthesized Fe, Co oxides, La oxide/oxy carbonate and $LaCoO_3$ in previous reports.^{65,72,78} For the synthesis of Fe and Co oxides, precursor solutions containing metal nitrates and alcohol usually show bimodal

particle size distribution consisting of large particles (i.e., CoO and Fe₂O₃) through droplet-to-particle conversion and small nanoparticles (i.e., Co₃O₄ and Fe₂O₃) through gas-to-particle conversion. Addition of the organic solvent having high enthalpy content (e.g., xylene) and the carboxylic acids containing long hydrocarbon chains (e.g., 2-ethylhexanoic acid) allows the production of homogeneously distributed nanoparticles from gas-to-particle as indicated in Figure 13.⁶⁵ The underlying reason towards gas-to-particle formation is attributed to the formation of metal-carboxylate and/or metal-ester complexes in the precursor solution due to reaction of nitrate precursor with carboxylic acid, which facilitates the evaporation of metal precursors and gas-to-particle particle formation.⁷⁹ Together with that, when boiling point of the organic acid is higher than superheating temperature of alcohol, cascade-like microexplosion reactions can take place during the decomposition of metal carboxylates/esters complexes, and these reactions allow gas-to-particle conversion processes and production of homogenous nanoparticles.⁸⁰ For spray-made synthesis of La compounds, the precursor solution consisting of La 2-ethylhexanoate and toluene/2-EHA solvent mixture allows the synthesis of La₂O₃/La₂O₂CO₃ compounds, and the role of increasing dispersion O₂ gas flow is emphasized for the generation of homogenous, nanosized La₂O₃ compounds rather than La₂O₂CO₃.⁷⁸

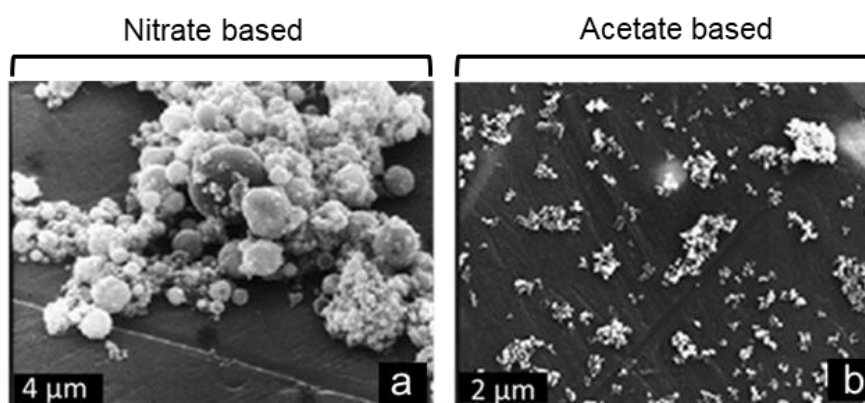


Figure 14 a) Particle morphology of the as-prepared nanoparticles including both nanosized LaCoO₃ particles and micron sized combustion residuals (large and black particles), when precursor salts are selected as nitrate salts and 1-propanol/propionic acid mixture is used as solvents. b) Highly homogenous distribution of as-prepared LaCoO₃ nanoparticles when acetate salts are used as precursors and dissolved in the same solvent mixture.⁸¹

In the case of LaCoO₃ nanoparticle synthesis from the metal acetate precursor salts, the importance of the solvent was underlined to affect the phase-purity of the as-synthesized nanoparticles. A set of carboxylic acids with varying carbon chain length were used to dissolve the metal acetate precursors to synthesize the LaCoO₃ perovskite. It was found that the carboxylic acids having longer carbon chains lead to an increase in flame temperature and thus trigger the formation of more phase-pure perovskites. Mixing the carboxylic acids with alcohols containing longer hydrocarbon chains generated phase-pure and smaller-sized LaCoO₃ nanoparticles.⁷² The chemical composition of precursor salts was also studied using acetate and nitrate precursors with the same solvent mixtures. With acetates better phase purity, more homogenous particle-size distribution and higher specific surface area was obtained and thus they are suggested to be suitable precursors for the spray-flame synthesis of LaCoO₃ perovskite nanoparticles.⁸¹

3 Analytical Methods

3.1 ATR-FTIR spectroscopy

Infrared radiation is electromagnetic radiation having a range of frequencies between 10,000–100 cm^{-1} , which organic and inorganic molecules can absorb. By quantizing the absorption energies, the vibration of a molecule can be obtained as discrete lines being used in identification of different molecular species.⁸² Among infrared spectroscopy techniques, ATR-FTIR spectroscopy (Attenuated Total Reflection Fourier Transform Infrared spectroscopy) is widely used for the analyses of all kinds of solid samples, including powders, pastes, pellets, slurries, and thin films. The most important advantage of this method compared to other FTIR measurement techniques are an easy and fast sample preparation.⁸³

A typical ATR-FTIR device comprises an ATR crystal such as diamond or germanium that is transparent to the infrared radiation. Pressure clamps are used to provide a uniform contact between the samples to be measured (e.g., nanoparticle powder) and the ATR crystal. The incoming IR beam is usually entering the ATR crystal at an angle of 45° (Figure 17a, incident IR beam enters from the left). A certain fraction of the IR beam reaches the sample in the evanescent field, where a part of the IR light is absorbed by the sample at specific IR energies. Due to the geometry and the incident angle, multiple internal reflections occur before the attenuated IR beam reaches the detector. The measured signal is Fourier transformed as in a common FTIR spectrometry leading to a spectrum showing the material-specific absorption spectra. The spectra obtained are interpreted to determine the chemical composition of the materials investigated based on literature reference data.

For ATR-FTIR measurements in this study, a Bruker Vertex 80 spectrometer equipped with a diamond crystal was used. The spectra were measured from 4000–400 cm^{-1} with a resolution of 4 cm^{-1} , and the obtained spectra correspond to average spectra of 16 consecutive scans in one measurement.

In the context of this thesis, electrochemical *operando* measurements combined with-ATR-FTIR spectroscopy were also applied in cooperation with the Muhler group at the Ruhruniversität Bochum to follow the electrochemical reactions occurring during ethanol oxidation experiments. Figure 17 displays the recently constructed holder setup, details of which can be found in a previous report.^{84,85} Briefly, the electrode holder containing a working, counter, and reference electrode (Figure 17) is mounted in an ATR-FTIR instrument as shown in Figure 16. Using the micrometer screw on top, the thickness of a thin electrolyte layer between the ATR-FTIR crystal at the bottom (e.g., germanium) and the surface of working electrode positioned above the ATR crystal can be adjusted. This setup, developed by the Muhler group was used to combine ATR-FTIR spectroscopy with cyclic voltammetry experiments (CV).

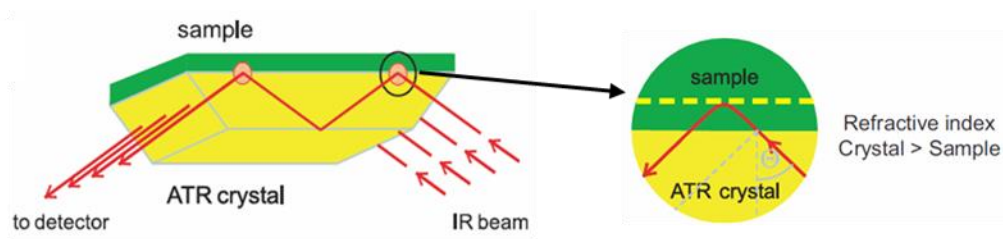


Figure 15: The principle of the ATR device: penetration of the incoming IR beam into ATR crystal and sample, followed by reflection of a fraction of the IR beam after being absorbed by the sample. After several internal reflections, the attenuated beam reaches the IR-detector. The refractive index of crystal needs to be higher than that of the samples to allow reflection of the IR beam at the crystal surface.⁸³

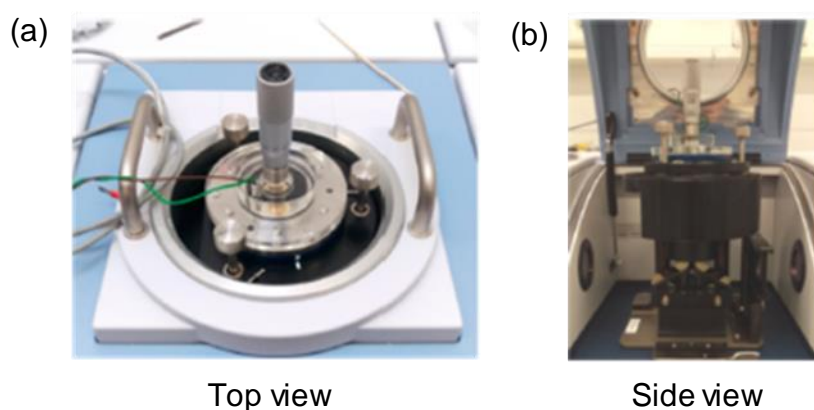


Figure 16: a) Bruker Tensor 27 ATR-FTIR spectrometer optimized for electrochemical cells developed by the Muhler Group et al.⁸⁵ b) Top view of the A530/P reflection unit in the sample compartment. Side view of the closed sample compartment with inserted electrode holder shown in Figure 17.

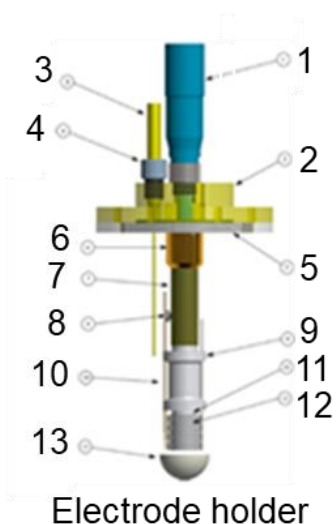


Figure 17: Configuration of the electrode holder for spectroelectrochemical experiments comprising: micrometer screw (1), acrylate glass lid (2), reference electrode (3), reference electrode holder (4), metal lid (5), micrometer adapter (6), extension (7), external connection of working electrode to potentiostat (8), counter electrode/microelectrode holder (9), Pt microelectrode (10), rotating disk electrode (11), counter electrode (12), Ge internal reflection element (13).⁸⁵

In collaboration with Steffen Cychy in the Muhler Group, *operando* ATR-FTIR measurements were carried out. The pristine and 60 at.% Fe substituted LaCoO₃ catalyst inks (same composition as presented before) were drop-casted on a polished 0.5 cm² glassy carbon electrode to obtain a surface loading of 200 μg/cm², in accordance to the rotating disk electrode measurements (RDE). Likewise, the electrodes were similarly conditioned and pretreated with respect to the applied potentials as well as the Ar-out-gassed 0.1 M KOH, but in a single-compartment setup. After pretreatment, the electrode holder was transferred to the spectroelectrochemical setup and a distance of 20 μm between the working electrode surface (WE) and the Ge internal reflection element was adjusted. The electrode holder and the used setup are described in detail previously.⁸⁵ Spectroelectrochemical measurements were conducted by applying a constant potential for 20 min in Ar-saturated 1 M EtOH/0.1 M KOH electrolyte under constant feeding of Ar using a Metrohm Autolab potentiostat. Potentials are then increased between 1.38 V vs. RHE and 1.78 V vs. RHE in 100 mV steps, with axial and lateral movement of the holder to refresh the electrolyte in the thin film between the measurements. Operando ATR-FTIR spectra were recorded using a Bruker Tensor 27. The FTIR spectra were averaged over 200 scans (90 s).

3.2 X-ray diffraction

X-ray radiation is a type of electromagnetic radiation that is frequently used to determine the crystal structures of materials. Because of its short wavelength (~0.01 to 100 nm), it provides information about the atomic bond lengths in crystal structures. One of the most widely used X-ray techniques to research these properties is the powder X-ray diffraction technique. Here, monochromatic X-ray radiation interacts with powder materials. When the scattered X-rays get in constructive interference, the Bragg reflections occur (Figure 18). A detector is used to detect the intensity of the diffracted beam as a function of the diffraction angles.

Since the diffraction patterns depend on the crystal structure, they give information about the chemical and structural properties of the materials, such as composition, atomic composition and crystal size of crystalline phases. Bragg's law is used to explain the relationship between the wavelength of the X-ray beam and interplanar distances in crystalline structures:

$$n \lambda = 2 d \sin\theta ,$$

where n is the order of the reflection, λ is the X-ray wavelength, d is the distance between the lattice planes and θ is the angle between the incoming X-rays and the lattice plane. As the interatomic distances are materials-specific, this technique allows the identification of the fingerprint pattern of numerous crystalline phases and discovery of new crystalline phases.

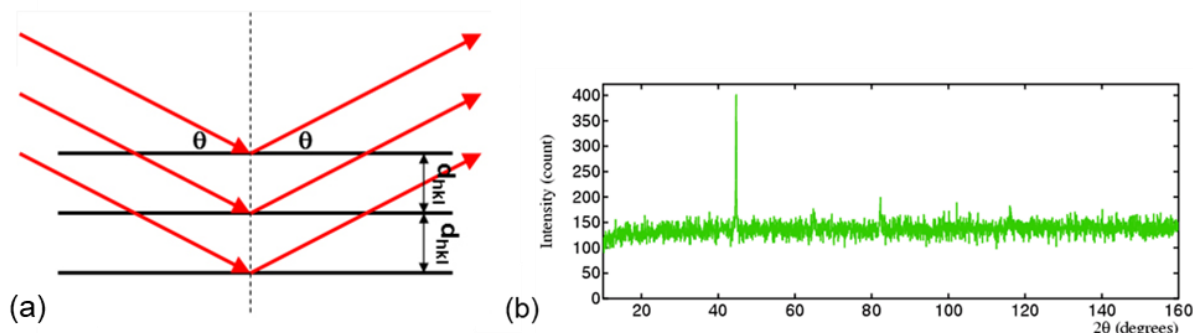


Figure 18: a) Reflection of the in-phase incoming X-ray radiation from the atoms in particular set of lattice plane resulting in the constructive interfered, harmonized diffraction beams.⁸⁶ b) X-ray diffraction pattern indicating the contribution of strong background signal in addition to the diffraction peaks.⁸⁷

In the analysis of characteristic diffraction peaks, strong background due to incoherently scattered X-rays can be a problem in the analysis (Figure 18b). Transition metals, such as Co and Fe, cause additional strong background due to fluorescence when the X-ray source is Cu K_{α} . Other X-ray sources (Co K_{α} and Fe K_{α}) or monochromators before the detector suppress the fluorescence effect and thereby enable interpretation of the X-ray diffraction patterns also for these materials.

For this thesis, XRD devices having both Co and Cu anodes were used. Initially, in collaboration with Benjamin Breitbach, Max-Planck-Institute for Iron Research, A SEIFERT analytical XRD (Diffractometer X6_WS) was used. A Co anode (Co K_{α} : 1.7902 Å) was used, operated at 40 kV and 40 mA step using an energy dispersive point detector (Meteor0D). XRD data were collected between $2\theta = 20\text{--}60^{\circ}$ with a step size of 0.1° and a count time of 20 s/step was used for the measurements.

In addition, with contribution of the Winterer group at the University of Duisburg-Essen, a PANalytical X'Pert PRO X-ray diffractometer was used. A Ni-filtered Cu anode (Cu K_{α} : 1.5406 Å) was used for the measurements. It was operated at 40 kV and 40 mA using a linear position sensitive X'Celerator detector and a monochromator. A Si low-background sample holder was used. XRD data were collected between $2\theta = 10\text{--}80^{\circ}$ with a step size of 0.03° and a count time of 3.6 s/step.

The XRD patterns obtained with the Cu source were used for profile refinement analysis utilizing the GSAS software. For these analyses, the XRD pattern of the LaB6-660a standard sample was initially refined and its instrumental parameters were used. For background fitting of the raw XRD patterns of Fe-substituted samples, the shifted Chebyshev polynomial function was used. For profile refinement, the sample displacement and lattice parameter parameters are separately refined to fit the peak position of the reference diffraction pattern to those of the raw XRD patterns. Following to that, the Thompson-Cox-Hastings version of the pseudo-Voigt function was used to define the peak broadening in the raw XRD patterns. Using the refined Lorentzian broadenings in the pseudo-Voigt function and assuming that the particles are spherical, the crystallite sizes of each phase were calculated. Micro-strain parameters were not fitted in any of the refinements, due to their high correlation with those of crystallite size parameters. After completing the refinement analyses, the weight fractions of individual phase were obtained and converted into volume fraction of the phases.

3.3 X-ray photoelectron spectroscopy

X-ray photoelectron spectroscopy is a surface characterization technique to research surface composition and oxidation state of elements, which are in the range of 0.1–1 nm.⁸⁸ Its working principle relies on the photoelectric effect where X-ray irradiation leads to the emission of electrons. When the applied radiation has sufficient energy to eject an electron from the inner core of near surface atoms, the ionization of elements occurs. Because the ionization energies of elements are materials-specific, they allow identification of the chemical composition of the compounds.

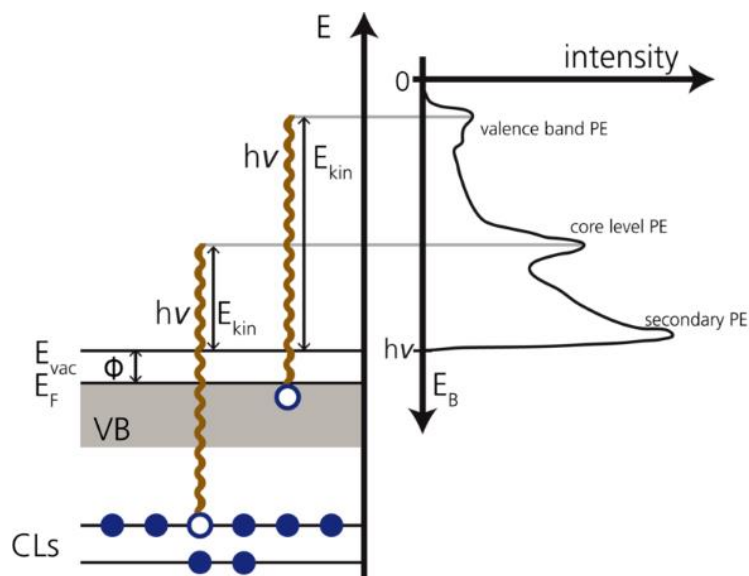


Figure 19: The ejection of the core-level and valence electrons by the incident photon and reflection of the kinetic energy of the photoelectrons in the XPS spectra⁸⁹. CLs: Core-level shifts, VB: Valence band, E_F : Fermi energy, E_{vac} : Vacuum energy, ϕ : Electrostatic potential in the vacuum near the surface, E_{kin} : Kinetic energy, PE: Photoelectron, E_B : Binding energy, h : Planck constant and ν : Frequency of the light.

With the use of X-ray or ultraviolet sources having energies of about 5–40 eV, core-level electrons release. Due to the ultra-high vacuum environment ensured in the XPS chamber, the released electrons do not collide considerably with gas molecules. Before the photoelectrons reach the detector, an energy-filter device is used to separate their kinetic energies. Then, with the conversion of the kinetic energy of the detected photoelectrons (E_{kin}) into the corresponding binding energies, using the equation below, the chemical species are examined.

$$E_{kin} = h\nu - E_b - \phi$$

where $h\nu$ corresponds to the photon energy of X-ray source, ϕ is the work function of the spectrometer and E_b is the initial binding energy of the released electron. Because of the chemical surrounding of core-level electrons influence their binding energy, any change in the energy levels of the core-level electrons modifies their binding energy and therefore the position of the XPS signals in the spectra. These modifications in the binding energies are used to determine the chemical state of the surface elements in the samples. Also, the intensities of the XPS signals are used to calculate the surface composition of the elements, which is rather critical for catalyst materials.

In this thesis, in collaboration with Ulrich Hagemann from the interdisciplinary center for analytics on the nanoscale (ICAN) in the University of Duisburg-Essen, a VersaProbe II (Ulvac-Phi, Chanhassen, USA) XPS instrument equipped with both Al K_{α} ($h\nu = 1486.6$ eV) and Mg K_{α} ($h\nu = 1253.6$ eV) anodes were used to record XPS spectra. A pass energy of 11.75 eV was used for the regional XPS. All binding energies were calibrated to the C1s signal at 284.8 eV.

For XPS measurement carried out with Al anode, before interpreting the Fe2p XPS, the subtraction of the Co Auger peak was necessary. Thus, the integrated area of the Co Auger peaks was initially derived for pure LaCoO₃ (LCO), and this area was then decreased at increasing Fe concentrations based on the relative content of the Co ions. Finally, the integrated areas of the Co Auger peaks were subtracted from the Fe 2p spectra to obtain the spectra originating only from Fe. For XPS measurement performed with Mg anode, XPS spectra of Fe2p were analyzed without any data correction.

3.4 Transmission electron microscopy

Transmission electron microscopy (TEM) is a well-established microscopy technique for uncovering the structural and chemical properties of catalysts. It consists of three main parts, namely, the illumination system, the objective lens/stage, and the imaging system.⁹⁰ The illumination system contains the electron source and condenser lens that are used to focus the electrons for the illumination conditions such as spot size and convergence angle. Parallel or convergent beam conditions can be also adjusted by tuning of strength of condenser lenses. Under the illumination component, the objective lens is present and contains the sample holder, which can be tilted along one or two axes so as to align the specimen with respect to the electron beam. The objective lens is a critical component to adjust the image quality of the samples. The other lenses below the objective lens namely intermediate and projector lenses are used to tune the magnification and to project an image or a diffraction pattern on the detector. The simplified scheme of the ray paths of an electron beam is given in Figure 20a.

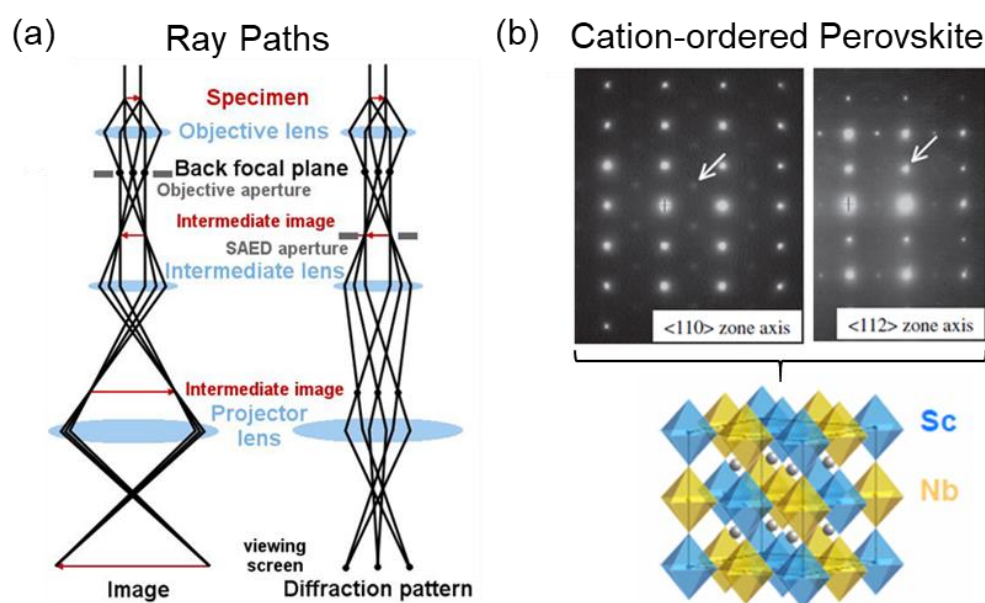


Figure 20: a) The schematic image showing the main units of transmission electron microscope (TEM), namely objective, intermediate and projector lenses together and illustrating how intermediate, final images and diffraction patterns are created.⁹⁰ b) The open arrows in the electron diffraction

patterns indicates the superstructure reflections, which imply of cation ordering in the crystal structure of perovskites, such as $\text{Pb}(\text{Sc}_{0.5}\text{Nb}_{0.5})\text{O}_3$.⁹¹

The TEM instrument is used here to visualize nanoparticles. At low magnification, the TEM images are useful to analyze the size distribution of nanoparticles. At high magnifications, imaging techniques such as high-resolution TEM (HR-TEM) enable the visualization and identification of nanoparticle shape and structure. In addition, high-angle annular dark-field scanning transmission electron microscopy (HAADF-STEM) is used to resolve the nanostructure down to the sub-nm scale. Thus, it enables the identification of atomic structures. Also, it allows chemical mapping of the nanoparticles and therefore provides information about their composition at high-resolution images.

Together with visualization and chemical composition data, the electron diffraction patterns are also used to find out the structural details of crystals, such as determination of crystal orientation, symmetry operation, and inter-planar spacing. For example, the electron diffraction patterns measured at different zone axis are useful for understanding complex structural phenomena such as cation ordering occurring in double perovskites (Figure 20b) or researching new crystalline compounds.

In this thesis, in collaboration with Markus Heidelmann from the interdisciplinary center for analytics on the nanoscale (ICAN) of the University of Duisburg-Essen, HRTEM, HAADF STEM, energy-dispersive X-ray spectroscopy (EDX), and selected area diffraction (SAED) measurements were performed with a JEM-2200FS (JEOL). For sample preparation, the nanoparticles were dispersed in ethanol and the mixture was sonicated for 10 min. Then, the dilute dispersion was dropped on a carbon-coated copper grid and dried. To make a comparison with the volume based XRD crystallite size, the number mean particle sizes obtained from TEM measurements were converted into the volume based mean size under the assumption that particle have spherical size.

3.5 Mößbauer spectroscopy

Mößbauer spectroscopy is a technique to obtain information about the local environment of atoms and to reveal the chemical, structural and magnetic properties of numerous compounds.⁹² It relies on the so-called Mößbauer effect which corresponds to recoil-free gamma-ray emission and absorption. The use of the Mößbauer isotope such as ^{57}Fe , which has low gamma-ray energy and long-lasting excited state, allows recoilless events to occur in a radioactive source. Then, gamma-ray energy of the radioactive source is modulated based on the Doppler Effect to detect the hyperfine interactions between atomic nuclei and their surrounding in the absorber. When nuclear transition energies in the absorber match with those in the gamma-ray emitter, the absorption phenomena occur. The absorbed energy displays as a peak in the Mößbauer spectra (Figure 21a).

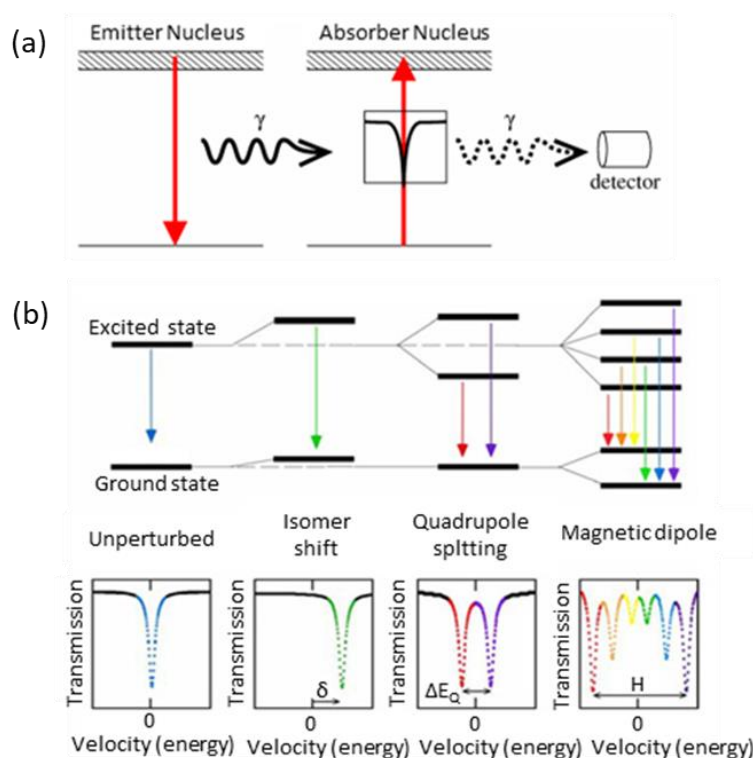


Figure 21: a) Scheme of Mößbauer spectrum from the identical source and absorber.⁹² b) Hyperfine parameters.⁹³

The main Mößbauer parameters; namely, isomer shift, quadrupole splitting, and magnetic splitting are used to examine the modification in the energy levels of the absorber nuclei (Figure 21b).⁹⁴ The isomer shift occurs due to a Coulombic interaction between nuclei and electrons. They are used to determine the valence states such as oxidation state of Fe, as well as to examine the ligand bonding states, electron shielding and electron-drawing power of electronegative groups. When a nuclear quadrupole moment interacts with an inhomogeneous electric field, electric quadrupole interactions occur, which is the origin of quadrupole splitting. It is a useful parameter for examining the degree of crystallographic site distortion, the oxidation state, spin state, and atomic coordination. When magnetic dipole interaction occurs between nuclear magnetic dipole moment and magnetic field, magnetic splitting takes place. It provides information about the magnetic interactions in the absorber such as ferromagnetism, paramagnetism or antiferromagnetism. Overall, using these Mößbauer parameters together allows detailed information about the electronic structure of the Fe-based compounds.

In collaboration with the Wende group, namely Joachim Landers and Soma Salamon at the University of Duisburg-Essen, a constant-acceleration Mößbauer driving unit was used for recording Mößbauer spectra in transmission geometry. α -Fe foil was used at room temperature as a reference sample to calibrate the spectrometer and a superconducting magnet in split-coil geometry was utilized for recording low temperature Mößbauer spectra at 4.3K. Temperature-field-dependent magnetization curves were recorded in a Quantum Design PPMS DynaCool. Field-dependent magnetization data were recorded at 4.3 K in external magnetic fields up to 9 T. Temperature-dependent measurements were performed by cooling down the samples without external field and recording the sample magnetization at 10 mT upon heating from 5–400 K and cooldown from 300–5 K to check for phase transitions and/or superparamagnetic properties.

3.6 Brunauer-Emmett-Teller analysis

Brunauer-Emmett-Teller (BET) analysis is used to determine the specific surface area of the materials such as porous solids and nanoparticles.^{95,96} At the fixed operating temperatures, the physisorption of an inert gas (usually N₂ or Ar) on the external and internal surface of solids is used to obtain the BET adsorption isotherms. These isotherms are useful to estimate the amount of an adsorbed monolayer of gas on the material surface (n_{mono}). The multiplication of the adsorbed gas amount by the area occupied by one adsorbed gas molecule (a_g) allows calculating the BET surface area (A_{BET}). The equation used to calculate the BET surface area is;

$$A_{BET} = n_{mono}a_g$$

Before BET measurements, a degassing operation is usually applied to clean the surface of the samples from other adsorbed impurities such as adsorbed water. Following to the degassing, the BET measurements were performed to determine the BET surface area. Its value is also used to estimate the average particle diameter (d). Assuming particles have a spherical shape, particle bulk density values (ρ) and the BET surface area are used to calculate the particle diameter by the following equation;

$$d = 6 / (A_{BET}\rho)$$

3.7 Linear sweep and cyclic voltammetry, rotating disk electrode measurements

Linear-sweep voltammetry (LSV) and cyclic voltammetry (CV) are typically used to determine the electrocatalytic activities of a catalyst. A test tube which contains a working, a reference and a counter electrode in an electrolyte is used to conduct these measurements (Figure 22a).⁹⁷ A potentiostat is connected to the electrochemical cell and used to maintain the potential difference between working and reference electrodes.

In voltammetry measurements, a function generator first relays the linear voltage sweep to a potentiostat. For LSV measurements, the voltage scan is in a constant range from low limit to high limit values. For the CV measurements, the voltage scan is in both directions from low to high and high to low limit values (Fig.16 a). Due to the potential sweep applied, current flows through the electrochemical cell (being a response from the potentiostat to maintain the potential difference between working and reference electrode). A current-voltage converter then measures the cell current. The current is usually divided by the electrode surface area to calculate the current density. In this way, the x - y recorder displays the current density-potential curves, namely polarization curves. Figure 18 shows a typical CV scan for a reversible reaction indicating for an anodic current (A.C.) under oxidation and a cathodic current (C.C.) under reduction.

To examine the kinetics and mechanism of electrochemical reactions of the electrode surface, a rotating-disk electrode system (RDE as a working electrode) is typically used. The disk electrode is usually composed of glassy carbon embedded in an insulator rod such as a teflon sheath. Because the disk electrode is in connection with a motor, it rotates at a high angular velocity. This system allows isolating the

electrochemical surface reactions from the transport of the reactants and products of reactions. Thus, it enables to research the kinetics of fast reactions and transfer rates of electrons to the electrode surfaces.

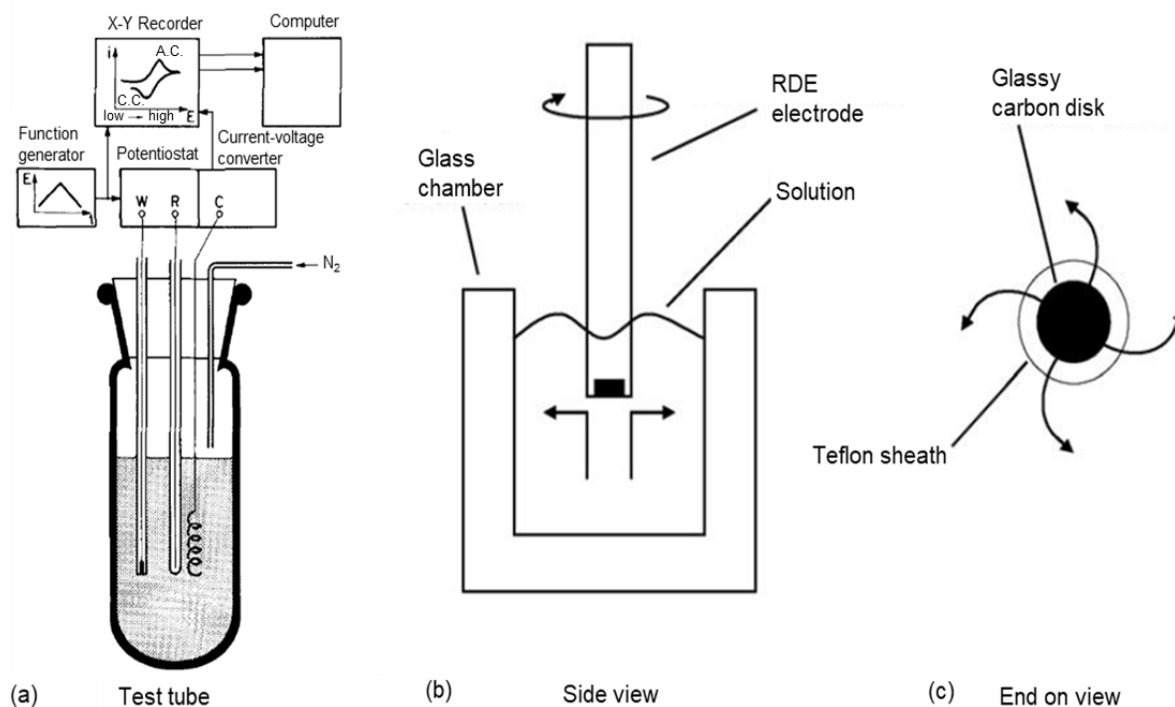


Figure 22: a) Schematics of an electrochemical cell including its main components.⁹⁷ b) Representation of the rotating disk electrode in a solution-filled glass chamber and c) the materials of the working electrode disk and insulator material.⁹⁸

In collaboration with the Schuhmann group, namely Wolfgang Schuhmann, Corina Andronescu and Danae Ramirez, Ruhruniversität Bochum, electrocatalytic measurements for OER and ethanol oxidation were performed. Initially, catalyst inks were prepared by dispersing 5 mg of perovskite nanoparticles in 1 mL of solvent mixture (0.49 ml water, 0.49 ml ethanol and 0.02 ml Nafion solution). Following 30 min of sonication, a defined volume of the homogeneous ink was drop-coated on a glassy carbon rotating disk electrode (RDE) leading to a catalyst mass loading of 200 $\mu\text{g}/\text{cm}^2$.

RDE measurements were carried out in a three-electrode cell using a Pt mesh as the counter electrode and a Ag/AgCl/3 M KCl as reference electrode. As working electrode, the catalyst-coated RDE was used and an Autolab potentiostat/galvanostat equipped with RDE rotator was employed to rotate the working electrode. A glass frit was used to separate the counter electrode from the bulk electrolyte solution. Electrochemical experiments were performed both in 0.1 M and 1 M KOH solution, which was previously outgassed with Ar. Before the evaluation of OER activity, the catalyst surface was conditioned by being cycled in the potential range between 0.2 to 0.5 V vs. Ag/AgCl/3 M KCl with a scan rate of 100 mV/s until reproducible CVs were registered. To determine the uncompensated solution resistance (R), electrochemical impedance spectroscopy (EIS) was applied in the range from 10 kHz–100 Hz using 10 mV AC amplitude at open circuit potential (OCP). The OER activity was evaluated by recording cyclic voltammograms in the potential range between 0.2–0.8 V vs. Ag/AgCl/3 M KCl at a

scan rate of 5 mV/s and 1600 rpm. For the evaluation of the ethanol oxidation activity, the same procedure was used as for the OER in the presence of 1 M ethanol dissolved in the 0.1 M KOH solution.

The potentials (in V) registered vs Ag/AgCl/3 M KCl as reference electrode were converted to the RHE scale and corrected for the uncompensated resistance using the following formula:

$$E_{RHE} = E_{Ag/AgCl} + E_{Ag/AgCl\ 3M\ KCl}^0 + 0.059\ pH - i\ R$$

Where E_{RHE} is the potential expressed in V vs. RHE, $E_{Ag/AgCl}$ is the potential measured in V vs. Ag/AgCl 3 M KCl, $E_{Ag/AgCl/3M\ KCl}^0$ is the formal potential of Ag/AgCl/3 M KCl (in V), i is the registered current (in A) and R is the solution resistance (in Ω) which was evaluated from the EIS recorded at high frequencies.

The ECSA was determined following the protocol described in literature.⁹⁹ Cyclic voltammograms were recorded in the OCP \pm 0.05 V potential window using different scan rates (ν): 0.005, 0.01, 0.025, 0.05, 0.1, 0.2, and 0.4 V/s. 10 s of waiting time was used between the anodic and cathodic scans. The electrochemical double-layer capacitance (C_{DL}) was calculated using the following formula:

$$C_{DL} = \frac{i}{\nu}$$

where i represents the current registered at different scan rates for a given potential value in the non-Faradaic region, evaluated from the anodic or the cathodic scan of the CV. The corresponding C_{DL} values resulted from the anodic and cathodic currents (in modulus) were averaged and were further used to calculate the ECSA, using the formula:

$$ECSA = \frac{C_{DL}}{C_s}$$

where C_s represents the specific capacitance, which is approximated to be 0.04 mF/cm² in alkaline electrolyte.

4 Experimental Procedure

4.1 Spray-flame synthesis of the $\text{LaCo}_{1-x}\text{Fe}_x\text{O}_{3\pm\delta}$ perovskites

Spray-flame synthesis of perovskite nanoparticles containing La, Co, and Fe was performed to yield nanoparticles with a defined La/Co/Fe ratio. The precursor solution was prepared with a constant molar ratio between La and (Co+Fe) precursors and a varying Co/Fe precursor ratio. For the preparation of the precursor solution, 1-propanol (50 ml), propionic acid (50 ml), and DI water (10 ml) were initially mixed in a glass flask in ambient atmosphere. Afterwards, the La-, Co-, and Fe-containing precursors were added to the freshly prepared solvent mixture keeping a total metal loading of La+Fe+Co as 0.1 M. Different atomic ratios of Fe/(Fe+Co) (x_{Fe}) were used to adjust a total amount of Fe (at.%) of 0, 20, 40, and 60 in the solution. Also, the La/(Co+Fe) atomic ratio was selected as 1 for all samples. Then, the solution was maintained to stir overnight. As-prepared La- and Co-based nanoparticles are labeled LCO. Fe-containing La- and Co-based nanoparticles are labeled with “x at.% Fe” to represent the Fe/(Fe+Co) precursor ratio.

A homemade enclosed spray-flame synthesis reactor was used to synthesize perovskite nanoparticles.¹⁰⁰ Figure 23a demonstrates the scheme of the reactor. A premixed pilot flame was provided using 1 slm of CH_4 and 2 slm of O_2 . 3 ml/min of the precursor and 4 slm of the dispersion O_2 gas was provided through a two-flow nozzle for spray formation. The reactor pressure was kept at 950 mbar. 125 slm of sheath gas (compressed air) and 170 slm of quench gas (compressed air) were provided to the reactor. The product nanoparticles were collected on a circular filter membrane. After the synthesis, the particles rested on the filter membrane for 30 min inside the filter house at 900 mbar so that they can fully dry. Subsequently, they were harvested from the filter membrane. Table 1 summarizes the process and solvent parameters for these syntheses.

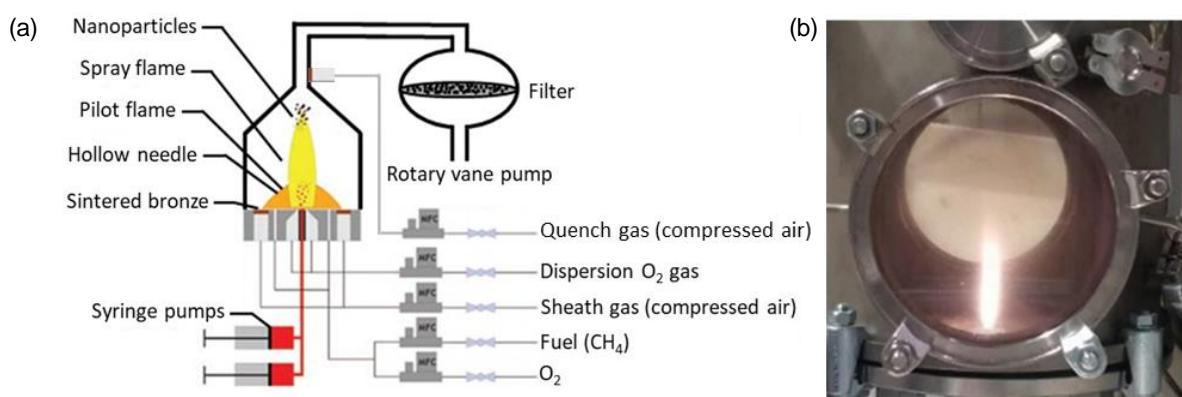


Figure 23: Scheme of the spray-flame reactor ((a), adapted from Ref.¹⁰⁰) and photo of the spray flame during the synthesis of Fe-substituted LaCoO_3 (b).

Table 1: Spray-flame process parameters and the solutions used.

Process and solution parameters	x_{Fe} , $\text{LaCo}_{1-x}\text{Fe}_x\text{O}_3$			
	0	0.2	0.4	0.6
CH_4/O_2 pilot flame / (slm/slm)	1/2			
Dispersion gas O_2 / slm	4			
Solution flow rate / (ml/min)	3			
Pressure / mbar	950			
Sheath gas (compressed air) / slm	125			
Quench gas (compressed air) /slm	170			
Precursors	La, Co, Fe acetates			
Solvent Mixtures (vol.%)	Propionic acid : 1-propanol : DI water (5:5:1)			
La and (Fe+Co) concentration / M	0.1			

5 Results and Discussion

In this chapter, the main aim is to synthesize the $\text{LaCo}_{1-x}\text{Fe}_x\text{O}_3$ perovskite nanoparticles with the spray-flame method and analyze their materials and catalytic oxidation properties. For this aim, a complementary bulk and surface characterization measurements were carried out to examine phase composition, surface specific area, particle characteristics, the content of organic residuals from the synthesis and surface chemistry of the as-prepared nanoparticles. Following to that, the catalytic activity of the as-prepared nanoparticles for OER and ethanol oxidation were investigated in order to determine at which Fe contents the materials show more activity. Finally, spectroscopic measurements during ethanol oxidation reaction were performed to identify oxidation products in the most active and least active catalysts.

5.1 Materials characterization of as-prepared $\text{LaCo}_{1-x}\text{Fe}_x\text{O}_{3\pm\delta}$ nanoparticles

5.1.1 Qualitative phase analyses

The XRD measurements in Figure 24 indicate the influence of the Fe/Co precursor ratios on the crystalline phase of the as-prepared nanoparticles. The diffractograms show that independent of the Fe/Co ratio, four main crystalline phases are present; namely, $\text{LaCo}_{1-x}\text{Fe}_x\text{O}_3$ perovskite, $\text{La}_2\text{Co}_{2-x}\text{Fe}_x\text{O}_5$ brownmillerite, and $\text{La}_2\text{Co}_{1-x}\text{Fe}_x\text{O}_4$ and $\text{La}_4\text{Co}_{3-x}\text{Fe}_x\text{O}_{10}$ Ruddlesden-Popper type phases. Further qualitative analyses indicate that the A_2BO_4 -type Ruddlesden–Popper phases (detectable at $2\theta \approx 28^\circ$, 50° , and 54°) are only present at 0 and 20 at.% Fe. Diffractograms of LCO and 20 at.% Fe materials additionally show small reflections at $2\theta \approx 50^\circ$ and 32.3° , which are attributed to CoO and $\text{La}_2\text{O}_2\text{CO}_3$ respectively. Increasing the Fe content in the precursor solution (samples with 40 and 60 at.% Fe) induces a shift of the main reflections to smaller angles suggesting an expansion of perovskite lattice parameters due to Fe substitution. Such a shift was previously reported and supports the incorporation of Fe^{3+} into LaCoO_3 .^{101,102} Additionally, the main reflection for 60 at.% Fe-substituted LaCoO_3 perovskite phases (at $2\theta \approx 37.9^\circ$) is observed as a single peak, while for lower Fe substitution a broadening of this main peak is detected. This change is consistent with previous reports showing that for Fe contents higher than 50 at.%, the perovskites exhibit an orthorhombic crystalline structure, while they retain the rhombohedrally-distorted cubic structure at lower Fe content.¹⁰²

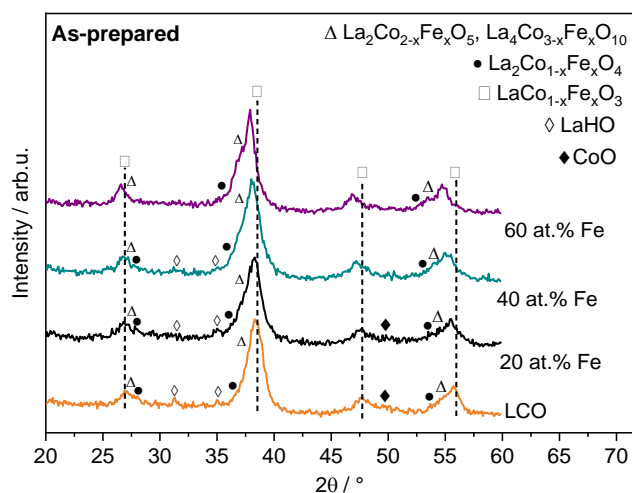


Figure 24: Co K_{α} -based X-ray diffractograms of the as-prepared nanoparticles at increasing Fe substitution. LaCoO_3 (LCO, ICSD no: 153986) and $\text{LaCo}_{1-x}\text{Fe}_x\text{O}_3$ ($x < 0.5$) belong to the same R-3c space group as LaCoO_3 . Other phases are; $\text{LaCo}_{1-x}\text{Fe}_x\text{O}_3$ ($x > 0.5$, ICSD no: 153877), $\text{La}_2\text{Co}_{1-x}\text{Fe}_x\text{O}_4$ (ICSD no: 151635), $\text{La}_2\text{Co}_{2-x}\text{Fe}_x\text{O}_5$ (ICSD no: 51198), $\text{La}_4\text{Co}_{3-x}\text{Fe}_x\text{O}_{10}$ (ICSD no: 51177), CoO (ICSD no: 9865), and $\text{La}_2\text{O}_2\text{CO}_3$ (ICSD no: 202988). The dotted lines indicate peak positions of LaCoO_3 (LCO).

Increasing the Fe/(Fe+Co) ratio also leads to changes in the peak shape of the $\text{A}_4\text{B}_3\text{O}_{10}$ -type Ruddlesden–Popper and Brownmillerite phases. Namely, at higher Fe content, a decreased intensity is observed for the diffraction at $2\theta \approx 28^\circ$, which indicates a lower content of the $\text{La}_2\text{Co}_{1-x}\text{Fe}_x\text{O}_4$ Ruddlesden–Popper phase. In parallel, sharper signals are registered at $2\theta \approx 37^\circ$ and 53° which can be attributed to $\text{La}_4\text{Co}_{3-x}\text{Fe}_x\text{O}_{10}$ Ruddlesden–Popper and $\text{La}_2\text{Co}_{2-x}\text{Fe}_x\text{O}_5$ Brownmillerite phases. Although overlapping diffraction peaks of the different phases do not allow to observe a clear trend regarding their phase content, the pronounced formation of Brownmillerite at increasing Fe substitution indicates that the secondary-phase composition is strongly influenced by the Fe/(Fe+Co) ratio.

5.1.2 Particle size and distribution, atomic structure and bulk composition

In addition to the qualitative phase analysis, the BET surface area and the average particle sizes of the as-prepared nanoparticles were obtained using the N_2 -physisorption measurements. Table 2 indicates that all as-prepared nanoparticles have high specific surface areas, which reach up to $116 \text{ m}^2/\text{g}$ and the corresponding average particle sizes down to about 7 nm. Despite LCO having a slightly higher particle size ($\sim 13 \text{ nm}$), those of Fe-substituted nanoparticles were calculated to have at or less than 10 nm.

Table 2: Specific surface areas of the synthesized perovskite oxides determined by N₂-physisorption measurements.

Sample	BET Surface area ^a / m ² /g	Calculated average particle size ^b / nm
LCO	64.3	12.9
20 at.% Fe	115.3	7.3
40 at.% Fe	116.2	7.4
60 at.% Fe	82.2	10.6

a: determined by N₂ physisorption, b: calculated from the specific surface areas according to the equation $d = 6/(A_{\text{BET}}\rho)$ with the assumption that particles have spherical shape.

Particle size and size distribution of the samples were also investigated using low-magnification TEM images. Figure 25 shows the size-distribution histograms fitted with log-normal functions. Agglomeration of the nanoparticles is visible in all the samples. Also, hexagonally-shaped and large crystals were detected in several nanoparticles. The particle size distribution was found to be similar for all the Fe-substituted LCOs, and shows average mean particle sizes of about 6–7 nm. It was also found that LCO nanoparticles, e.g., pristine LaCoO₃, show a larger particle size of about 14 nm. These results show a good agreement with the estimated particle sizes by BET measurements. In addition to the mean particle size, values of 1.2–1.4 for the geometric standard deviation (i.e., σ_g), which is used for normal distribution of lognormally fitted particle sizes, indicates the values of 1.2–1.4; therefore, suggest a self-preserved and monodisperse size distribution of the nanoparticles in all samples.¹⁰³

The insets in Figure 25 show the representative crystal structure of LCO and Fe-substituted LCO. All images confirm the single-crystalline structure of these nanoparticles. In the LCO sample, the representative crystal structure was found to be similar to the perovskite domains of Fe-substituted LaCoO₃ projected along <001> and <110> directions.¹⁷ Among Fe-substituted samples, similar crystalline structures were observed with no explicit structural changes regarding the Fe content.

The chemical composition of the samples (Table 3) was derived from the EDX-TEM data recorded for the area presented in Figure 26. The measured Fe/(Fe+Co) ratios agree well with the nominal ratios used in the precursor solutions. However, the overall La/(Co+Fe) atomic ratios tabulated in Table 3 indicate La-rich compositions (~10–20 at.%), irrespective of the used Fe concentration. EDX measurements performed on locally selected regions using dark-field STEM mode (Figure 26) reveal that on a small scale the regions with different La/(Co+Fe) ratios can be identified. In general, larger particles exhibit La-rich compositions while smaller particles mostly have similar chemical compositions to the overall EDX results except for very small nanoparticles having La-deficient composition.

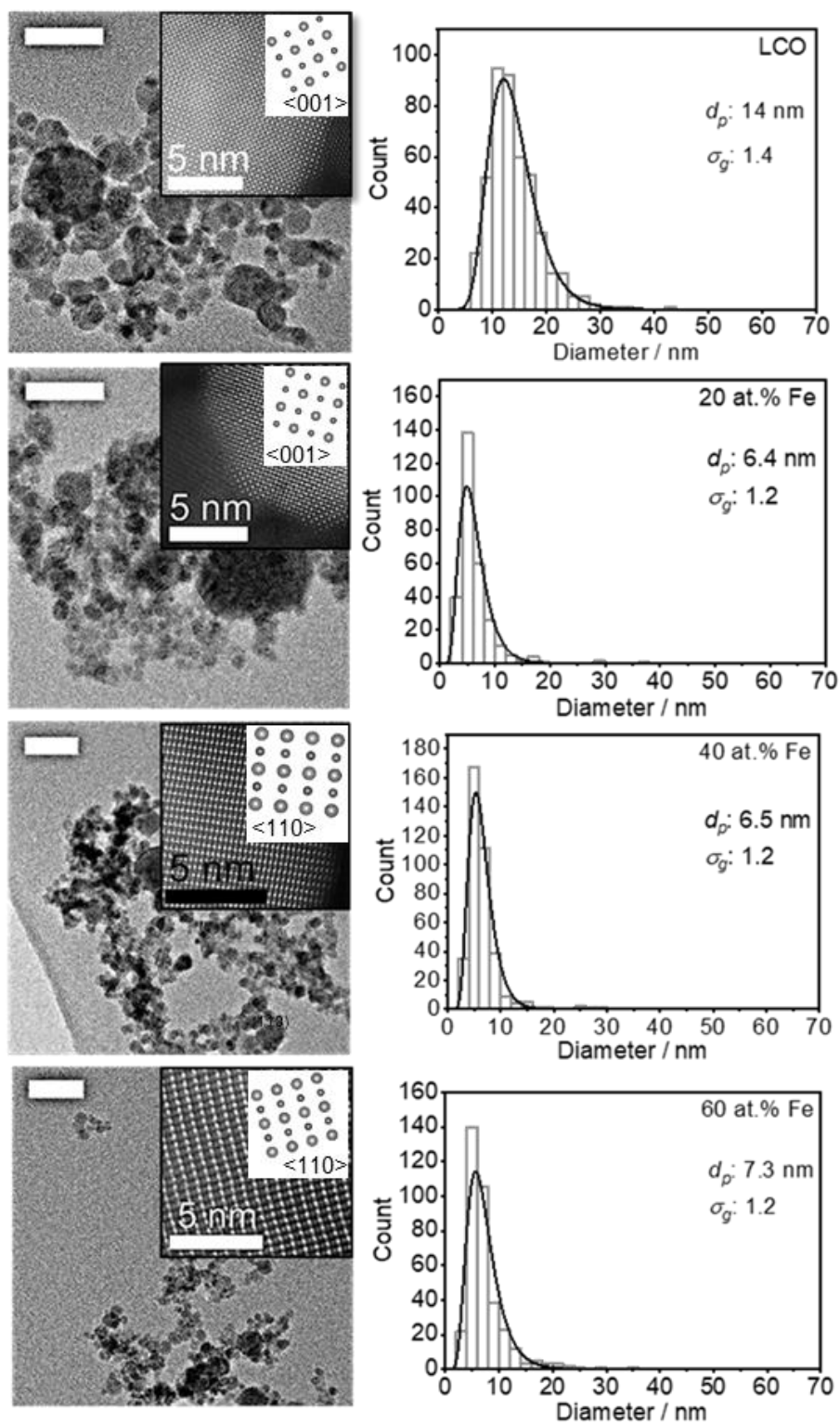


Figure 25: TEM, dark-field STEM images and particle size distribution of LCO and Fe-substituted LCO nanoparticles. Inset scheme in the STEM image show La atoms (big) and Co/Fe atoms (small) in model perovskite structure (ICSD no: 99369) viewed down along $\langle 001 \rangle$ and $\langle 110 \rangle$ family of directions. The model structures are drawn by VESTA software¹⁰⁴. The count mean particle size and geometric standard deviation were found by lognormal fitting of the histograms and abbreviated as d_p and σ_g , respectively. The scale bars are 30 nm.

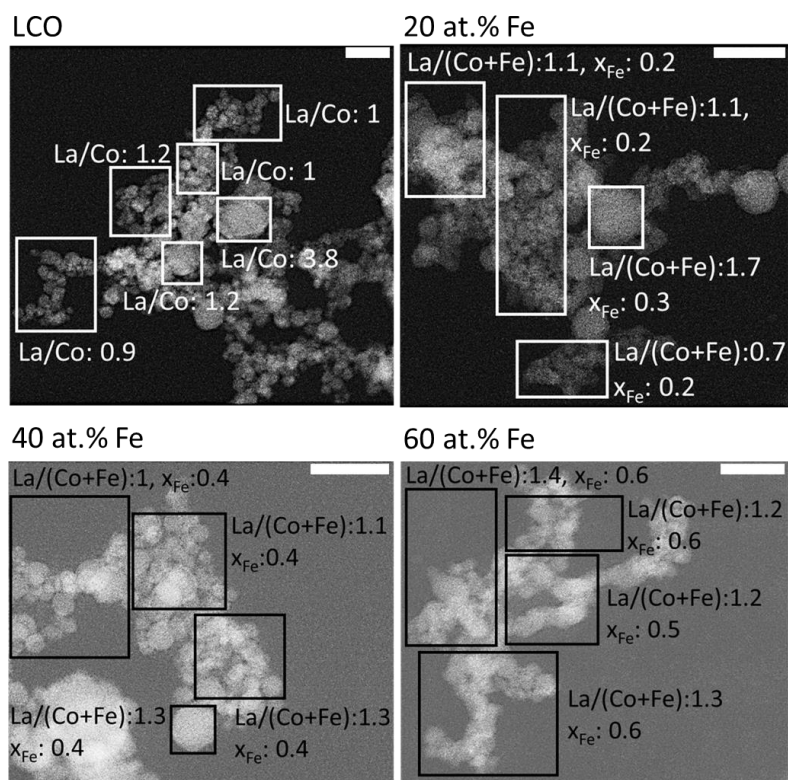


Figure 26: EDX measurements performed in dark-field STEM mode showing the $\text{La}/(\text{Co}+\text{Fe})$ ratio or $x_{\text{Fe}} = \text{Fe}/(\text{Co}+\text{Fe})$ from different selected areas. The scale bars are 25 nm.

Highly La-rich compositions in large LCO crystals (see Figure 26: $\text{La}/\text{Co} = 3.8$) suggest that La_2O_3 -like phases are present as secondary phases. At 20 at.% Fe, La-rich particles (Figure 26: $\text{La}/(\text{Co}+\text{Fe}) = 1.7$) can be related to the A_2BO_4 -type Ruddlesden–Popper phases. At 40 and 60 at.% Fe, 20–40% of La-enrichment can be attributed to the presence of the $\text{A}_4\text{B}_3\text{O}_{10}$ -type Ruddlesden–Popper phases. It is noteworthy that La-deficient areas are also visible in the composition of the LCO and the 20 at.% Fe. Overall, local EDX measurements not only support the results extracted from XRD, but also enabled the identification of minor content of La-deficient phases, which are hardly to be detected by diffraction measurements.

Table 3: Element ratio derived from the overall EDX measurement of the constituent elements using dark-field STEM.

Sample	$\text{La}/(\text{Co}+\text{Fe})$	$x_{\text{Fe}} = \text{Fe}/(\text{Co}+\text{Fe})$
LCO	1.14	-
LCFO 20 at.% Fe	1.13	0.21 ± 0.04
LCFO 40 at.% Fe	1.10	0.40 ± 0.03
LCFO 60 at.% Fe	1.18	0.58 ± 0.04

5.1.3 Surface chemical structure, composition and oxidation states

The as-prepared nanoparticles were further investigated using ATR-FTIR spectroscopy in order to identify organic and inorganic chemical groups. (Figure 27). At high wavenumbers between 4000–2500 cm^{-1} , all the samples show similar absorption bands which can be attributed to the asymmetric and symmetric stretching vibration of C–H groups (2957, 2922, 2871, and 2852 cm^{-1}).⁸² Between 1550–1000 cm^{-1} , the absorption bands correspond to the asymmetric and symmetrical stretching vibration of O–C=O groups (1547 and 1419 cm^{-1}). In the same range, the asymmetric and symmetric deformation vibration of C–H groups were also detected (1465, 1374, 1292 cm^{-1}).¹⁰⁵ The small bands at 1077 and 1008 cm^{-1} were attributed to the stretching vibrations of C–O groups.¹⁰⁶

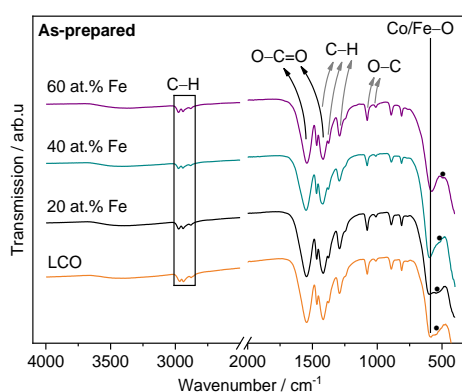


Figure 27: ATR-FTIR spectra of as-prepared $\text{LaCo}_{1-x}\text{Fe}_x\text{O}_4$ perovskite nanoparticles. Identified functional groups are marked. The black dots indicate the secondary Co/Fe–O-related band detected at 550–497 cm^{-1} .

Overall, these bands show rather similar patterns compared to the IR spectra of acetate groups reported by Chen et al.¹⁰⁷ Thus, the observed acetate groups most likely remain from the precursors and carboxylate groups from the solvent used in the spray-flame synthesis. In addition, the relative band intensities of the already mentioned functional groups are similar and therefore they are not dependent on the Fe content. At lower wavenumbers (600–400 cm^{-1}), the detected bands can be assigned to Co/Fe–O bonds. For LCO and 20 or 40 at.% Fe, the bands were found to locate at 590, 598, and 595 cm^{-1} , respectively, and these values are consistent with those reported for LaCoO_3 -type perovskites.¹⁰⁸ However, at 60 at.% Fe, the dominant absorption band is visible at 579 cm^{-1} , a value previously attributed to the Fe–O stretching vibration.¹⁰⁹ In addition to the abovementioned bands, a second band was identified at 550, 538, 525, 497 cm^{-1} for LCO and the materials with 20, 40, and 60 at. % Fe, respectively. This second band at about 550 cm^{-1} in the FTIR spectra of LCO can be attributed to that of LaCoO_3 -type perovskite as well.¹⁰⁸ Also, with increasing Fe concentration, the decreasing wavenumber of the second bands (dots in Figure 27) and overall transition of doublet bands to the single band was already mentioned in a previously reported IR spectrum of $\text{LaCo}_{1-x}\text{Fe}_x\text{O}_3$ perovskites.¹¹⁰ These findings imply the changes in the Co–O bond properties with increasing Fe substitution.

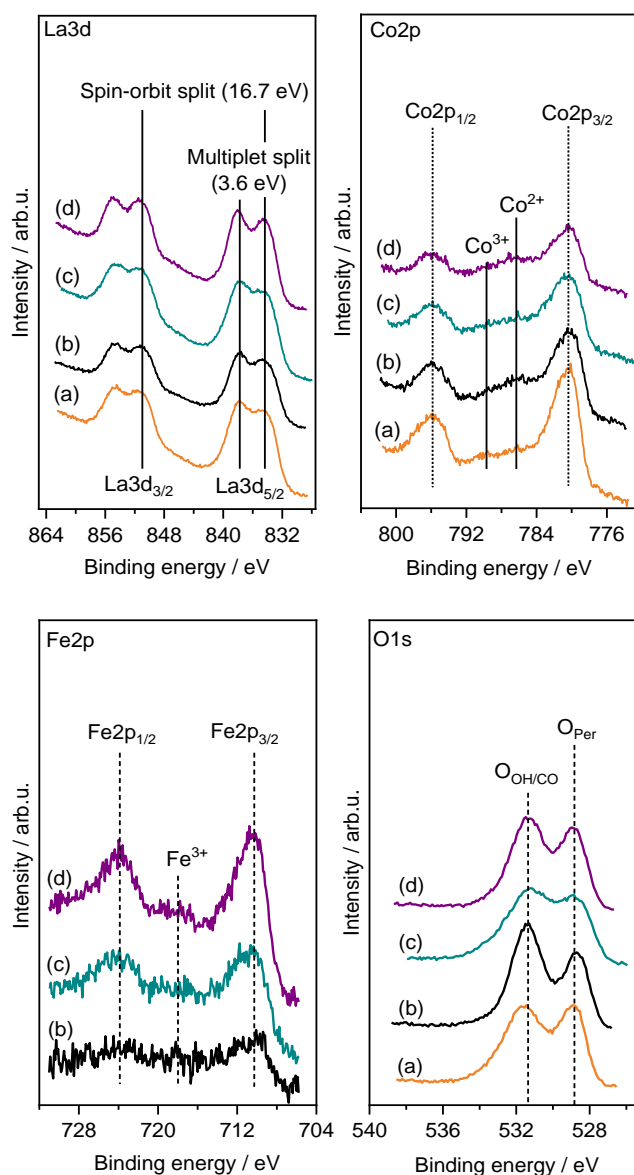


Figure 28: Al-K α -based La 3d, Co 2p, Fe 2p, C 1s and O 1s XP spectra at 0 at.% Fe (a), 20 at.% Fe (b), 40 at.% Fe (c), and 60 at.% Fe (d). The exhibited Fe 2p spectra were obtained by subtraction of the Co Auger peaks from the raw Fe2p spectra, which is measured by Dr. Ulrich Hagemann in Interdisciplinary Center for Analytics on the Nanoscale (ICAN).

Moreover, surface properties of the as-prepared nanoparticles were examined by analyzing the high-resolution X-ray photoelectron spectra (XPS) to find out the surface chemical species and/or the oxidation state of the involved transition metals. In Figure 28, the La 3d spectra were analyzed by examining the spin-orbit components. The spin-orbit splitting of 16.7 eV was observed at all samples and can be attributed to the spectral features of perovskite-like structures.¹¹¹ However, the measured multiplet splitting of \sim 3.6 eV deviates from the typical multiplet splitting of stoichiometric perovskite structures (\sim 4 eV) and shows similarity to the splitting observed in La₂CoO₄-type Ruddlesden–Popper structures.¹¹² Also, these multiplet splitting values were found to be highly analogous to the previously reported XP spectra of La₂O₃ and water exposed La compounds.^{113,114} For this reason, the contribution of the LaOOH phase to the overall La3d spectra, as found from XRD analyses of LCO, 20 at.% and 40 at.% Fe (Figure 24), cannot be excluded.

Co 2p and Fe 2p high-resolution XPS were also analyzed. According to Co 2p XPS, the binding energies of Co 2p_{3/2} (780.5 eV) and Co 2p_{1/2} (795.9 eV) peaks correspond to oxidized Co species like CoO or Co₃O₄.¹¹⁵ Moreover, the presence of satellite peaks at 786.3 and 789.8 eV suggests the presence of Co²⁺ and Co³⁺, respectively. The higher intensity of the satellite peak at 786.3 eV compared with the one at 789.8 eV indicates a higher amount of Co²⁺ ions on the catalyst surface.

In Fe2p XPS, the low intensity of the Fe 2p peaks for 20 at.% Fe makes the precise assignment of the Fe oxidation state difficult. Still, two weak signals can be noticed at ~709.7 and ~711 eV, which can be assigned to a mixture of Fe²⁺ and Fe³⁺.¹¹⁶ The increase in Fe content leads to a shift of the Fe 2p_{3/2} peak towards higher binding energy, which can be related to a higher amount of Fe³⁺ ions on the 60 at.% Fe nanoparticle surface. The satellite features observed in the 40 and 60 at.% Fe samples (at ~718.2 eV) further support the presence of Fe³⁺ ions.^{116,117} In addition, the difference in the binding energy of Fe 2p_{1/2} and Fe 2p_{3/2} was calculated as ~13.5 eV for all Fe-containing samples. This value is also in agreement with the peak splitting of Fe³⁺ ions reported for perovskite materials.¹¹⁸

The O 1s spectra mainly show two XPS signals at different binding energies. The high signals at ~528.8 eV can be attributed to the characteristic peak of the perovskite oxygen anions^{118,119}. The second oxygen signal at ~531.3 eV is usually attributed to surface OH groups, carbon-related oxygen groups, O₂⁻ and low-coordinated oxygen groups.¹²⁰ Yet, since no OH-related band was observed in the FTIR spectra of all samples, the influence of surface OH groups on O1s spectra can be excluded. The intensity of O1s at ~531.3 eV relative to those at 528.8 eV show a correlation with the increase in the signals of Co²⁺ ions relative to Co³⁺ in the Co2p spectra. This correlation implies that CoO or perovskite compounds that can stabilize high Co²⁺ concentrations, such as Brownmillerite or RP-type phases, are present at higher contents in 20 and 60 at.% Fe compared to other samples (Figure 28). Therefore, the O1s intensity at ~531.3 eV can be proposed as critical indication in the evaluation of the content of the secondary phases identified in the XRD patterns of the samples.

5.1.4 Electrocatalytic activity for water and ethanol oxidation

The electrocatalytic properties of the as-prepared nanoparticles for the oxygen evolution reaction (OER) and the ethanol oxidation reaction (EtOR) were investigated in collaboration with Swapnil Varhade, Corina Andronescu, and Wolfgang Schuhmann (RUB) to examine the catalytic activity of the samples. The LCO and the 20 and 40 at.% Fe-substituted nanoparticles showed similar OER activities (~1.64 V vs. RHE at a current density of 10 mA/cm). A lower OER activity was registered for 60 at.% Fe; namely, an overpotential of 40 mV was required for this sample to reach the same current density as of the other samples. (Figure 29a). The polarization curves, calculated based on the electrochemical surface area (ECSA), also show a similar trend to those based on geometric surface area (Figure 29c vs. Figure 29a). Similarly, for ethanol oxidation, the LCO and the 20, and 40 at.% Fe-substituted samples were found to be the more active catalysts than the 60 at. % Fe-substituted one (Figure 29b). The particular decrease in the OER and EtOR activity of 60 at.% Fe can be likely related to lower electronic conductivity of this sample compared to the others, as decreasing electronic conductivity of LaCoO₃ with Fe substitution was previously shown in literature¹²¹.

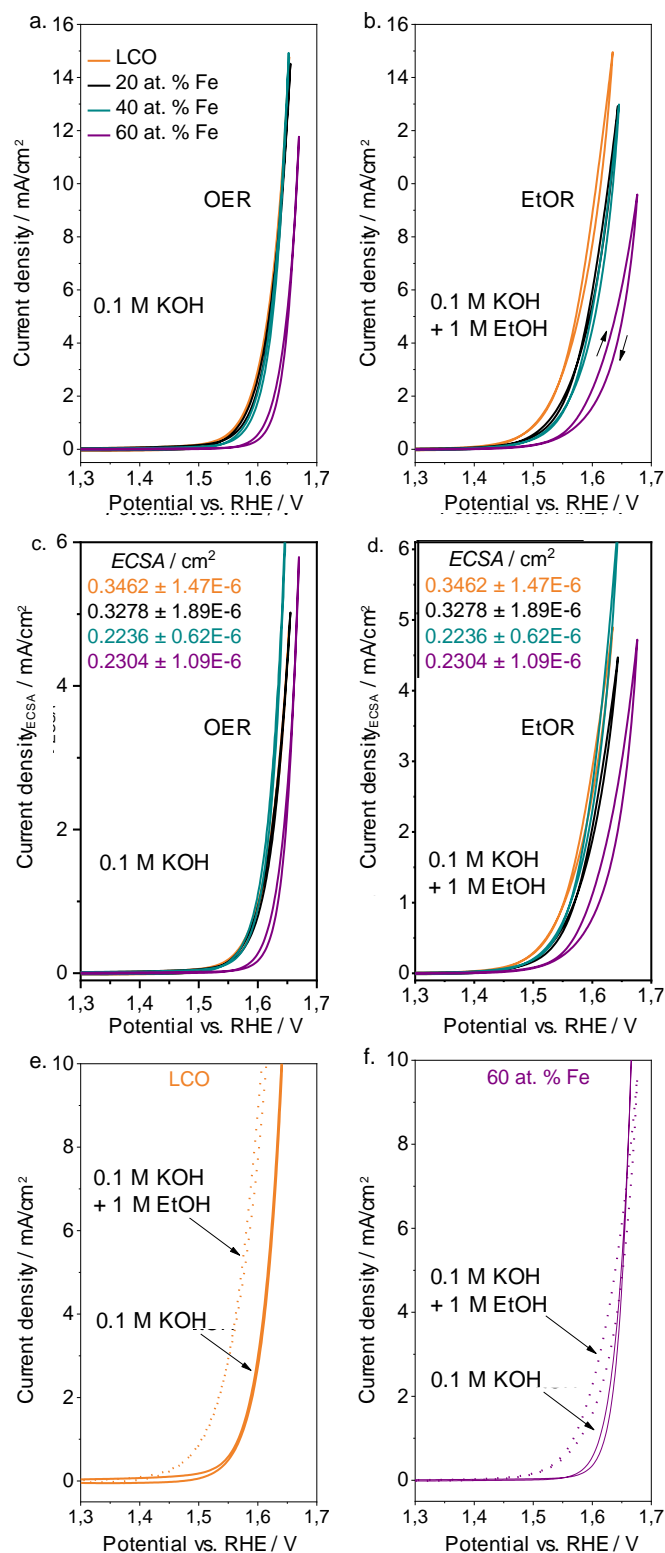


Figure 29: Cyclic voltammograms recorded in 0.1 M KOH (a,c) and 0.1 M KOH + 1 M ethanol (b,d) for LCO (black line), 20 at.% Fe (red line), 40 at.% Fe (blue line) and 60 at.% Fe (magenta line). Comparison of the performance of LCO (e) and 60 at.% Fe (f) in the presence (dashed line) and in the absence (solid line) of 1 M EtOH in 0.1 M KOH. All CVs were recorded with a scan rate 5 mV/s at a rotation speed of 1600 rpm. Current densities are calculated with respect to the geometric area of the electrode (a, b, e, f) or to the electrochemical active surface area determined from the double layer capacitance (c, d).

When the current is normalized by the geometric surface area of the electrodes, it was found that a gradual increase in the Fe content leads to a decay in the catalyst performance in EtOR. (Figure 29b), On the other hand, no significant difference was observed at LCO, 20, and 40 at.% Fe when the electrochemical surface area (ECSA) is used for normalization in the current density calculation (Figure 29d). Such a change implies that surface area and particle size of the samples have an influence on their EtOR activities and therefore gives importance to the interpretation of EtOR curves based on ECSA. Overall, for both normalization cases, a substantial decay was observed at 60 at.% Fe. Besides, lower currents were measured during the cathodic scan as compared to the anodic one. The decrease in the cathodic measurement suggests a partial blocking of the active catalytic sites. In the anodic scans, for LCO, the currents recorded in the presence of ethanol are higher than the ones in pure 0.1 M KOH (Figure 29e). However, at 60 at.% Fe, only slightly higher potentials are needed to achieve a current density of 10 mA/cm² when ethanol is present in the electrolyte (Figure 29f). This indicates that EtOR is the dominant process on LCO, while it is less pronounced in the case of 60 at.% Fe.

5.1.5 Operando electrochemistry/ATR-FTIR measurements

In order to find out which catalytic oxidation products form on the electrocatalyst surface during the EtOR, where different selectivity pathways exist leading to different products, *operando* electrochemistry/ATR-FTIR measurements were performed in collaboration with Steffen Cychy and Martin Muhler (RUB).⁸⁵ These measurements were conducted during ethanol electro-oxidation using LCO and 60 at.% Fe as electrocatalyst, since the two materials show considerably different performance in the EtOR according to the RDE experiments (Figure 29e, f).

The ATR-FTIR spectra recorded while applying a potential are presented in Figure 30 and are plotted as the logarithm of the reciprocal reflection, shortly $\log(1/R)$. Negative bands indicate the depletion of reactant species which is ethanol (black label). Vice versa, positive bands are related to generated species such as acetaldehyde (orange label) and acetate (red label) during the EtOR. Although the composition of the formed products is catalyst dependent, it is likely that acetate mainly is observed as the predominant product. Also, acetaldehyde is expected as intermediate product while C–C-bond scissoring products such as CO, CH₃, and CO₂ are hardly possible during ethanol oxidation.^{58,122}

Depletion of ethanol is clearly indicated by the negative band at 1045 cm⁻¹ assigned to the C–O stretching vibration of ethanol.^{109,123} The less intense negative band at 878 cm⁻¹ can be assigned to the C–C stretching vibration of ethanol. This band only becomes observable when positive product bands are also identified. In contrast, the negative C–O stretching vibration is also detected when product bands are no longer present or show very weak signals. This can be seen for both catalysts in the black colored spectra recorded at 1.38 V vs. RHE, which might be due to adsorption of ethanol on the catalyst surface so that less ethanol is detectable in the evanescent wave above the ATR-IR crystal. When the potential is increased by 100 mV to 1.48 V vs. RHE, positive bands (assigned to the antisymmetric and symmetric stretching vibration of the carboxylate group of acetate) are visible at 1552 and 1414 cm⁻¹,^{85,123} respectively, for the LCO catalyst. The less active catalyst (60 at.% Fe) does not show any significant positive bands at this potential after 20 min electrolysis. The earlier occurrence of product signals with use of LCO catalyst compared to 60 at.% Fe is in good agreement with the relatively lower overpotential for LCO exhibited in the voltammograms in Figure 29d.

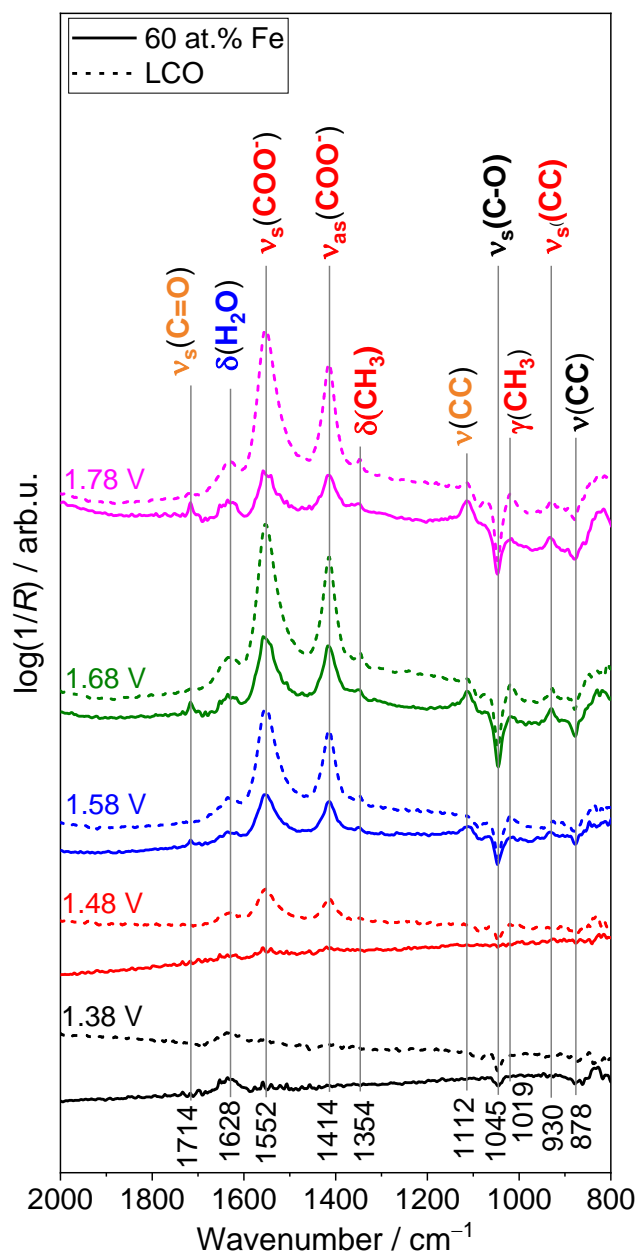


Figure 30: Operando electrochemistry/ATR-FTIR spectra obtained after 20 min electrolysis time in 1 M EtOH, 0.1 M KOH electrolyte at potentials between 1.38 V and 1.78 V vs. RHE at a distance of 20 μm between the ATR unit and the catalyst-modified working electrode. All potentials are referred to the RHE.

As water forms as a byproduct during the oxidation of ethanol, the scissoring vibration of water observable at 1628 cm^{-1} becomes visible. This vibration might be also caused by slight concentration fluctuations or changes of the local pH value within the thin electrolyte film between ATR-IR crystal and the electrode surface due to the consumption of protons and hydroxyl groups by the electrochemical reaction at the surface.¹²⁴ At a potential of 1.58 V vs. RHE, the IR spectra of both catalysts show the positive COO^- stretching vibrations at 1414 and 1552 cm^{-1} . They also exhibit acetate-related vibrations; namely, the CH_3 bending signals (at 1354 cm^{-1}), the rocking CH_3 (at 1019 cm^{-1}) and symmetric stretch C-C vibration (at 930 cm^{-1}). These additional bands become just visible because the formed acetate concentration is temporarily higher due to increased conversion rate of ethanol to acetate at the higher potential.

In addition to the acetate bands, acetaldehyde-related bands are observed for the 60 at.% Fe sample at 1714 cm^{-1} (C=O symmetric stretching vibration of acetaldehyde) and at 1112 cm^{-1} (symmetric C–C vibration) but not for LCO. These positive acetaldehyde bands indicate the longer lifetime of the primarily formed acetaldehyde before it is subsequently further oxidized. This situation can be compared with the blocking of active sites at higher reactant concentrations as reported by Lin et al.¹²⁵ for a concentration variation of ethylene glycol over a Pd-based electrocatalyst. Therefore, the observation of the presence of acetaldehyde is one further indication for the inferior activity of the 60 at.% Fe catalyst with respect to the EtOR. At the same time, blocking of the active sites at the catalyst surface may also explain the decreased activity of this catalyst towards the OER when ethanol is present as a reactant in the electrolyte.

The spectra recorded at a potential of 1.68 V vs. RHE are very similar to those recorded for 1.58 V vs. RHE, except that the intensity of all bands increases. However, indication of the presence of acetaldehyde is missing for LCO, except for a very weak shoulder at 1112 cm^{-1} , whereas the intensity of the related band indeed increases for the 60 at.% Fe sample. For the highest applied potential at 1.78 V vs. RHE, the acetaldehyde bands become visible for the LCO electrocatalyst, too. Thus, insufficient availability of oxidizing active surface species for the four-electron oxidation from ethanol to acetate is only reached at quite high potentials.

Furthermore, the overall intensity of the other product bands increases at 1.78 V vs. RHE, as compared with the previous potential steps. Contrary to this trend, when the 60 at.% Fe catalyst was used, a decrease of the positive acetate bands and negative ethanol bands are observed. Also, higher spectral noise is visible at the high potential applied likely due to evolving oxygen. These observations support the RDE measurements which indicate a lower EtOR and OER catalytic activity of 60 at.% Fe at the applied potentials up to 1.7 V vs. RHE (Figure 29f). On this catalyst, the OER seems to occur at substantially higher potentials. Compared to the OER activity of LCO catalyst, that of 60 at.% Fe seems to be suppressed to some extent in the presence of ethanol most likely because of competition for the active sites at the catalyst surface. This situation suggests that, during RDE measurements of 60 at.% Fe, the currents registered up to 1.7 V are mainly due to EtOR and not to the OER.

5.2 Investigation of the spray-flame process parameters

Previous part showed that spray-flame made Fe-substituted nanoparticles in the as-prepared state have two main problems as OER catalysts; multiphase formation and high content of unburnt organic combustion residuals. To overcome these problems, this chapter is based on the improvement of phase purity of stoichiometric perovskite phase and lowering of the combustion residual content. For this reason, in the beginning of this part, it was aimed to modify spray-flame process parameters/solvent characteristics and subsequently analyze the as-prepared nanoparticles by XRD and FTIR measurements. By these analyses, the most appropriate process parameters and solvent characteristics were determined based on which sample has the lowest content of secondary phases and combustion residuals in the as-prepared nanoparticles.

5.2.1 Correlation of spray-flame synthesis parameters and phase purity

In order to investigate the influence of Fe substitution on the OER catalytic properties of LaCoO₃ perovskite nanoparticles, it is critical to eliminate the formation of secondary, undesired phases during. Therefore, in this part, the effect of the spray-flame process parameters such as flow rate of dispersion O₂ gas, precursor flow rate and solution-based properties (e.g., relative volume ratios of solvents) on the phase composition of the as-prepared nanoparticles was analyzed. All other process parameters were kept fixed at a reactor pressure of 950 mbar with sheath and quench gas flows of 125 slm and 170 slm, respectively. The combined La, Fe, and Co concentration was 0.1M for all precursor solutions. As a representative sample, 20 at.% Fe substituted nanoparticles were used for these analyses.

Table 4 shows the different process parameters and solvent volume ratios utilized for their spray-flame syntheses. Each set is numbered from set 1 to set 3 and includes different mass flows of the dispersion O₂ gas, precursor flow rate, or different solvents with varying volumetric ratios. The as-prepared nanoparticles were investigated by XRD to identify the crystalline phases.

Table 4: Process parameters and volume ratios of the solvents used for the spray-flame synthesis of 20 at.% Fe-substituted LaCoO₃. Propionic acid is abbreviated as PA.

Set	Precursor rate (ml/min)	Dispersion O ₂ gas (slm)	Solvent volume ratios (PA:1-propanol)	Total concentration (M)
1	2	5	100 % PA	0.1
2	3	5	40:60	0.1
3	3	5	20:80	0.1

The process and solvent parameters of Set 1 were selected for the first experiment as these parameters have been reported for spray-flame synthesis of LaCoO₃ perovskites by Chiarello et al.⁸¹ Also, the another reason to select these parameters is that the reactor setup used in that report show high similarity to the reactor used in this study, except that they used a ring of small pilot flames to stabilize the main flame.⁷¹

Figure 31 shows the XRD result of the samples synthesized in various series. The as-prepared nanoparticles obtained with Set 1 parameters contain a considerable amount of secondary phases such as Brownmillerite phases (LaCo_{0.8}Fe_{0.2}O_{2.5±δ}) and RP-type phases (La₂Co_{0.8}Fe_{0.2}O_{4±δ}), which is confirmed by the high intensity of the diffraction peaks at 42–46° (see Figure A1). Also, metal oxide in minor contents (CoO and La₂O₃) are observed. The formation of such secondary phases can be due to the initially selected solvents and volumetric flow rate of the CH₄/O₂ pilot flame as well as volumetric flow rate of the dispersion O₂ gas and precursor flow rates.

The heat released from combustion of propionic acid per liquid solvent volume ($\Delta H_{cv} \approx -20.6$ kJ/cm³) and from the pilot flame of CH₄/O₂ (i.e., 1 slm/2 slm) is assumed to not provide a high enough temperature environment to promote a high evaporate rate of the droplets within the time required for precipitation of a solid product inside the droplets. Because oxidation is slower for large existing particles, the formation of fully oxidized materials (i.e., ABO₃) is hindered. This argument can likely explain the reason why the high content of oxygen-deficient perovskite phases such as Brownmillerite and RP-type

phase were found in the samples synthesized in set 1. In addition, it is possible that the initially selected flow rate of dispersion gas (O_2) and precursor flow rate are not appropriate for the formation of stoichiometrically oxidized perovskites. Overall, based on the argument in the previous paragraph, it was aimed to vary the process and solution parameters in a way to increase the flame temperature and see the resulting change in phase composition. For this purpose, 60 vol.% of the 1-propanol ($\Delta H_{cv} = 26.9$ kJ/cm³) is mixed with 40 vol. % of propionic acid while the total metal loading of La, Co, and Fe is kept at 0.1 M. Also, the gas-to-liquid mass ratio is decreased by increasing precursor flow rate from 2 ml/min to 3 ml/min so that higher flame temperature can be reached.

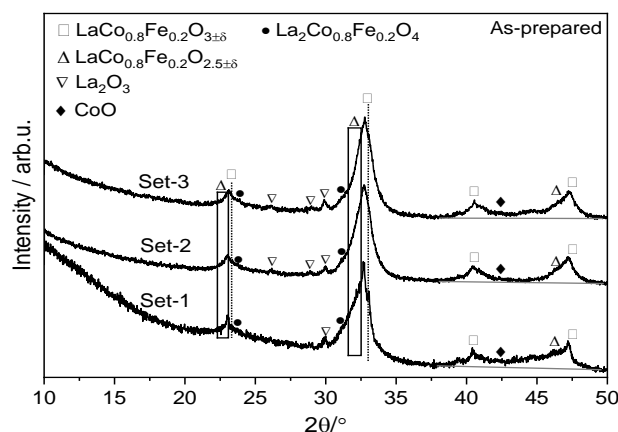


Figure 31: Comparison of the XRD diffraction patterns of the nanoparticles synthesized by the process parameters of Set 1, Set 2, and Set 3 consecutively. The detectable phases are Perovskite (●), Ruddlesden-Popper and Brownmillerite (◆), La_2O_3 (○), and CoO (△) respectively. Background lines were drawn to indicate the diffraction peaks between $2\theta \approx 42-46^\circ$.

Following these modifications, the XRD pattern of the sample in Set 2 show a significant increase in the content of the stoichiometric perovskite phase, which can be seen by the increasing peak intensity at $\sim 32.9^\circ$. Also, the single oxide phases found in Set-1 patterns was largely eliminated in the Set 2 patterns, and only minor content of the diffractions between $2\theta \approx 26-30^\circ$ and $2\theta \approx 42-45^\circ$ was observed. Regarding other perovskite-like phases, the both Brownmillerite and RP type phases are still visible in Set 2 spectra but their phase content exhibit reducing diffraction intensities at $2\theta \approx 30.5-32.5^\circ$ and $45.5-47^\circ$, which implies higher content of the stoichiometric perovskite phase.

Also, the propionic acid/1-propanol volume ratio was modified from 40/60 to 20/80 to further increase the overall ΔH_{cv} of the solvents (Set 3). By this way, the influence of the ΔH_{cv} of the solvents on the phase composition of as-prepared nanoparticles was investigated. The resulting XRD patterns show no detectable change in secondary perovskite-like phases but the content of La_2O_3 and CoO phases slightly increases. This increase in the La_2O_3 phase content can possibly arise from precipitation of La_2O_3 in the precursor solution during the synthesis, due to lower volume of propionic acid in the solution. Overall, the Set 2 based as-prepared nanoparticles have the highest perovskite content and therefore they were investigated for materials characterization, and post-treatment studies in the following part.

5.2.1.1 Phase and chemical structure analyses

Figure 32 exhibits the effect of Fe content on phase composition in the XRD patterns (the Set 2-based patterns, solid lines). For comparison, Cu- K_α -scanned XRD patterns of the previously studied samples

in Figure 24 (20 at.% Fe, dotted lines) are shown. Apparently, the disappearance of the diffraction peaks between $2\theta \approx 42\text{--}46^\circ$ indicates that the CoO and La_2O_3 phases were largely eliminated from the overall phase content. At all Fe contents, the main diffraction peaks are attributed to those of the $\text{LaCo}_{1-x}\text{Fe}_x\text{O}_{3\pm\delta}$ and $\text{LaCo}_{1-x}\text{Fe}_x\text{O}_{2.5\pm\delta}$ phases. Also, La_2O_3 is observed in minor contents. In addition, the XRD peaks shift to lower diffraction angles at higher Fe contents. This shift implies the substitution of the Co by Fe. Besides, sharp and single diffraction peaks (indicated by black arrows) are observed at 60 at.% Fe. Although the diffraction angles of these peaks well match with those of both rhombohedral and orthorhombic perovskite structures, the presence of only a single peak at the highest intensity suggest orthorhombic structure is more dominant at 60 at.% Fe. Overall, this finding is in agreement with the structural change from rhombohedral to orthorhombic perovskite crystals reported at high Fe contents.¹⁰²

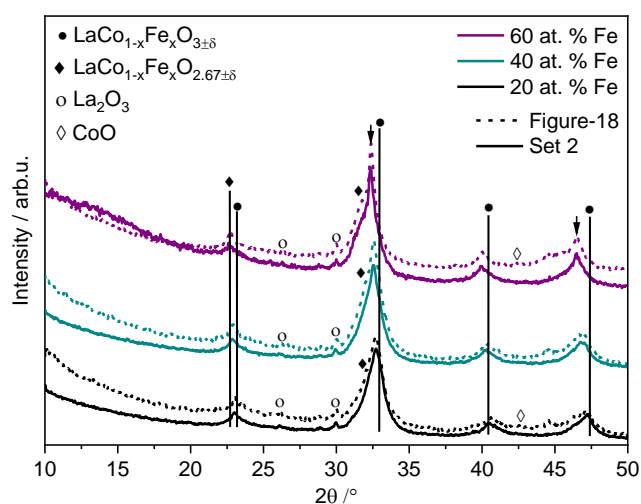


Figure 32: Comparison of the XRD patterns of the as-prepared nanoparticles (Set 2) with respect to Fe-substitution at 20, 40, and 60 at.%. The detectable phases are Perovskite (●), Ruddlesden-Popper and Brownmillerite (◆), La_2O_3 (○) respectively. Black arrows indicate the diffraction peak specific to orthorhombic structure of perovskite at 60 at.% Fe.

The combustion residuals and inorganic groups in the Set-2 based samples (solid lines) and the previously studied samples (in Figure 27, dashed lines) were investigated using the corresponding ATR-FTIR spectra in Figure 33. The same functional groups of O–H, O–C=O, and C–H groups appear in both spectra. Compared to the intensity of the Co/Fe–O bands, the total band intensity of these groups considerably lower in the Set 2-based spectra. This indicates the increasing content of perovskite-related bands at these samples. Besides, the signals between 400 and 750 cm^{-1} correspond to the absorption bands related to cobalt and iron sites. The bands at 589 cm^{-1} can be attributed to the octahedral coordination of Co/Fe ions, and they match with the typical absorption band in rhombohedral LaCoO_3 perovskites.^{126–128} Although the intensity of these bands are similar in all spectra, the intensity of the second band at 535 cm^{-1} shows a decrease at higher Fe content. The band at 535 cm^{-1} can be attributed to a low symmetry band of the rhombohedral LaCoO_3 structure.¹²⁹ The decreasing intensity of this band at higher Fe contents indicates that the chemical composition of the rhombohedral LaCoO_3 crystals changes with Fe substitutions.

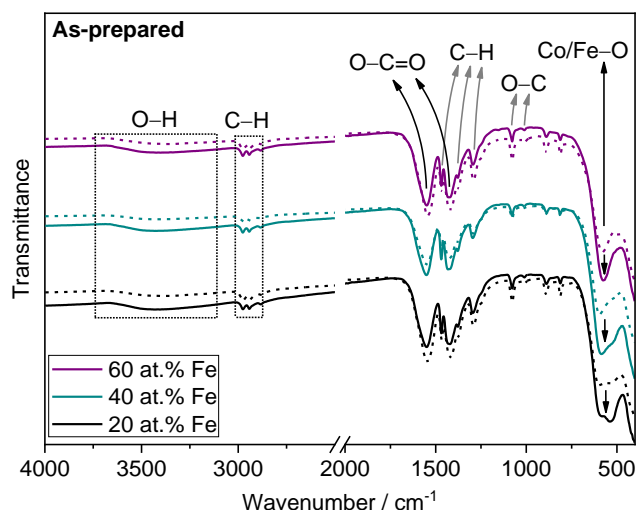


Figure 33: ATR-FTIR bands associated with the functional groups in the as-prepared powders with respect to Fe substitution. All spectra were normalized relative the maximum transmittance, and they were drawn such that the baseline of carboxylate bands overlap. Arrows indicate the increasing band intensity of the Co/Fe–O. Dotted lines indicate the FTIR spectra shown before (see Figure 27) and the solid lines show those of the as-prepared nanoparticle with the Set 2 parameters.

5.2.1.2 Thermal analyses

In order to clean the perovskite samples from combustion residuals found in FT-IR results, heating them at a controlled atmosphere can be an appropriate method. In this respect, it is needed to know how these residuals release from the samples when being exposed to increasing temperatures at the selected atmosphere. For this purpose, TGA and DSC measurements were performed to investigate thermal properties of the perovskite samples. As the previous FT-IR measurements indicate the presence of similar content of the organic species in the all samples, the thermal measurement were made only on one sample (40 at.% Fe-substituted LaCoO_3) under air atmosphere and their results are exhibited in Figure 34. These measurements were also coupled with mass spectrometry to research the molecular species released from the nanoparticles at different temperatures. The TGA curve indicates a total mass loss of about 12 wt.% until 600°C , and shows no further changes after this temperature. Moreover, QMS results in Figure 35 indicate that the main species detected are H_2O ($m = 17, 18$) between the room temperature and 800°C , and CO_2 ($m = 44$) at $\sim 150\text{--}300^\circ\text{C}$. In this regard, the overall decreasing weight of the sample can be explained by releasing of high amount of H_2O from the sample. On the other hand, the prominent DSC signal between $150\text{--}300^\circ\text{C}$ can be related to burning of hydrocarbon combustion residuals, and formation of CO_2 as supported by QMS measurements. Based on the results of the thermal characterization, the as-prepared nanoparticles were heated at 250°C (where most of DSC signal was observed), at 450°C (where DSC signals ended) and at 600°C (where almost no mass loss was observed). Influence of Fe-substitution at different heating temperatures were then investigated.

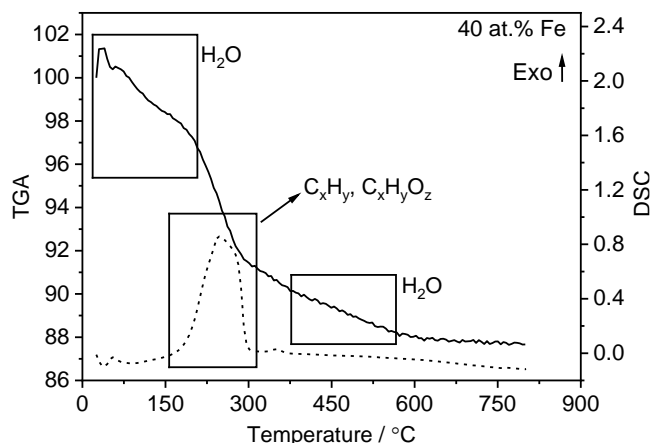


Figure 34: TGA and DSC curves of 40 at. Fe-substituted LaCoO_3 (solid and dashed curves, respectively), indicating the critical temperature intervals where most combustion residuals are removed. The thermal measurement was applied with heating rate of $5^\circ\text{C}/\text{min}$ under air atmosphere.

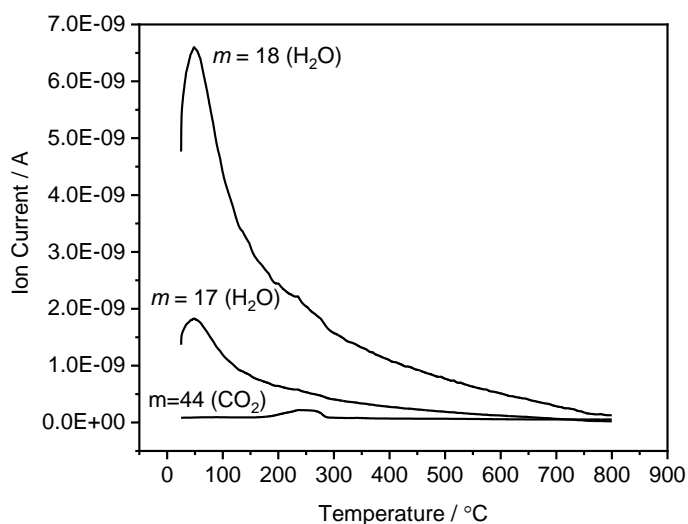


Figure 35: The QMS results obtained during the TGA measurement of 40 at.% Fe-substituted LaCoO_3 . H_2O and CO_2 are detected as the most prominent species.

5.2.2 The heat-treated $\text{LaCo}_{1-x}\text{Fe}_x\text{O}_3$

Despite the Set 2-based samples being the most suitable as-prepared samples in terms of phase purity, they still have considerably high content of combustion residuals, and thus the second part of this chapter was devoted to their heat-treatment at varying heating temperatures in O_2 to eliminate the combustion residuals. For this reason, the Set 2 based as-prepared nanoparticles were heated at 250, 450, and 600°C for 3 h under O_2 gas. In this way, it was intended to find out how chemical structure, crystalline phases, particle characteristics, surface and magnetic properties of the Fe-substituted nanoparticles were altered with heat treatment in O_2 . In the end of this chapter, the findings from these characterizations were overall summarized and the influence of Fe substitution content and heating temperature on the OER activities of the heat-treated perovskite nanoparticles were discussed.

5.2.2.1 Chemical structure

The FT-IR spectra of the heat-treated samples in O₂ were measured in order to identify organic and inorganic species present in the samples (Figure 36). The FTIR region at 3670–2620 cm⁻¹ is attributed to broad bands of structural water. The very weak band at about 3690 cm⁻¹ indicates some hydroxyl groups formed at all the heated samples. Following the heating, the most of the C-related combustion residuals are no longer present in the samples, and the absorption bands of carboxylate (O–C=O) and carbonate (CO₃) were only detected in the FTIR region between 1600 and 1200 cm⁻¹. The bands at 1494 and 1378 cm⁻¹ are attributed to those of O–C=O while the slightly shifted bands at 1346 cm⁻¹ correspond to those of CO₃ groups. Besides, the total band intensities of these two groups were observed to diminish after the as-prepared samples were heated to 250, 450, and 600°C.

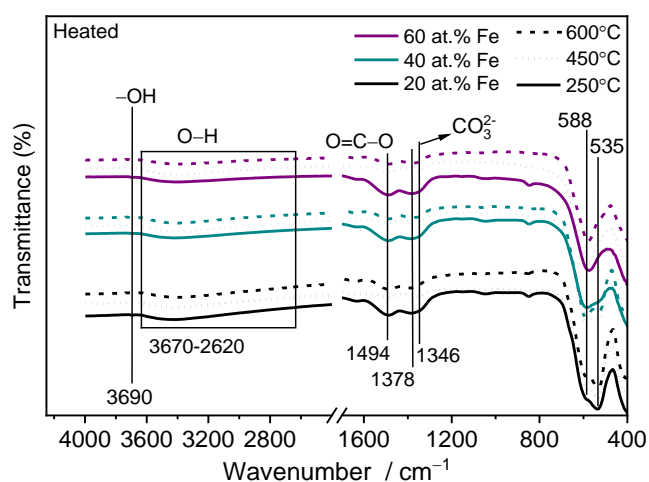


Figure 36: ATR-FTIR spectra showing the detected functional groups of the Fe-substituted LaCoO₃, which are heated samples at 250, 450, and 600°C under O₂ for 3 h.

Cobalt and iron-related bands are also present at 750–400 cm⁻¹. Similar to the FTIR spectra of the as-prepared samples, the broadened bands at 588 and 535 cm⁻¹ were observed at 20 and 40 at.% Fe. These bands are attributed to the octahedral coordination and low symmetry bands of the Co–O vibrations in LaCoO₃, respectively. In contrast, one dominant band at 579 cm⁻¹ was mainly observed at 60 at.% Fe. This band well corresponds to the Fe–O stretching vibration, meaning the Fe–O bonds begins to become more dominant than the Co–O bonds at 60 at.% Fe. In the spectra of the samples heated at 450 and 600°C, well-separated and narrower bands are visible at all Fe-substitution levels. This can be related to the increasing crystallinity of the samples due to heating. Overall, the ATR-FTIR spectra of cobalt and iron-specific bands mainly show similar absorption band patterns at varying heating temperatures. Rather than heating temperature, different Fe contents can be considered to have a major influence on the IR bands.

Table 5: The assignment of the different organic groups at the heated perovskite nanoparticles.

ATR-FTIR bands / cm^{-1}	Functional Groups
3697	OH-stretching frequencies ¹³⁰
3650-2640	OH stretching vibration corresponding to structural water ¹³¹
2921, 2850	C-H stretching mode ¹³²
1636	Monodentate carbonate ¹³³ / $\delta(\text{HOH})$ ¹³²
1486	The carbonates groups similar to La_2O_3 ¹³⁴ / adsorption of CO_2 ¹³⁵
1380	The carbonates groups similar to La_2O_3 ¹³⁴
1359	Symmetric vibration of C-O ¹³²
1041	Adsorption of CO_2 ¹³⁵
847	The carbonates groups similar to La_2O_3 ¹³⁴

5.2.2.2 Crystalline phases

Figure 37a exhibits the influence of heating on the change in the phase composition of the 20 at.% Fe-substituted samples. Heating them at 250°C in O_2 increases the phase fraction of the stoichiometric $\text{LaCo}_{0.8}\text{Fe}_{0.2}\text{O}_{3\pm\delta}$ perovskites. This can be attributed to the oxidation of $\text{LaCo}_{0.8}\text{Fe}_{0.2}\text{O}_{2.5\pm\delta}$ Brownmillerites. At the heating temperature of 450 and 600°C, the diffraction peaks of the $\text{LaCo}_{0.8}\text{Fe}_{0.2}\text{O}_{3\pm\delta}$ perovskite become more dominant. This result suggests that 450°C is a sufficiently high temperature for obtaining highly phase-pure perovskite. Also, the main diffraction peaks of La_2O_3 ($2\theta \approx 30^\circ$) in the as-prepared nanoparticles transform to those of LaOOH (raising $2\theta \approx 27.0^\circ$, ICSD: 60675). This transformation can be related to the release of hydrocarbon groups from La_2O_3 leading to unprotected surfaces, which allows to adsorption of hydrate species to La_2O_3 to form LaOOH phases. This finding draws attention to the high sensitivity of the La_2O_3 -based phases to the heating environment due to hydroscopic nature of La compounds.

Furthermore, Figure 37b shows the XRD patterns of the samples with different Fe contents that were exposed to different heat treatments in O_2 . The increasing Fe content was observed to induce higher phase content of the $\text{LaCo}_{1-x}\text{Fe}_x\text{O}_{2.5\pm\delta}$ Brownmillerites ($2\theta \approx 30\text{--}32^\circ$). This result can be attributed to the higher structural stability of the Brownmillerite phases at more Fe contents as it was reported. Therefore, especially at 60 at.% Fe, heating the samples up to 600°C is needed to make the perovskite phase dominant phase. Besides, the shift in the diffraction peaks towards lower 2θ values is observed at higher Fe contents and indicates the higher content of the Fe substitution in the $\text{LaCo}_{1-x}\text{Fe}_x\text{O}_{3\pm\delta}$.

Moreover, the diffraction peaks of $\text{La}_2\text{Co}_{1-x}\text{Fe}_x\text{O}_3$ RP-type phase are observed at all Fe contents and heating temperatures. The formation of these phases and La-based single oxides together were observed to be coupled with the formation of Co_3O_4 phases at $2\theta \approx 37^\circ$ (see the main diffraction peaks of Co_3O_4 phases in Figure A2). Here it is assumed that Co_3O_4 phase is not pristine but most likely contain certain degree of Fe substitute as no Fe-specific phase was detected from the XRD patterns. Overall, the formation of the La-rich phases in the presence of the Co-rich phases can be due to maintaining the overall atomic ration of $\text{La}/(\text{Fe}+\text{Co})$.

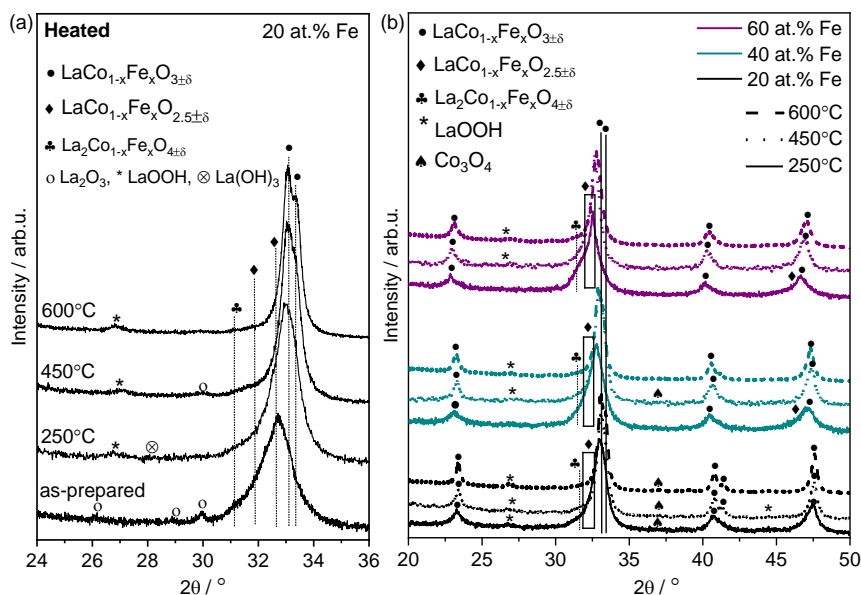


Figure 37: XRD patterns of the heated powders at different Fe substitutions. Phase transformation from rhombohedral to orthorhombic upon Fe substitution is shown in the inset.

Despite the qualitative phase analyses by XRD measurements, the overlapping diffraction peaks in them do not allow the quantitative analyses of perovskite and other phases. In order to make quantitative structural analyses, the selected area electron diffraction (SAED) patterns of each sample were obtained by TEM measurements. The SAED patterns were converted into the radial profile plots, which are used to extract the corresponding interplanar spacings (i.e., d-spacings) as described in Figure 38. Because the samples heated at 450 and 600°C show rather similar d-spacing values, only the d-spacings of the ones heated at 250 and 450°C were tabulated in Table 6. For the analyses, the calculated d-spacings values were compared to those of the reference perovskite and perovskite-like structures found in the ICSD database, which are tabulated in Table A1.

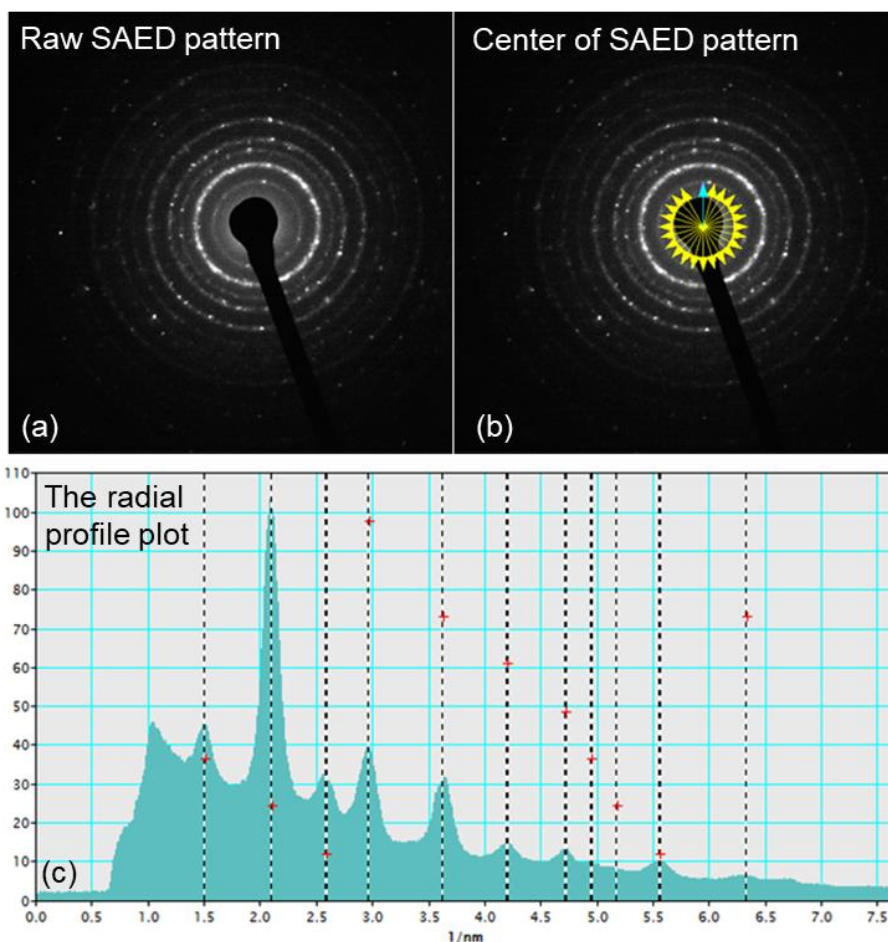


Figure 38: The single SAED pattern obtained from a large amount of the particles (a) and the radial profile plot calculated from it (c) for a representative sample, the heated-treated $\text{LaCo}_{0.8}\text{Fe}_{0.2}\text{O}_3$ at 250°C . After locating the center of the SAED pattern (b), it is rotational averaged to obtain the radial profile plot, and then to measure of d-spacings at the selected peak positions. DiffTools add-in in Digital Micrograph software was used for the processing of the SAED patterns.

At 20 and 40 at.% Fe, the calculated d-spacings were found similar to those of rhombohedral $\text{LaCo}_{0.8}\text{Fe}_{0.2}\text{O}_3$ (ICSD: 190099) and $\text{LaCo}_{0.5}\text{Fe}_{0.5}\text{O}_3$ (ICSD: 245179) perovskites, respectively. These results suggest the analyzed peaks from SAED patterns can be most likely attributed to perovskite phase at these Fe concentrations, which is in agreement with XRD results. On the other hand, for the heated-treated sample at 250°C , the d-spacings at 60 at.% Fe were found considerably higher than those at 20 and 40 at.% Fe. Moreover, they show the best match with those of pristine $\text{La}_2\text{Co}_2\text{O}_5$ (ICSD: 51198) Brownmillerite phase. Here, it is essential to note that only the structural details of pristine $\text{La}_2\text{Co}_2\text{O}_5$ is available in ICSD database. It can be assumed that Fe substitution on the reference $\text{La}_2\text{Co}_2\text{O}_5$ phase can have a marginal effect on its d-spacings because the ionic size of Fe^{3+} ($r_{\text{Fe}} \approx 0.645\text{\AA}$) substitute is rather similar to that of Co^{2+} ($r_{\text{Co}} \approx 0.650\text{\AA}$) ions in $\text{La}_2\text{Co}_2\text{O}_5$.¹³⁶ Therefore, the d-spacings in the reference $\text{La}_2\text{Co}_2\text{O}_5$ were not expected to change dramatically with Fe substitution. Under this assumption, the measured d-spacings at 60 at.% Fe can be also likely attributed to 60 at.% Fe substituted $\text{La}_2\text{Co}_2\text{O}_5$.

When the d-spacings of 60 at.% Fe substituted crystals were compared at 250 to 450°C , a noticeable decrease in their values are observed. This decrease can be related to the oxidation of Brownmillerites to perovskites, as noted in the XRD analyses. Indeed, the measured d-spacing values at 60 at.% Fe most

likely confirm the presence of $\text{LaCo}_{0.4}\text{Fe}_{0.6}\text{O}_3$ perovskite having rhombohedral or orthorhombic structures.

Overall, the evaluation of the XRD and d-spacing analyses suggest that perovskite phases are dominant at 20 and 40 at.% at all the heat-treatment temperatures. Similarly, the results from both analyses indicate that perovskite phases are dominant at 60 at.% at 450 and 600°C. On the other hand, for the heat-treated samples at 250°C, the secondary phases identified in the XRD pattern of 20, 40, 60 at.% Fe samples (Figure 37b) can be mostly attributed to Brownmillerite phase as found by their d-spacing analyses. Based on these results, the abovementioned XRD patterns was investigated with profile refinement analyses to estimate the phase fractions and crystallite size of the perovskite and Brownmillerite phases. For crystallite size calculations, the particle shape was assumed spherical.

Table 6: Extracted d-spacing values of $\text{LaCo}_{1-x}\text{Fe}_x\text{O}_{3\pm\delta}$ annealed at 250 and 450°C. Precision of the values are in the range of 0.01 Å.

Heat treatment temperature /°C	Relative intensity (%)	Interplanar <i>d</i> -spacings / Å		
		20 at.% Fe	40 at.% Fe	60 at.% Fe
250	36	3.8272	3.8660	3.9256
	100	2.7124	2.7564	2.7968
	31	2.2131	2.2358	2.2758
	30	1.9160	1.9404	1.9988
	30	1.5646	1.5907	1.6159
450	76	3.8465	3.8653	3.8660
	100	2.7172	2.7569	2.7614
	44	2.2067	2.2321	2.2326
	43	1.9208	1.9428	1.9478
	26	1.5614	1.5808	1.5874

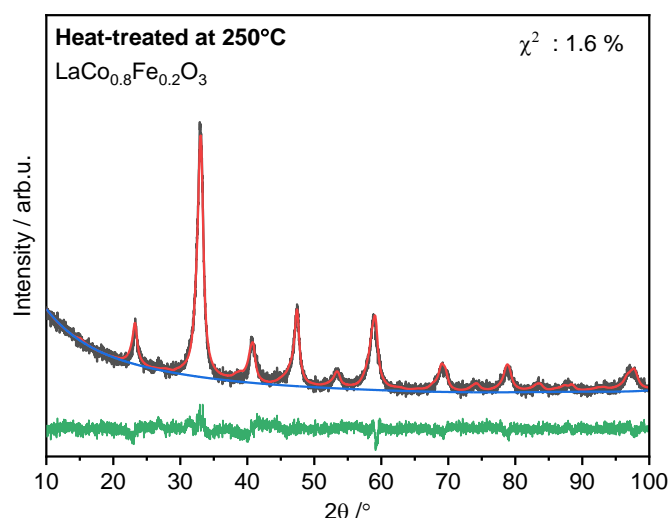


Figure 39: The refinement plots of the XRD patterns of 20 at.% Fe-substituted LaCoO_3 . Experimental, simulated, background and difference plots were indicated by black, red, blue, and green lines. R_{wp} indicates weighted R -factor, which is used to measure convergence of the refinement.

Figure 39 shows the XRD profile refinement plots of the 20 at.% Fe-substituted LaCoO_3 (see Figure A3 for the other refinement plots). The obtained R_{wp} values at about 2.9% imply that the experimental XRD pattern is well defined with the simulated pattern using only the crystallographic phases of $\text{LaCo}_{0.8}\text{Fe}_{0.2}\text{O}_3$ perovskites and $\text{LaCo}_{0.8}\text{Fe}_{0.2}\text{O}_{2.7}$ brownmillerites. These two phases were also used for the profile XRD refinement of most of the other samples. Only for the 60 at.% Fe-substituted sample heated-treated at 250°C , the $\text{LaCo}_{0.8}\text{Fe}_{0.2}\text{O}_{2.7}$ and $\text{LaCo}_{0.8}\text{Fe}_{0.2}\text{O}_{2.5}$ Brownmillerites were involved in the profile refinement to define high degree of secondary phases present in their XRD patterns. Due to the low phase fractions of the Ruddlesden-Popper and single oxide phases ($< 5 \text{ wt.}\%$) in the heat-treated samples as observed in the qualitative XRD analyses (see Figure 37), they were not involved in the whole profile fitting.

Table 7 tabulates the refinement results showing the relative phase fractions and crystallite sizes of the abovementioned phases. For the samples heat-treated at 250°C , the refinement can be reliable due to low χ^2 between 1.3-1.7 % and their results confirm the overall increasing phase fractions of $\text{LaCo}_{1-x}\text{Fe}_x\text{O}_{2.7}$ and $\text{LaCo}_{1-x}\text{Fe}_x\text{O}_{2.5}$ brownmillerites with increasing Fe substitution.

Besides, the crystallite sizes of the $\text{LaCo}_{1-x}\text{Fe}_x\text{O}_3$ perovskite were found more than twice bigger than those of $\text{LaCo}_{1-x}\text{Fe}_x\text{O}_{2.5}$ brownmillerite phases. The individual crystallite sizes were also proportioned to the corresponding phase fractions in order to find out the volume based mean crystallite sizes. They were found to well match with the volume-based mean particle size obtained from the TEM measurement, which will be shown in the next part.

Table 7: Results of XRD refinement for heat-treated samples, showing the estimated phase fractions and crystallite sizes. As the crystallite sizes measured from XRD measurements are based on the sample volume, the number-based TEM particle sizes shown in Figure 40 were converted to volume-based particle sizes for comparison.

Heating temperature	250°C			450°C		
At. % Fe	20	40	60	20	40	60
Phase Fractions / wt. %						
LaCo _{1-x} Fe _x O ₃	44	30	-	54	38	60
LaCo _{1-x} Fe _x O _{2.7}	28	27	47	46	62	17
LaCo _{1-x} Fe _x O _{2.5}	28	43	53	-	-	22
Crystallite Size / nm						
LaCo _{1-x} Fe _x O ₃	14.1	11.9	-	20.1	21.5	14.8
LaCo _{1-x} Fe _x O _{2.7}	14.3	7.5	11.2	10.8	11.6	13.4
LaCo _{1-x} Fe _x O _{2.5}	4.2	4.4	4.7	-		6.9
Volume based mean XRD crystallite size / nm	~ 8.8	~ 7.5	~ 8.2	~ 15.7	~ 15.3	~ 13.5
Volume based mean TEM particle size / nm	~ 8.6	~ 8.1	~ 7.4	~ 13.9	~ 17.9	~ 9.7
χ^2	1.6	1.3	1.9	1.8	1.7	1.7

XRD profile refinement of the samples heat-treated at 450°C show the similar results to those heat-treated at 250°C, except that the measured crystallite sizes of the perovskite and brownmillerite phases increase explicitly. The volume based mean crystallite sizes were also found to show slight deviations from the mean particle sizes measured in TEM measurements. These deviations can be likely related to the reason that the TEM measurement can most likely represent smaller particles in the samples while XRD based analyses are more representative for the whole sample. Overall, the qualitative phase analyses, the SAED measurement results and the profile pattern refinements agree with one another in that the Brownmillerite phase content increase with different Fe substitutions.

5.2.2.3 Particle size distribution, shape and atomic arrangement

As mentioned in the previous part, TEM micrographs were used to find out the particle size and size distribution of the nanoparticles at different Fe and heating temperatures. Figure 40 and Figure 41 indicate the measured number based mean particle size values (d_p) and geometric standard deviations (σ_g). As will be seen in Figure 42, most particles heat-treated at 250 °C have either octahedral or hexagonal crystal shapes; therefore, the diagonal distances in these crystals were measured to represent the crystal

size and shape in a most proper way. As for the most particles heated-treated at 450 and 600 °C, the nanoparticle shapes turn into a spherical form, thus, the diameter of the particle shape was considered for the particle size analyses. Besides that, all the particles analyzed in TEM measurements were observed to have single crystalline structure; therefore, being compared to the XRD crystal size.

Accordingly, from the lognormal fitting of the particle size histograms, the geometric standard deviations (σ_g) were found in the range of 1.3–1.5. These values indicate asymptotic self-preserving size distributions in all the samples.¹⁰³ Heat-treated nanoparticles at 250°C results in a highly homogenous particle size distributions, and the number based mean particle sizes (d_p) were calculated around 7.3–8.1 nm. These values were found to be similar to the d_p values of the as-prepared nanoparticles that range between 6.9–8.4 nm (Figure A4), and suggest that heat-treatment at 250°C do not cause a considerable change in the overall mean particle sizes.

It is here necessary to remind that the number based d_p values were measured to be almost similar to the volume based d_p . Thus, either number or volume based d_p , the d_p of the heat-treated nanoparticles at 250°C do not show a good match with the crystallite sizes of $\text{LaCo}_{1-x}\text{Fe}_x\text{O}_3$ perovskites (~11.9–14.1 nm) as can be seen in Table 7. Instead, they are closer to the crystallite sizes of $\text{LaCo}_{1-x}\text{Fe}_x\text{O}_{2.7}$ or $\text{LaCo}_{1-x}\text{Fe}_x\text{O}_{2.5}$ brownmillerites (~4.2–4.7 nm); therefore, TEM images for the heat-treated nanoparticles at 250°C can be more representative for the mixture of perovskite and Brownmillerite crystals. For the heat-treated nanoparticles at 450°C, the mean particle sizes increase and get closer to perovskite crystal sizes at 20 and 40 at.% Fe; thus, they most likely represent perovskite nanoparticle. For 60 at.% Fe, the nanoparticles in the TEM image can be representative for the mixture of Perovskite and Brownmillerite phases as the d_p values were measured between their crystals sizes.

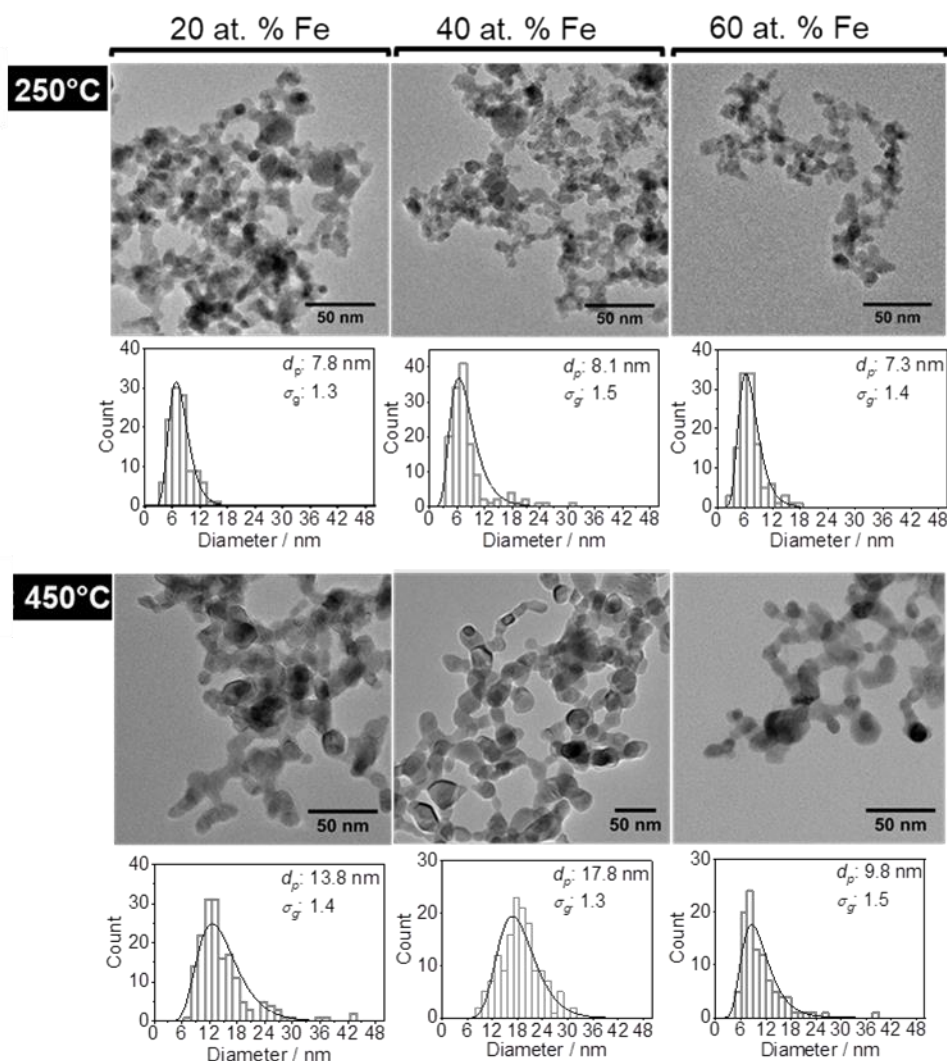


Figure 40: TEM micrographs and lognormal size distribution of 20, 40, and 60 at.% Fe substituted nanoparticles heated at 250, 450, and 600°C, respectively. The number-based primary particle size and geometric standard deviation obtained from log-normal fitting are given in the histograms.

The influence of the heating temperature on particle sintering is shown in Figure 41. For the as-prepared samples, the TEM images indicate point contacts between the nanoparticles, and therefore suggests the formation of agglomerates (Figure A4). For the samples heat-treated at 250°C and 450°C, most of the nanoparticles were found in the aggregated state and the TEM images overall show the agglomeration of these aggregates. These results indicate the particle sintering occurs between the nanoparticles with heat treatment. The another critical change in the TEM images of 20 and 40 at.% Fe is that the heat-treated samples at 450°C contain substantially larger nanoparticle than those at 250°C. For 60 at.% Fe, the increase in the d_p of the nanoparticles were found less pronounced, but particle necking between the nanoparticle is clearly visible in the TEM images in Figure 41, which imply increasing degree of sintering in the samples exposed to higher heat treatment temperatures.

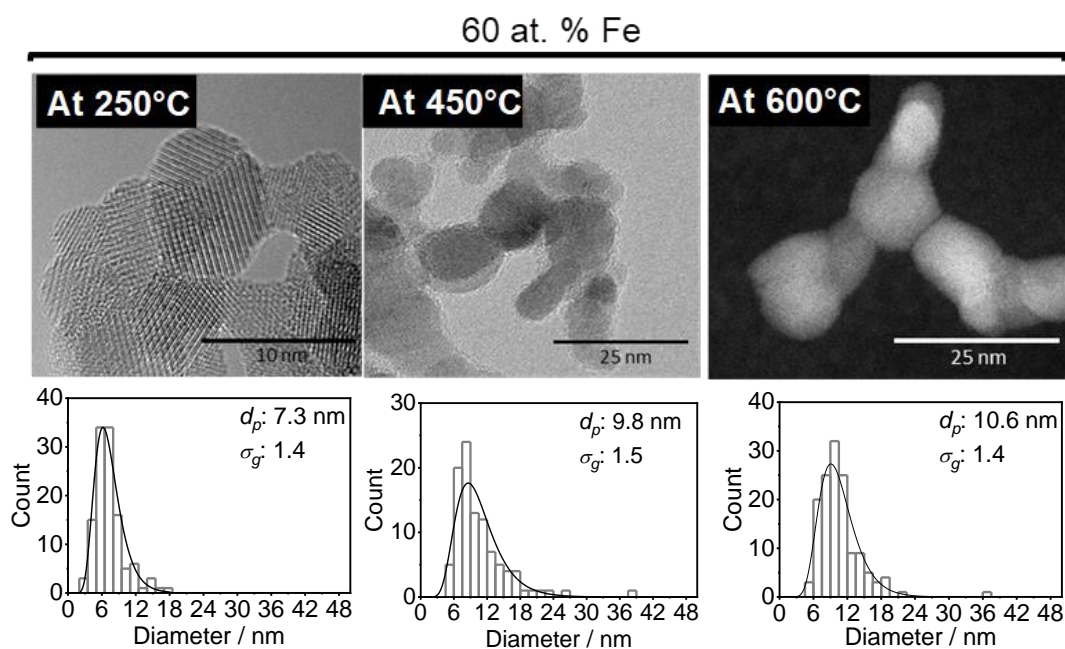


Figure 41: Representative 60 at.% Fe-substituted perovskite nanoparticles with corresponding particle size distribution after heating them at 250, 450, and 600°C.

HAADF-STEM images of the heat-treated nanoparticles are shown in Figure 42. All the nanoparticles are observed in either octahedral or hexagonal shapes. These shapes most likely originate from the rhombohedral crystal structure of the $\text{LaCo}_{1-x}\text{Fe}_x\text{O}_{3\pm\delta}$ perovskites as this crystal structure is found in the hexagonal crystal family. In addition, highly ordered crystal facets were detected in the HRTEM image at 60 at.% Fe (Figure 42c). These ordered structures can be related to the atomic-scale twinning in the crystals as previously being observed in mixed oxide $\text{LaSrCo}_{0.5}\text{Fe}_{0.5}\text{O}_{3-\delta}$ perovskites.²³ The cation ordering mechanism between Co and Fe ions¹³⁷ can cause the formation of these perovskite structures at 60 at.% Fe. The HAADF-STEM images shown in insets exhibit the atomic structure of the crystals at different Fe contents. The observed atomic arrangements can be attributed to those of perovskite and Brownmillerite crystals oriented in $\langle 001 \rangle$, as previously shown by the simulated crystal structure of perovskites in Figure 25. However, the crystal size of the detected nanoparticles in the inset STEM images visibly ranges about 5–8 nm. These crystal size values show better agreement with those of Brownmillerites than perovskites, as seen in Table 7, and therefore the observed crystals can be most likely attributed to Brownmillerite structure oriented in $\langle 001 \rangle$. Overall, the observation of the ordered crystal facets together with Brownmillerite phases suggest that the origin of ordering in the crystal structure can be possibly due to oxygen vacancy ordering.

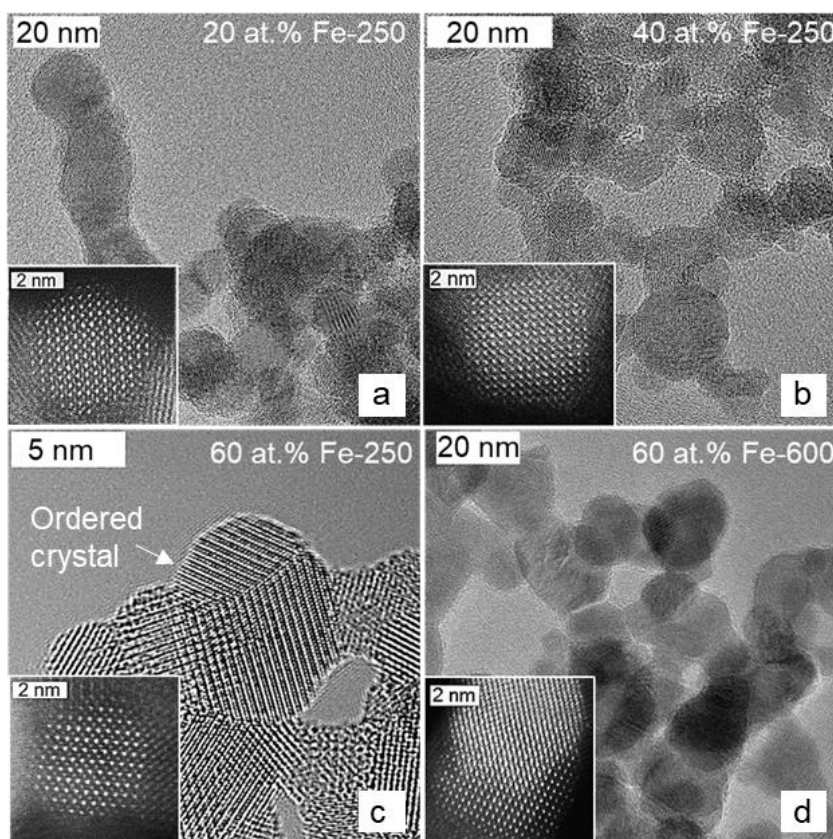


Figure 42: Morphology of the selected nanocrystals at different Fe substitutions and preparations (abbreviated as “x% Fe–temperature/K”). The insets indicate typical perovskite crystal structures, which were well documented for LaCoO_3 perovskites by the previous STEM analysis.¹³⁸

5.2.2.4 Surface oxidation states and compounds

Following structural and particle characteristics, the surface oxidation state and surface composition of the heated nanoparticles were determined by XPS measurements. Because the nanoparticles heated at 450 and 600°C were observed to have almost the same XPS spectra, only the results of those heated at 450 and 250°C are discussed below.

Figure 43 indicates the core-level and satellite signals of $\text{Co}2p_{3/2}$. At all Fe contents, the core-level signals at 779.5 eV and the satellite features at about 789.6 eV can be attributed to the Co^{3+} ions being observed in perovskites. In regard of the Fe content, the main difference in the XPS spectra is observed in the satellite features at 785.7 eV. These satellites are attributed to Co^{2+} ions and their increasing signal intensity at higher Fe content indicates the increasing amount of Co^{2+} ions. This increase in the Co^{2+} ions can be related to a higher content of Brownmillerite and/or perovskite having increasing degree of oxygen deficiency. This finding is especially observed for nanoparticles heated at 250°C because those heated at 450°C contain a high degree of Co^{3+} ions, and show no significant change in their $\text{Co}2p_{3/2}$ spectra.

In addition to the $\text{Co}2p_{3/2}$, $\text{Fe}2p$ spectra are shown in Figure 43. At all Fe contents and heating temperatures, the core-level signals at ~710.0 and 723.2 eV correspond well to those of the Fe^{3+} ions found in Fe-based perovskites.¹¹⁸ The satellites at 717.9–718.4 eV show a good match with those of Fe^{3+} . These Fe^{3+} signals can be attributed to Brownmillerites of $\text{La}_3\text{Co}_{3-x}\text{Fe}_x\text{O}_{8\pm\delta}$ and/or perovskite phases of LaCo_{1-x}

$x\text{Fe}_x\text{O}_{3\pm\delta}$ as they both have a high content of Fe^{3+} ions in their structures. Also, the signal at 724.2 eV (Fe^{3+} in oxygen-deficient structure) most likely corresponds to Fe-substituted Brownmillerites. Similar XPS signals were observed for Brownmillerites in a previous report.¹³⁹ Heating the nanoparticles from room temperature to 450°C causes a considerable decrease in the XPS signals at 724.2 eV and a slight increase in those at 710 eV. These changes most likely indicate the reducing content of Brownmillerite phase and increasing content of perovskite phases.

Besides, the core-level signals of iron at ~708.7–708.8 eV and the satellites at ~715.0–715.5 eV observed at Fe2p spectra of 20 at.% Fe in Figure 43, and they correspond to Fe^{2+} ions. The identified Fe^{2+} ions can be attributed to both, the Ruddlesden-Popper type phase $\text{La}_{2-y}\text{Fe}_{1-x}\text{CoO}_4$ and Brownmillerite ($\text{La}_2\text{Co}_{2-x}\text{Fe}_x\text{O}_{5\pm\delta}$) as the Fe^{2+} ions can be most likely present in these phases.

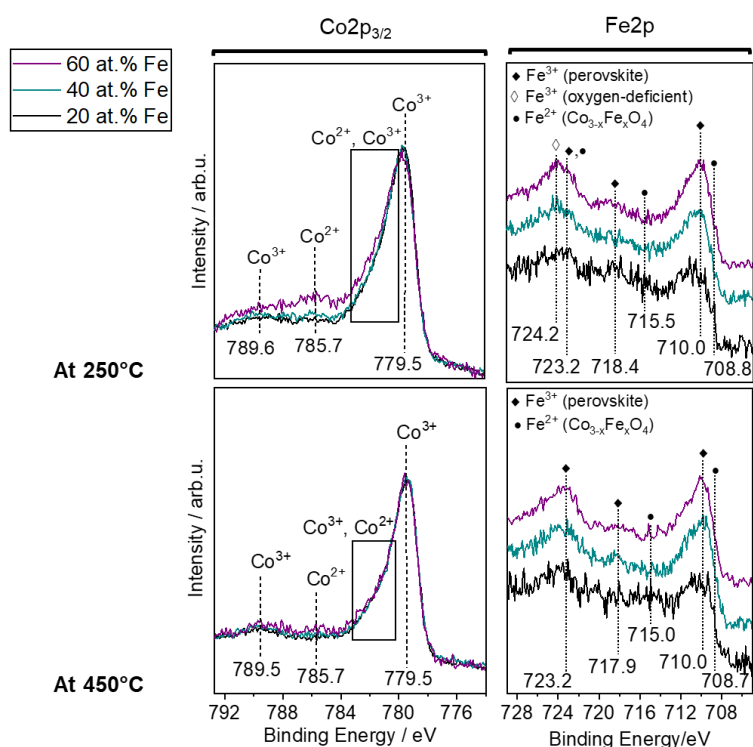


Figure 43: Al- K_{α} -based Co2p and Fe2p spectra of the samples at different Fe substitutions and heating temperatures.

O and La were also examined by the corresponding XPS measurements. Figure 44 shows the XPS spectra of the O1s and La3d. For all samples, the O1s spectra exhibit the characteristic lattice oxygen signal of perovskites at ~528.5–528.8 eV. Also, additional oxygen signals are observed at 531.1–531.5 eV. These signals can be attributed to the overall signals of surface hydroxyl oxygen, carbon-related oxygen, O^{2-} and low-coordinated ionic oxygen species.¹⁴⁰ Since the carbonate groups were already observed in the FTIR spectra of all heat-treated nanoparticles, the respective oxygen species of these groups are also expected at 531.1–531.5 eV. In addition to that, heating the nanoparticles from room temperature to 450°C leads to the O1s at ~528.5–528.8 eV peak to narrow. The broad signals at 528.8 eV at 250°C are most likely due to the overlapping O1s signals of several perovskite-like compounds. Therefore, the lower peak widths of these signals at 450°C implies the oxidation of perovskite-like phases to more stoichiometric perovskites. Besides, La3d spectra show the multiplet peak splitting of 4 eV at all Fe content. This is in good agreement with the characteristic multiplet splitting of perovskites. At the heating

temperature of 250°C, the La3d spectra also contain additional signals at 20 at.% Fe. They can be related to LaOOH or La(OH)₃ compounds because they are also observed in the XRD measurements. After heating to 450°C, the observed La3d signals can only be attributed to those of perovskite nanoparticles.

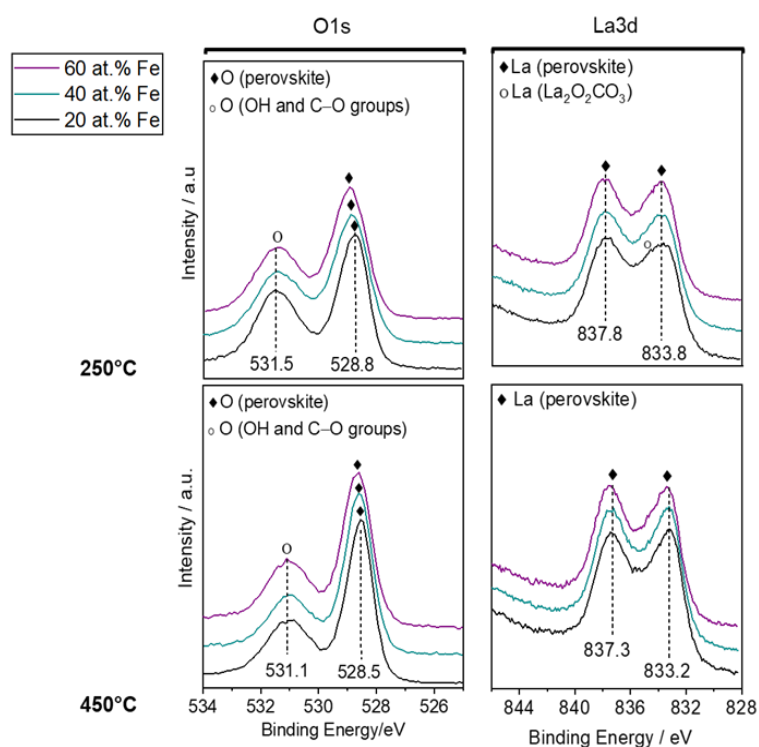


Figure 44: Al-K_α-based O1s and La3d spectra of the samples at different Fe substitutions and heating temperatures.

5.2.2.5 Magnetic state and bulk oxidation state of Fe

Following the surface-sensitive XPS measurements, Mößbauer measurements were performed to determine the magnetic state of the heated nanoparticles. Also, the oxidation state of Fe ions in the bulk of these nanoparticles was investigated using the same measurements. Figure 45 shows the room temperature Mößbauer spectra with respect to Fe contents and heating temperatures.

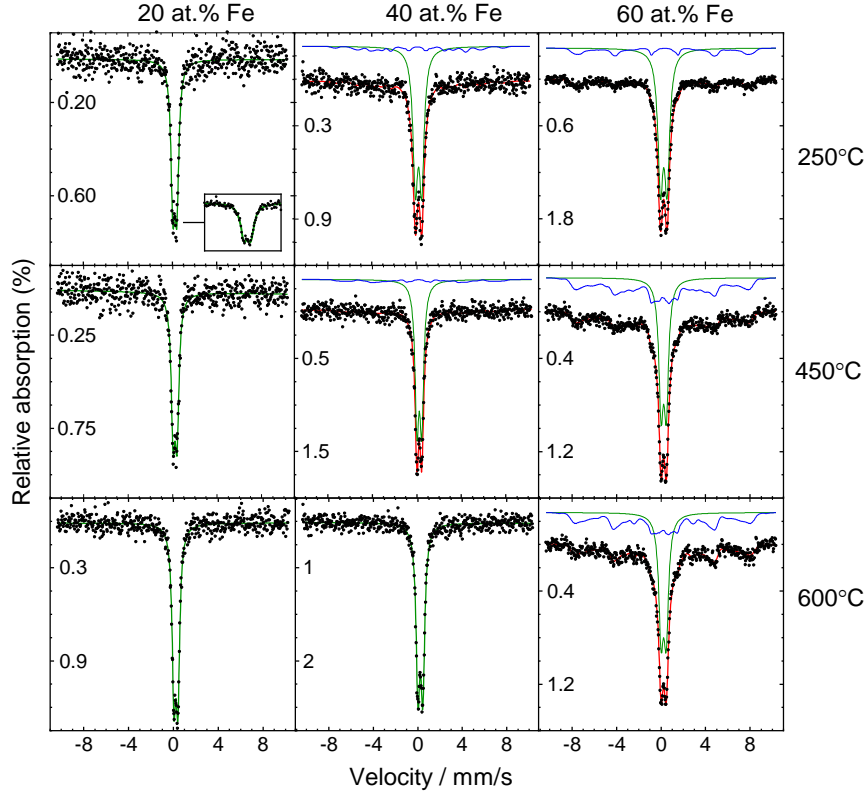


Figure 45: Room-temperature (300 K) Mössbauer spectra of the samples heated at 250, 450, and 600°C. The black dots indicate the measured spectra while red lines show total fitted spectra. Deconvoluted spectra of doublets and sextets are shown by green and blue. Inset figure at 20 at.% Fe is used to show the doublet spectra more clearly.

Accordingly, Figure 46 exhibits (super-) paramagnetic doublet fraction at 20 at.% Fe is about 100% independent of the heating temperatures. These doublets indicate the paramagnetic state in the 20 at.% Fe-substituted perovskites. This is in agreement with the result of the previously reported magnetization data of the Co- and Fe-based perovskites.¹⁰² At higher Fe contents and the same heating temperatures, an increase in the sextet fractions is found, and this increase indicates that perovskites have more magnetically ordered antiferromagnetic state.

Besides, a marginal decrease in the paramagnetic doublet fractions is observed when Fe content is changed from 20 to 40 at.% Fe, suggesting the samples at these Fe substitutions are mainly in similar paramagnetic state at all heating temperatures. In contrast, the doublet fraction at 60 at.% Fe decreases considerably (Figure 46) and the corresponding sextet fractions increase up to ~60 % at heating temperatures of 450 and 600°C. The increase in the sextet fraction at 60 at.% Fe at room-temperature Mössbauer measurements imply that the $T_{\text{Néel}}$ temperatures of 60 at.% Fe-substituted samples are above room temperature. This result is in agreement with a previous report that indicates the $T_{\text{Néel}}$ temperatures of 58 at.% Fe substituted LaCoO_3 is about 380 K¹⁰², and therefore explains why the antiferromagnetic sextets at 60 at.% Fe are present at high contents at the room-temperature spectra.

On the other hand, the prominent increase in the sextet fraction of 60 at.% Fe at the heating temperature of 450 and 600°C can be due to the increase in the $T_{\text{Néel}}$ of the samples heated at higher heating temperatures. It was reported previously that the $T_{\text{Néel}}$ considerably decreases from the bulk ($T_{\text{Néel}} \sim 229$ K) to

the surface regions ($T_{\text{Néel}} \approx 30$ K) at very small nanoparticles ~ 5 nm,¹⁴¹ and therefore point out influence of high surface area in the nanoparticles on the $T_{\text{Néel}}$. Since the surface area of the samples heated at 450 and 600°C are expected to be lower due to their higher mean particle sizes as indicated in Figure 41, the surface area effect on $T_{\text{Néel}}$ can be less pronounced at these samples. Thus, their overall $T_{\text{Néel}}$ are expected to be even higher than that of the samples heated at 250°C, and this relationship can explain why there is more antiferromagnetic sextet fractions observed at these samples. It is also necessary to note that influence of particle size on $T_{\text{Néel}}$ temperature is not observed for 20 and 40 at.% Fe, which can be due to the overall lower content of the sextet fraction detected in the room-temperature Mößbauer spectra of these samples.

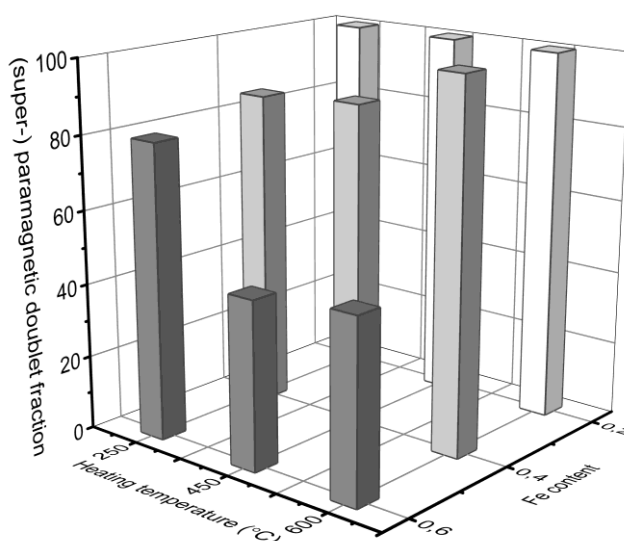


Figure 46: (Super)paramagnetic doublet fraction in the heated, Fe-substituted heated obtained from room-temperature (300K) Mößbauer spectra. For convenience, at.% Fe substitutions contents are displayed by atomic fraction of Fe (x_{Fe} in $\text{LaCo}_{1-x}\text{Fe}_x\text{O}_{3\pm\delta}$) at 0.2, 0.4, and 0.6.

In addition, the quadrupole splitting values corresponding to the doublets in the Mößbauer spectra are exhibited in Figure 47. Accordingly, they were found to increase at higher Fe content independent of the heating temperature. This increase in quadrupole splitting can be attributed to the increasing amount of micro-strain in the perovskite structure at higher Fe content. Besides, the quadrupole splitting values were found pronouncedly higher at 40 and 60 at.% Fe-substituted samples heated at 250°C. This notable increase in the quadrupole splitting can be associated with the influence of smaller particle sizes of these samples on the degree of microstrain. It was previously documented that higher degree of surface-induced lattice expansion occurs in the metal oxide nanoparticles having the smaller sizes.¹⁴² Thus, at 40 and 60 at.% Fe, it is expected that surface-induced lattice expansion occur in the samples heated at 250°C due to their relatively small particle sizes, and this expansion can be related to the increase in the quadrupole splitting values. At 20 at.% Fe, the quadrupole splitting did not show a noticeable change compared to those at 40 and 60 at.% Fe, and this result most likely suggest that there is not a significant contribution of micro-strain at Fe-substituted samples due to low Fe concentration.

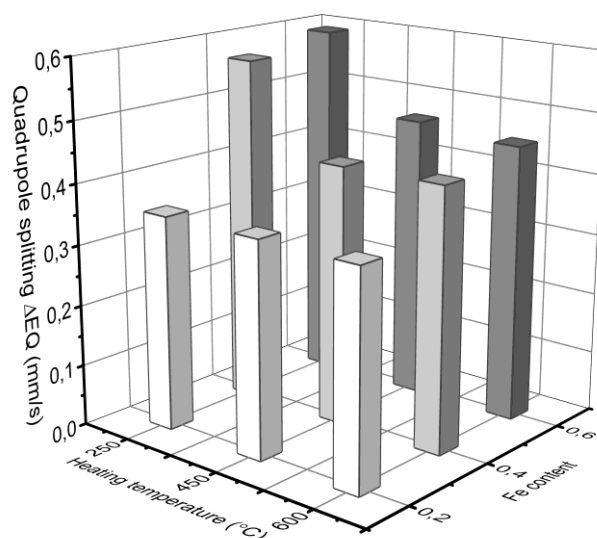


Figure 47: Quadrupole splitting with respect to extend of Fe-substitution and preparation temperature based on the room-temperature (300 K) Mößbauer spectra. Note that ordering of samples concerning their Fe content is reversed compared to those in Figure 46.

Furthermore, the analyses of Mößbauer subspectra, namely the deconvoluted doublet and sextet spectra in Figure 45, display comparable isomer shifts of about 0.31–0.35 mm/s. These values can be attributed to ferric Fe^{3+} compounds. As contributions of the Fe^{2+} ions correspond to much larger isomer shifts in the region of 0.9–1.3 mm/s, no considerable features with this isomer shift are visible in the Mößbauer spectra.⁹⁴ These results suggest that only Fe^{3+} are expected in the bulk of the all Fe-substituted samples.

5.2.2.6 Comparative OER activities of the heated samples and overall analyses

Following the material characterization, the OER catalytic activities of the heated nanoparticles were investigated by linear sweep voltammetry (LSV) measurements. Figure 48 exhibits the effect of Fe content on the polarization curves of the nanoparticles heated at 250°C. Figure 49 shows the respective potential values required to attain a current density of 10 mA/cm² and the standard deviations between the measurements. Accordingly, similar OER potentials of about 1.655 V at 10 mA/cm² were measured at 20 and 40 at.% Fe while the OER potential at 60 at.% Fe slightly decreases to ~1.64 V at 10 mA/cm². Despite the high standard deviations found at each Fe content, the average potential values indicate that the OER catalytic activities at 60 at.% Fe is slightly higher than those at 20 and 40 at.% Fe.

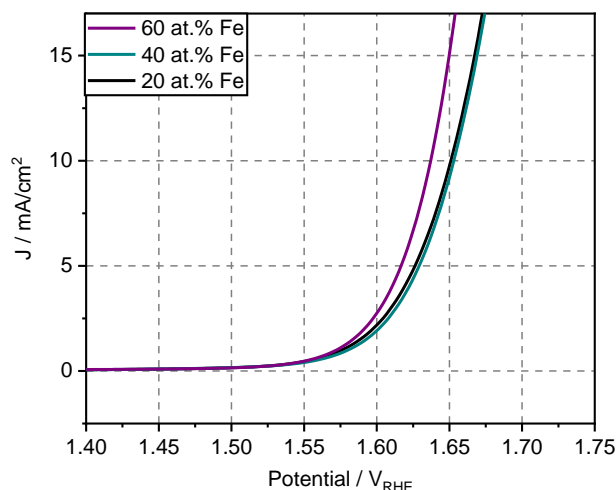


Figure 48: Linear sweep voltammograms (iR compensated) of Fe-substituted LaCoO_3 perovskites recorded in 1 M KOH at a scan rate of 5 mV/s and 1600 rpm electrode rotation, showing the OER activities of 60, 40, and 20 at.% Fe-substituted LaCoO_3 perovskite heat-treated at 250°C , with a catalyst loading of $210 \mu\text{g}/\text{cm}^2$ and using Nafion in the ink preparation. The single polarization curve for each Fe content correspond to the average curve of the three LSV measurements out of three different samples.

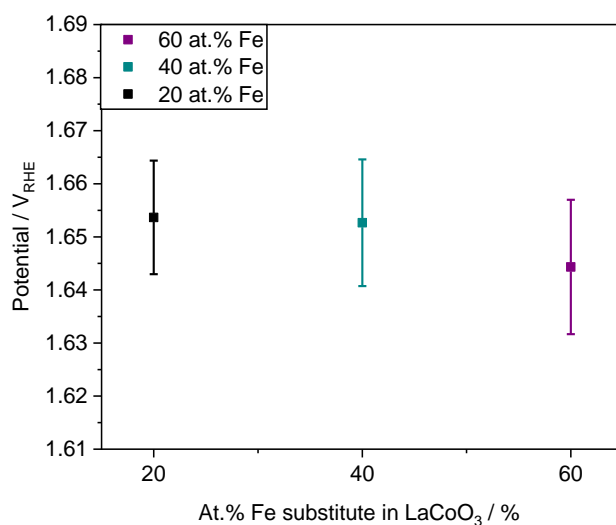


Figure 49: Summary of the OER activities of Fe-substituted LaCoO_3 perovskites expressed as the potential at a current density of $10 \text{ mA}/\text{cm}^2$. Three samples were considered and the error bars show the standard deviation of the measurements.

Moreover, the heated-treated samples at the same Fe concentration were studied in order to investigate the influence of phase composition at different heat-treated samples on the corresponding OER catalytic activities. Since the most noticeable change in the phase composition was observed at 60 at.% Fe-substituted perovskites (Figure 37b), LSV measurements were performed for these samples heated at different heating temperatures. The measured polarization curves are shown in Figure 50. The recorded potentials at $10 \text{ mA}/\text{cm}^2$ are also exhibited in Figure 51. The measured potentials were found to average around 1.645 V at $10 \text{ mA}/\text{cm}^2$, being independent of the heating temperature. These results indicate that the OER catalytic activity of the nanoparticles does not considerable change with the heating temperatures. This implies that the overall changes in the bulk, morphological, and surface properties of the

samples due to heating do not have an important effect on the OER activity. Instead, the Fe content plays a more important role in the OER catalytic activity.

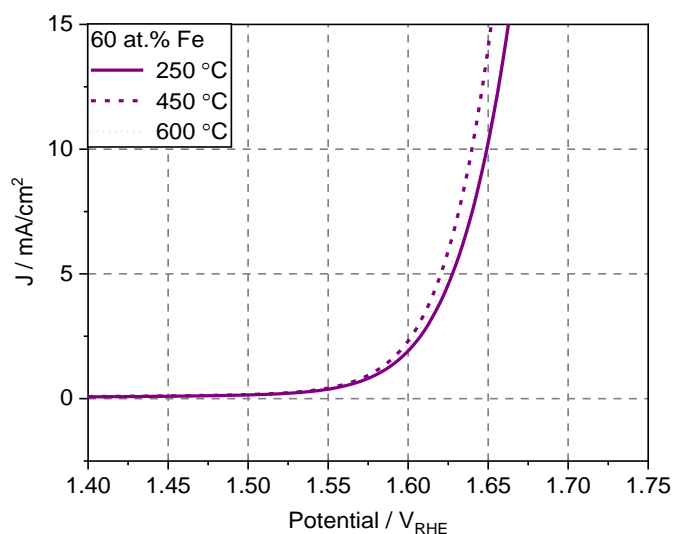


Figure 50: Linear sweep voltammograms (iR compensated) of Fe-substituted LaCoO_3 perovskites recorded in 1 M KOH at a scan rate of 5 mV/s and 1600 rpm electrode rotation, showing the OER activities of 60 at. % Fe-substituted LaCoO_3 heat-treated at 250, 450, and 600°C with a catalyst loading of 210 $\mu\text{g}/\text{cm}^2$ and using Nafion in ink preparation. The single polarization curve for each Fe content corresponds to the average curve of the three different LSV measurements out of three samples.

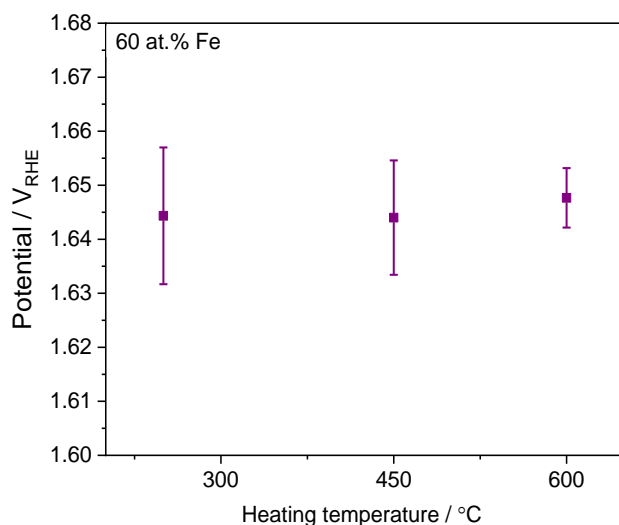


Figure 51: OER activities of Fe-substituted LaCoO_3 perovskites expressed as the potential at a current density of 10 mA/cm^2 . Three samples were considered and the error bars show the standard deviation of the measurements.

The most notable changes observed from the material characterizations and OER catalytic tests are summarized for the heated samples in Table 8. For the Fe-substituted samples heated at 250°C, the increasing content of surface Co^{2+} ions and octahedrally coordinated Co/Fe ions together with increasing degree of micro-strain can be more likely related to the higher OER activity of 60 at.% Fe. In a previous study on Co-containing oxides, the octahedrally coordinated Co^{2+} were found to be the reason for high activity for CO oxidation as they can easily oxidized.¹⁴³ Besides, the critical role of elastic strain on the formation

of oxygen vacancies in the both bulk and surface of the LaCoO_3 type perovskites was reported in a review paper, and the oxygen vacancies were described as the reactive sites towards OER.³⁷ Referring to these literature studies, the slightly higher OER activity at 60 at.% Fe can be explained by relatively higher surface Co^{2+} ions and distinctly higher microstrain at this composition than at 20 and 40 at.% Fe. Since Fe substitutes were found at Fe^{3+} oxidation state in the bulk and surface of all the samples heated at 250 °C, increasing content of Co^{2+} ions at 60 at.% Fe-substituted perovskite indicate higher degree of oxygen vacancy at their structure. This outcome can explain why 60 at.% Fe-substituted samples are slightly more active for OER.

For the 60 at.% Fe-substituted samples heated at 250, 450, and 600°C, no considerable variance in the catalytic OER activities were found as mentioned above. As shown in the XPS results, the surface Co^{2+} ions convert into Co^{3+} with heating at higher temperatures in O_2 , which imply lower concentration of surface oxygen vacancies. In addition, the heated-treated samples showed lower degree of micro-strain as found by their Mößbauer analyses, and this result also suggest the formation energy of oxygen vacancies lower in the bulk and in the surface. Besides, the increasing degree of particle sintering with heating at higher temperature is expected to have a detrimental effect on OER activities as it lowers the surface area of the nanoparticles thereby decreasing their catalytically active sites. However, with heat-treatments of the samples at higher temperatures, less carbonate contamination is also observed, and that most likely neutralize the detrimental effect of particle sintering on the OER, and leading to no detectable change in the OER activities.

Overall, heating the as-prepared nanoparticles above 250°C was found not to be necessary to improve the OER catalytic properties. On the other hand, following to spray-flame synthesis, low-temperature heat-treatment at 250°C is considered necessary to eliminate the combustion residual products so that the intrinsic catalytic activity of the perovskite/Brownmillerite phases can be compared. It is important to note that the OER activity of the heat-treated nanoparticles at 250°C are comparable with those synthesized by wet chemical techniques such as citrate complexation technique. That suggests the further improvement in the OER activity of the spray-flame made nanoparticles is necessary. Such an improvement can be realized with increasing phase content of stoichiometric perovskite-structured nanoparticles. The reason is that stoichiometric perovskites have much higher electrical conductivity than the Brownmillerite and Ruddlesden-Popper type phases and therefore the increase in their phase content can improve the overall OER activity.¹⁴⁴ Therefore, in the next chapter, a set of changes in the solvent and process parameters were additionally made in order to eliminate the single oxide secondary phases and increase the content of stoichiometric perovskite phase. Following to that, the as-prepared nanoparticles were heat-treated at 250°C in O_2 to eliminate the combustion residuals from the samples. Afterwards, the material and catalytic properties of both the as-prepared and heat-treated samples were compared in a systematic way.

It is necessary to mention that Fe substitution content in the next chapter was kept between 20 and 40 at.% Fe in order to synthesize rhombohedral perovskites. Although 60 at.% Fe-substituted nanoparticles heated at 250°C were found as the more active catalysts for the OER in this chapter, their crystal structure most likely contains the mixture of rhombohedral and orthorhombic structures. To eliminate any effect of different perovskite structures on the OER catalytic activities, the maximum concentration of Fe substitutes was limited to 40 at.%.

Table 8: Summary of materials characterization and catalytic activity tests.

Characterization techniques	Fe-substituted samples heat-treated at 250, 450, and 600°C	
	20, 40, and 60 at.% Fe heat-treated at 250°C	60 at.% Fe heat-treated at 250, 450, and 600 °C
	With increasing Fe	With increasing heat-treatment temperature
Chemical structure (FT-IR)	Less intensity of low-symmetry band of rhombohedral LaCoO ₃ and more intensity of octahedral coordination band observed	Decreasing content of carbonate groups
Phase composition (SAED, XRD profile refinement)	Increasing content of secondary phases mostly containing Brownmillerite phases	Decreasing content of Brownmillerite and other secondary phases
Particle characteristics (TEM)	No systematic change in the number and volume based mean particle sizes. Observation of ordered crystals at the highest Fe content	Higher degree of particle sintering
Surface chemistry (XPS)	Increasing content of surface Co ²⁺	Increasing content of Co ³⁺
Local structure of Fe (MS)	Higher fractions of magnetically ordered antiferromagnetic state. Higher values of quadrupole splitting, implying higher degree of micro-strain	Lower values of quadrupole splitting, implying lower degree of micro-strain
OER catalytic activity (LSV)	Slightly higher OER activities at 60 at.% Fe	No considerable change

5.3 High-purity as-prepared and heated LaCo_{1-x}Fe_xO_{3±δ} nanoparticles

It was aimed to further improve the phase purity of the LaCo_{1-x}Fe_xO₃ nanoparticles in the prepared state. Because organic precursors and solvents are used in spray-flame synthesis, organic residuals are often found on the as-prepared catalyst surface. Therefore, the as-prepared nanoparticles were heated to 250°C. To increase the phase purity of the nanoparticles in the as-prepared state, several modifications were made in the process/solvent parameters as shown in Table 9. Firstly, propionic acid ($\Delta H_{cv} = -15.3$ kJ/cm³) was replaced with octanoic acid ($\Delta H_{cm} = -30.3$ kJ/cm³) while the volume ratio of 1-propanol was kept constant. The aim was to increase the overall combustion enthalpy of the precursor solution and thus increasing flame temperature and accelerating droplet evaporation. This strategy was also shown to increase the content of stoichiometrically oxidized perovskites as described in Ref.⁸¹ In addition, the total precursor concentration of La, Fe, and Co was increased from 0.1 to 0.15 M and the volumetric flow rate of the CH₄/O₂ was systematically increased. The influence of these changes on the phase purity of the nanoparticles was examined by XRD measurements.

Table 9: The modification in the spray-flame process and solvent parameters.

Set	Solvent volume ratios	Total concentration / M	CH ₄ /O ₂ / (slm/slm)
(a)	Propionic acid / 1-propanol (20:30)	0.1	1/2
(b)	Octanoic acid / 1-propanol/water (20:30)	0.1	1/2
(c)	Octanoic acid / 1-propanol/water (20:30)	0.15	1/2
(d)	Octanoic acid / 1-propanol/water (20:30)	0.15	1.5/3
(e)	Octanoic acid / 1-propanol/water (20:30)	0.15	2/4

For the octanoic acid-based precursor solutions, firstly, octanoic acid was mixed with 1-propanol in a glass flask at room temperature and the solvent mixture was stirred for about 10 min. Then, the La, Co, and Fe salts were added. A small amount of water was added to fully dissolve the La-acetate. The flask was placed in a 75°C silicon oil bath under constant magnetic stirring for at least 2 h. The precursor solution in the series c–e was kept under stirring at 75°C during the spray-flame synthesis to prevent precipitation of the La precursor. For these precursor solutions, the total La and (Fe + Co) concentration was 0.15 M.

The influence of the abovementioned changes in the process and solvent parameters on the XRD patterns of the as-prepared nanoparticles were examined (Figure 52). XRD diffractograms indicate that there is no explicit change in the diffraction peaks in the XRD patterns in series (a) and (b). This result suggests that using octanoic acid instead of propionic acid does not critically change the content of the crystallographic phases in the as-prepared samples. When the total precursor concentration is increased from 0.1 to 0.15 M in series (b) and (c), the diffraction signals specific to La-related oxides disappear in series (c) as well as in series (d) and (e). This result indicates that heating the precursor solution during the synthesis and selecting the metal concentration at 0.15 M is beneficial in preventing the formation of La oxide phases. Furthermore, the increase in the volumetric flow of the premixed CH₄ and O₂ gases in series (c–e) leads to a slight shift of the diffraction peaks towards higher diffraction angles and this shift can be partly related to increasing content of stoichiometric perovskite phase in the as-prepared samples. Also, the observed shift can be due to increasing particle size of the as-prepared nanoparticles synthesized at higher volume flow of CH₄/O₂ which can be confirmed by evolution of shaper diffraction peaks from series (c) to (e).

Among the analyzed samples, the 40 at.% Fe-substituted nanoparticles corresponding to series (e) was selected for further physical characterization as it most likely contains the more stoichiometric perovskite phase. Additionally, 20 and 30 at.% Fe-substituted nanoparticles were also synthesized. The process and solvent parameters used for the synthesis of these nanoparticles are tabulated in Table 10.

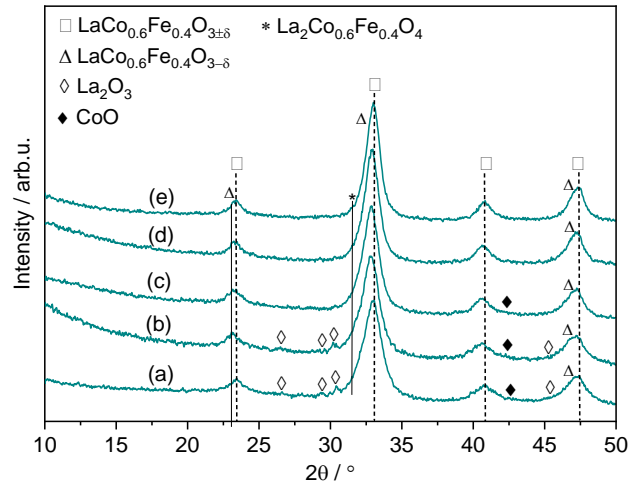


Figure 52: XRD pattern of 40 at.% Fe-substituted perovskites synthesized at the different process and solvent parameters. For the process and solution parameters, see Table 10.

Table 10: Summary of the spray-flame process parameters and the solutions used.

Process and solution parameters	$x_{\text{Fe}}, \text{LaCo}_{1-x}\text{Fe}_x\text{O}_3$		
	0.2	0.3	0.4
CH ₄ /O ₂ pilot flame / (slm/slm)	2/4		
Dispersion gas O ₂ / slm	5		
Solution flow rate / (ml/min)	3		
Pressure / mbar	950		
Sheath gas (compressed air) / slm	125		
Quench gas (compressed air) / slm	170		
Precursors	La, Co, Fe acetates		
Solvent Mixtures (vol.%)	Octanoic acid : 1-propanol : DI water (2:3:1)		
La and (Fe + Co) concentration / M	0.15		

5.3.1 As-prepared $\text{LaCo}_{1-x}\text{Fe}_x\text{O}_3$ perovskites

5.3.1.1 Comparative phase and chemical structure analyses

The XRD patterns of all materials were measured to investigate the crystalline phases present in the as-prepared and heat-treated samples (Figure 53). The comparison of the XRD patterns of the material with 20 at.% of iron with the reference perovskite phase of $\text{LaCo}_{0.8}\text{Fe}_{0.2}\text{O}_3$ (ICSD no: 190099) suggests that the main peaks can be attributed to those of perovskites. At 30 and 40 at.% Fe, the diffraction peaks shift to lower 2θ values, which agrees with previous reports suggesting increasing lattice parameters with increasing Fe content.¹⁰²

In addition, secondary phases of oxygen-deficient $\text{LaCoO}_{2.94}$ (ICSD no: 153995) and lanthanum rich La_2CoO_4 (Ruddlesden Popper-type (RP-type), ICSD no: 16404) were found for all samples. Also, a small content of CoO (ICSD: 9865) is detectable at 20 at.% Fe. Note, the ICSD database only includes

unsubstituted states of these secondary phases. However, slightly shifting peaks at $\sim 23^\circ$, 32.6° , and 47° with increasing Fe content suggest that the secondary phases also contain Fe. We attribute the change in the relative intensity of the peaks at $2\theta \approx 24^\circ$ to a decrease of the amount of secondary RP-type phases at higher Fe content. On the other hand, the relative intensities of the peaks at $2\theta \approx 47^\circ$ imply that the oxygen-deficient perovskite phase content rises with increasing Fe content. Overall, we consider that Fe substitution leads to changes in the secondary phase contents of as-prepared samples.

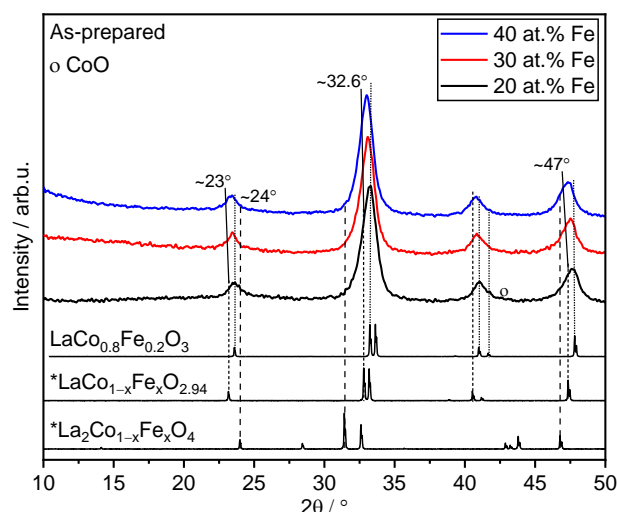


Figure 53: X-ray diffractograms of both the as-prepared samples at increasing Fe contents. Note that although only $\text{LaCoO}_{2.94}$ and La_2CoO_4 were available in the ICSD database as reference, the elemental composition analyses by EDX suggest all samples include Fe (see text). Thus, the reference phases were modified to $\text{LaCo}_{1-x}\text{Fe}_x\text{O}_{2.94}$ and $\text{La}_2\text{Co}_{1-x}\text{Fe}_x\text{O}_4$, respectively.

Using organic precursors and solvents for the synthesis of oxides in a spray-flame reactor is often accompanied by organic residuals from ligands and solvents. They adsorb on the as-prepared catalyst surface, which can thus alter their intrinsic catalytic activities. In this regard, residual surface species in the as-prepared samples were investigated using infrared spectroscopy.

The ATR-FTIR spectra of the as-prepared samples are shown in Figure 54. The spectra of these materials clearly display the main absorbance bands of organic and hydroxyl groups: C–H (2957 , 2922 , 2871 , 2852 , 1434 , 1411 , 1380 , 1303 , 1170 , 722 cm^{-1}), O–C=O (1543 cm^{-1}) and C–O (1111 cm^{-1}).⁸² We assume that the large number of hydrocarbon-based functional groups originate from adsorbed propene species on oxide surfaces. Thus, the observed C–H species can be mostly attributed to the solvents used for these syntheses.^{105,107} The presence of O–C=O and C–O groups at 1543 and 1111 cm^{-1} can be attributed to carboxylate species. The high intensity of C–H group signals can be additionally related to unburnt hydrocarbons. The highly hygroscopic nature of the as-prepared samples is also apparent with the absorption band of O–H groups at $3650\text{--}3080\text{ cm}^{-1}$, which can be attributed to structural water.¹³¹ Besides that, the absorption band intensity of O–C=O and C–H groups were found to vary at different Fe contents, being noticeably lower at decreasing Fe contents relative the band intensity of Co(Fe)–O around 590 cm^{-1} .

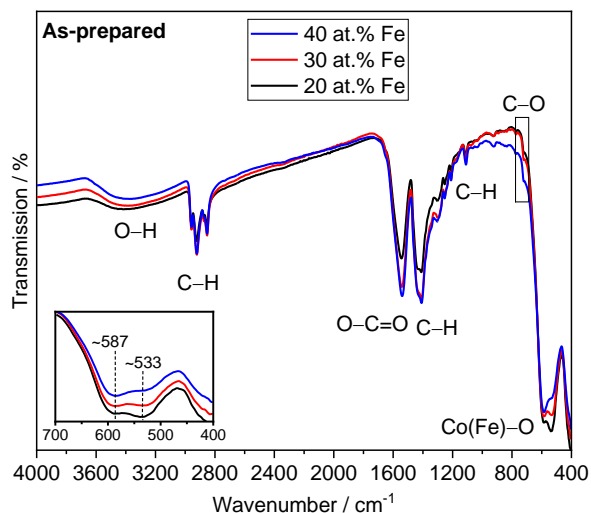


Figure 54: ATR-FTIR spectra of as-prepared nanoparticles. Functional groups were identified and are indicated respectively. The inset shows a zoom of the signals indicating the absorption band of Co(Fe)-O bonds.

A detailed evaluation of the ATR-FTIR spectra in the low wavenumber range shows some differences and changes with respect to the materials' composition. The signals between 400 and 750 cm^{-1} are related to absorptions of cobalt and iron bulk sites. In the spectra of the as-prepared samples, the bands at 587 cm^{-1} can be attributed to octahedral coordination of Co/Fe ions, which is in accordance with the typical absorption band in rhombohedral LaCoO_3 perovskites.¹²⁶⁻¹²⁸ Also, a second band at 533 cm^{-1} appears for all Fe contents and this second band is most likely attributed to a lower symmetry band of the rhombohedral LaCoO_3 structure.¹²⁹ Noticeably, at higher Fe content the band intensity at 533 cm^{-1} decreases relative to the signal at 587 cm^{-1} . This observation indicates that $\text{LaCo}_{1-x}\text{Fe}_x\text{O}_3$ perovskite with more Fe ions leads to an increase in octahedral coordinated Co/Fe ions at higher Fe content.

Overall, ATR-FTIR analyses most importantly points out the presence of high amounts of O-C=O and C-H groups at all Fe contents. This finding implies that catalytic properties of perovskites can be largely influenced by these residual groups. Thus, to get rid of them, the as-prepared samples were heated for five hours in oxygen atmosphere at 250°C, and the physical properties of the heat-treated samples were investigated.

5.3.2 Heat-treated $\text{LaCo}_{1-x}\text{Fe}_x\text{O}_3$ perovskites

5.3.2.1 Comparative phase and chemical structure analyses

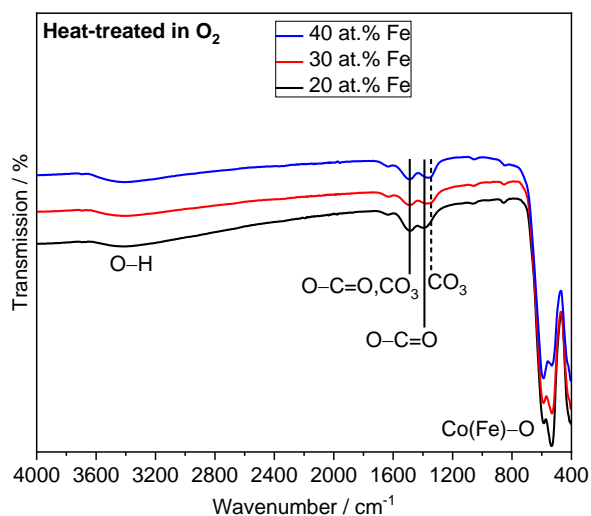


Figure 55: ATR-FTIR spectra heat-treated nanoparticles. Together with Co(Fe)-O bands, water, carboxylate and carbonate functional groups were identified and are indicated respectively.

After heat treatment of the as-prepared samples, the absorption signals of organic species and structural water are largely reduced, meaning that they decompose/desorb with heating (Figure 55). Noticeably, the absorption bands at 1391 and 1487 cm^{-1} appear at all Fe contents, which can be mostly likely attributed to O-C=O groups in carboxylates.¹⁴⁵ With increasing Fe substitutions, O-C=O groups are still present but with shifted band positions (compared to the pristine materials), and an additional functional group at $\sim 1340\text{ cm}^{-1}$ is visible at 30 and 40 at.% Fe. In fact, the band positions at 1490 and $1340\text{--}1350\text{ cm}^{-1}$ can be attributed to the asymmetric and symmetric stretching of the O-C-O group in carbonates. Also, the band splitting of about $140\text{--}150\text{ cm}^{-1}$ (at $\sim 1490\text{--}1345\text{ cm}^{-1}$) for samples with 30 and 40 at.% Fe suggests the configuration of monodentate carbonate species.¹⁴⁶

Overall, the FT-IR spectra of the heat-treated samples clearly indicate the presence of CO_3^{2-} and O-C=O groups as residual functional groups in addition to the metal oxygen bands. Thus, infrared spectral analyses on organic residuals draw attention to the need for controlled low-temperature heating to lower the amount of combustion residuals. Concerning the FT-IR bands of Co(Fe)-O it is observed that heating makes the observed bands (at ~ 587 and $\sim 533\text{ cm}^{-1}$) sharper due to increasing crystallinity of heat-treated nanoparticles, and all spectra of heat-treated materials indicate higher band intensity of octahedral coordination of Co(Fe)-O at increasing Fe contents.

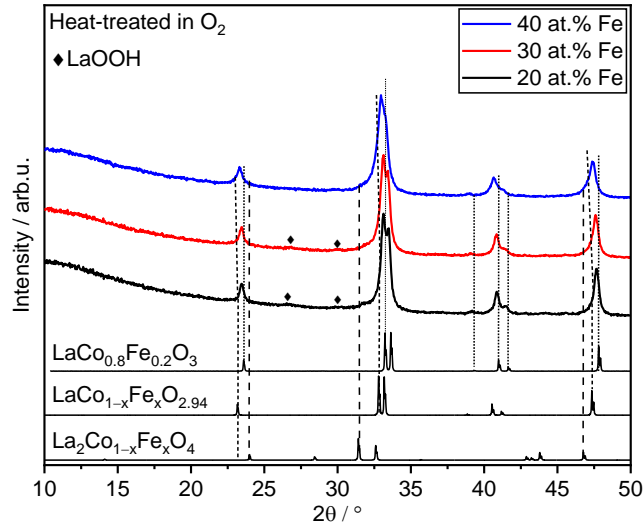


Figure 56: X-ray diffractograms of the heat-treated samples at increasing Fe contents. In addition to stoichiometric and other perovskite-like phases, diffraction peak of LaOOH newly appears at low and intermediate Fe concentrations.

XRD of the heat-treated samples in oxygen (Figure 56) shows that the amount of perovskite phase increases while the $\text{LaCo}_{1-x}\text{Fe}_x\text{O}_{3-\delta}$ phase content reduces, implying an oxidation of the oxygen-deficient $\text{LaCo}_{1-x}\text{Fe}_x\text{O}_{2.94}$ to $\text{LaCo}_{1-x}\text{Fe}_x\text{O}_3$ during heating. Nonetheless, some amount of the oxygen-deficient perovskite is still present, especially at 40 at.% Fe, which can be attributed to incomplete oxidation due to its high content in the as-the prepared sample. Besides that, small diffraction peaks, most probably originated from LaOOH (ICSD: 60675) newly appear at 20 and 30 at.% Fe. These peaks imply a slightly decreasing content of RP-type phases since they oxidize and disproportionate to perovskite and La_2O_3 .

5.3.2.2 Particle characteristics and surface crystal structure

To analyze the successful incorporation of iron atoms into the lattice, the interplanar spacings (d-spacings) of all heat-treated perovskites were investigated using electron diffraction. Therefore, radial profile plots were obtained from the electron diffraction patterns and the position of the main diffraction peak was compared for the different samples (Figure 57).

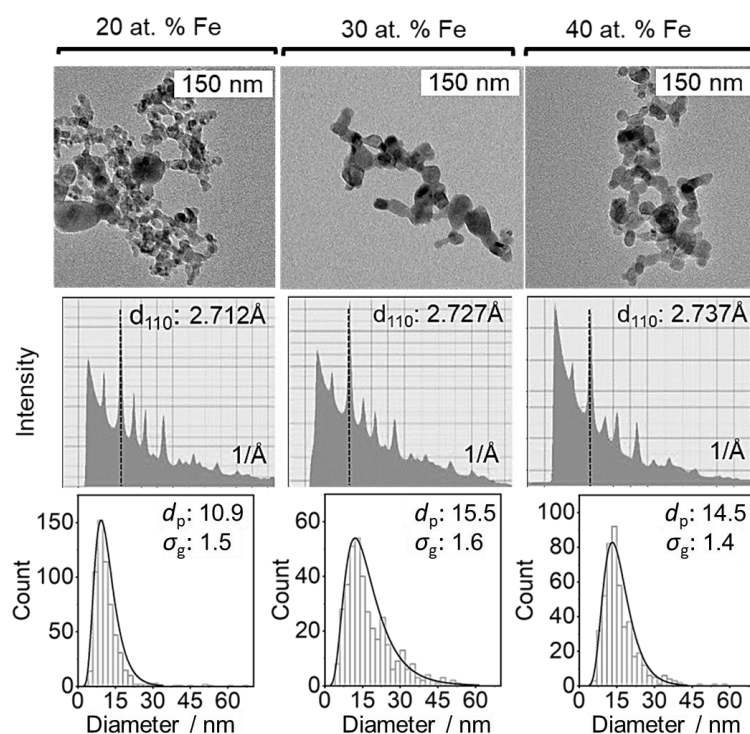


Figure 57: Radial profile plots (middle) obtained from selected area electron diffraction patterns (SAED) together with the particles size distribution shown by both, the low-magnification TEM images (top) and lognormal-fitted curves (bottom). The distribution curves are given with their corresponding mean particle size (d_p in nm) and geometric standard deviation (σ_g) at respective Fe substitutions.

The radial profile plots show that the interplanar spacing value for d_{110} shifts with increasing nominal iron content from 2.7124 (20 at.% Fe) to 2.7367 (40 at.% Fe), indicating an increasing substitution of cobalt with iron. This result is expected and in accordance with the XRD data as well as with the literature data for lattice parameters of Fe-substituted LaCoO_3 perovskites.¹⁰¹ In addition, histograms of the particle sizes were determined from TEM images measuring the size of over 400 nanoparticles/sample (Figure 57, bottom) and fitted to a lognormal particle size distribution. The calculated count median diameters d_p range from 11 to 16 nm, showing the lowest particle size at 20 at.% Fe. The values for the geometric standard deviation σ_g vary between 1.4 and 1.6 as expected for a self-preserving particle size distribution which is typically observed for particles from gas-phase synthesis.¹⁰³

Moreover, EDX measurements (Table A1) on single particles using dark-field STEM were made out of over 15 selected crystallites per sample. The results show that the measured atomic ratios of Fe/(Fe+Co) are consistent with the concentration ratios adjusted in the precursor solutions, confirming both, an overall homogeneous incorporation of iron and a preservation of the intended atomic ratio between Fe and Co. However, the measured average La content showed about 10 at.% excess in case of 20 at.% Fe and about 20 at.% excess in case of 30 and 40 at.% Fe, indicating a La-rich composition. This result can be attributed to the presence of Ruddlesden-Popper phases. More precisely: As Fe was found in all EDX measurements and La_2CoO_4 was detected in the XRD measurements, the La-rich composition can be most likely related to $\text{La}_2\text{Co}_{1-x}\text{Fe}_x\text{O}_4$ -like phases, being present in minor content in the heat-treated samples. For a more detailed structural analysis, the surface structures of selected representative nanocrystals were investigated using HAADF-STEM (Figure 58 and Figure 59).

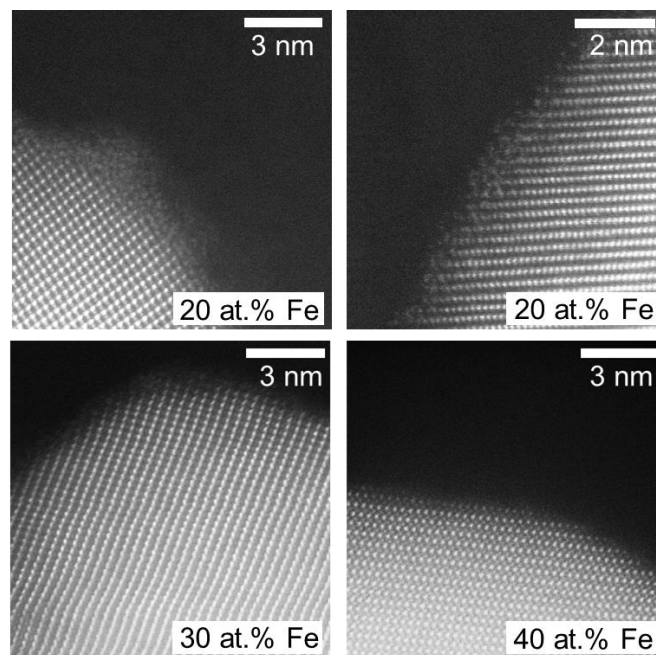


Figure 58: HAADF-STEM images showing the atomic arrangements of the bulk and the surface region (heat-treated samples). The white rectangles in the insets indicate the near-surface regions where the atomic structure of perovskites with different Fe content were analyzed. The white solid arrows (right) highlight the nanoscale ordering of a crystallite with 40 at.% Fe.

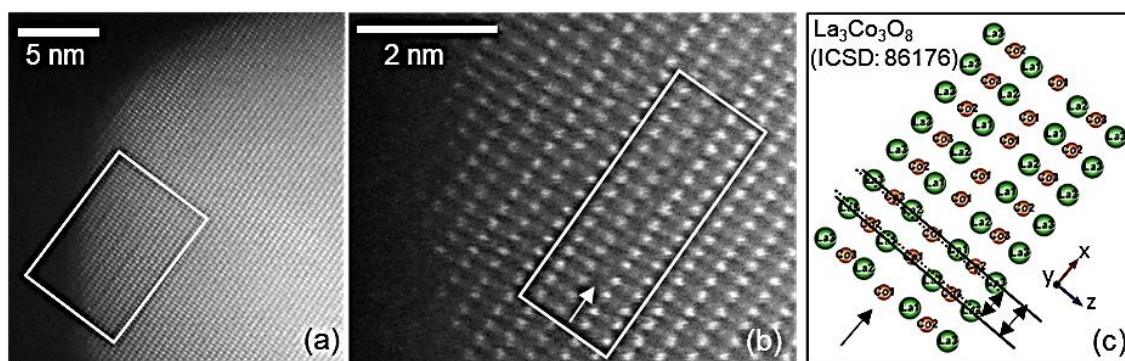


Figure 59: HAADF-STEM image of the 30 at.% Fe-substituted sample showing the dark stripes near the surface structure of the selected crystal (indicated within the rectangle in (a)), the shorter distances between Co atoms in the one dark stripe on the plane indicated by the white arrow (b). Simulated crystal structure of oxygen vacancy ordered structure indicating the shorter distances between Co atoms in the planes (see the two-sided arrows) on the plane indicated by the black arrow, which is projected along $\langle 010 \rangle$ direction in (c).

At the lowest iron content (20 at.%), the selected crystallite surface appears to be rich in defects, which is distinct from the bulk structure (cf. XRD in Figure 56). The 30 at.% Fe-substituted particles usually show a less defective surface structure and a highly crystalline bulk structure. Together with that, the formation of dark stripes at the some crystallites were also observed at this composition and the one of them was indicated in Figure 59a. Previous reports on LaCoO_3 perovskite suggest that these dark stripes can be originated from the oxygen vacancies orderings.^{20,138} Indeed, the magnified STEM images focusing on one of the observed dark stripes indicate the shorter distances of the Co ions at particular atomic planes (Figure 59b), and this structural feature can be matched with those of oxygen vacancy ordered

$\text{La}_3\text{Co}_3\text{O}_8$ Brownmillerite (Figure 59c). It is important to note that the crystal analyzed in Figure 59 is not pristine, and contain about 30 at.% Fe and 30 at.% excess La as found by the EDX analyses. Thus, its overall composition can be denoted as $\text{La}_4\text{Co}_{2.1}\text{Fe}_{0.9}\text{O}_{10-\delta}$ being similar to those of RP-type phases. At 40 at.% Fe, a very high crystallinity was observed with almost no surface defects. Compared to the two other materials, a varying contrast was observed (indicated by white solid arrows) suggesting the formation of layers in which the bright regions are most likely related to La-rich compositions owing to their high atomic weight (Figure A5). Such type of atomic arrangement at high Fe contents was reported previously for Co- and Fe-based double-perovskite structures, and therefore draws attention to nanoscale ordering in perovskite structures with higher Fe substitution.^{147,148}

5.3.2.3 *Magnetic properties and Fe oxidation state analyses*

To relate the observed compositional and structural findings with the magnetic properties of the samples magnetometry measurements were also carried out, and their results were shown in Figure A6. Magnetization curves under the applied magnetic field at 4.3 K (Figure A6a) display weak hysteresis loops with no saturation magnetization, which suggest presence of antiferromagnetic (AFM) interactions in Fe-substituted perovskites. Noticeably, extent of magnetization at 4.3 K show a systematic decrease with increasing Fe contents, which can be related to increasing antiferromagnetic interactions at higher Fe substitutions. Besides that, temperature-dependent field-cooled and zero-field-cooled magnetization curves (Figure A6b) display a certain extent of splitting, which suggest that some fraction of the samples have net magnetic moment at higher ordering temperatures. Overall, the magnetometry analyses clarify the concentration of Fe substitutes in perovskite are directly related to AFM interactions, but the influence of nanoscale ordering of perovskite structure on such AFM interactions cannot be excluded, especially at 40 at.% Fe substitutions.

To investigate magnetic fingerprints of the perovskite phases and to examine the local environment and oxidation state of the Fe ion, low-temperature Mößbauer spectra were measured. The spectra recorded at 4.3 K are shown in Figure 60. The measurement of the as-prepared sample with the lowest iron content has a poor signal-to-noise ratio and is therefore not shown.

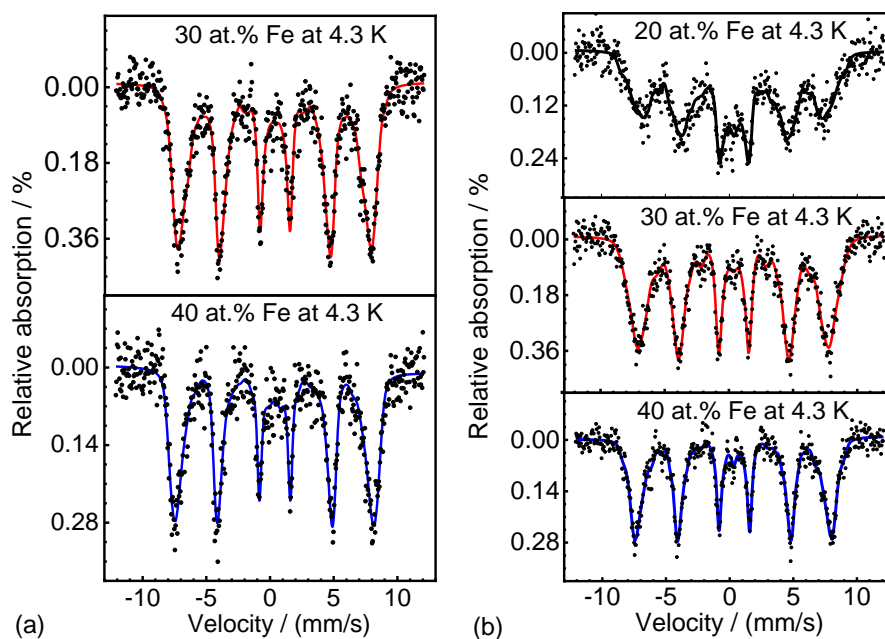


Figure 60: Mößbauer spectra of as-prepared (a) and heat-treated (b) $\text{LaCo}_{1-x}\text{Fe}_x\text{O}_{3\pm\delta}$ measured at 4.3 K.

All Mößbauer spectra show only one sextet hyperfine structure regardless of their Fe content and the spectra of the samples with 30 and 40 at.% of Fe are very similar. However, the peak widths of the sextets slightly narrow with increasing iron content indicating a higher degree of magnetic ordering. Together with that, higher magnetic-ordering temperatures ($T_{\text{Néel}}$) at higher Fe substitutions can also explain the narrower peak width.

To quantify the observed trends in the Mößbauer spectra, the hyperfine parameters were analyzed by fitting the measured sextets with Fe-Mößbauer literature data (Table A3). The isomer shifts (0.33–0.36 mm/s) and the quadrupole level shifts (between -0.10 and -0.04) are in very good agreement with those of perovskite structures reported previously, suggesting Fe^{3+} ions in octahedral coordination.¹⁴⁹ The magnetic hyperfine field increases with increasing Fe substitution. This can be attributed to a decreasing number of neighboring Co ions as proposed by Kondakindi et al.¹⁴⁹ Most importantly, the analyzed Mößbauer spectra do not show any detectable differences in terms of oxidation state of Fe but are mainly affected by the local coordination of Fe with neighboring Co atoms.

5.3.2.4 Surface chemistry and oxidation state of constituent elements

Previous reports emphasize the decisive role of surface composition and oxidation states of transition-metal ions on the OER catalytic activities of catalyst nanoparticles.^{33,34} Therefore, surface properties of the heat-treated nanoparticles were investigated with XPS. Surface elements and their oxidation states (heat-treated samples) were analyzed using Mg- K_α scanned XPS regional spectra ($h\nu = 1253.6$ eV).

Figure 61a shows the core-level and satellite features of Fe2p for all three samples. In all spectra, the satellites are observed between 720–716 eV. These satellites can be attributed to those of Fe^{3+} ions which are typically observed at ~ 718 eV in perovskite materials.¹⁵⁰ The core-level signals of Fe2p $_{3/2}$ also mostly show a good match with the peak profile of Fe^{3+} ions. At about 708.4 eV, a weak shoulder is visible at all Fe contents, which is a hint towards the presence of little amounts of Fe^{2+} ions.

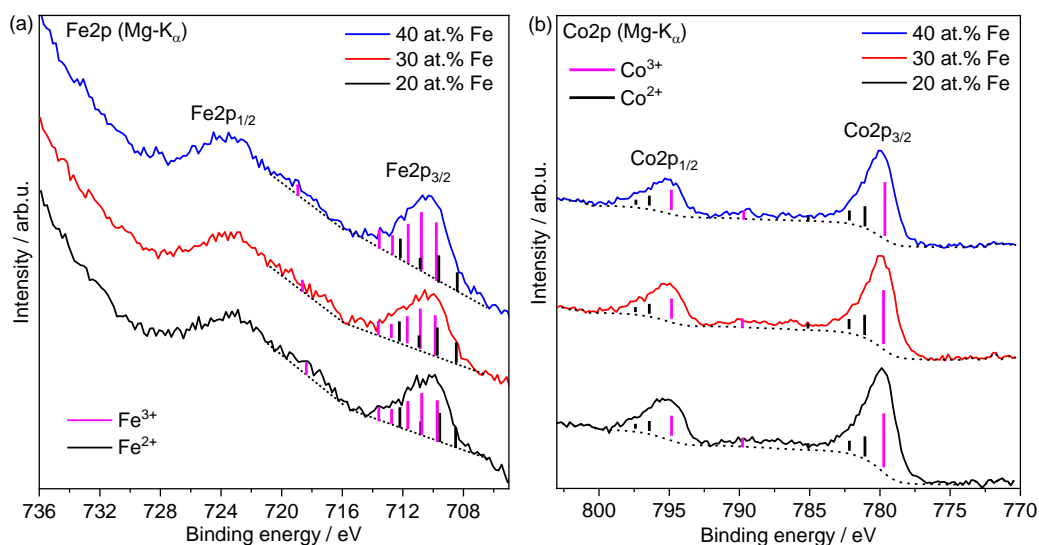


Figure 61: Regional XPS spectra of Fe2p and Co2p using XPS (source: Mg-K α). Reference lines of Fe and Co oxidation states were drawn referring to a previous study.¹¹⁵

Figure 61b demonstrates the Co2p core-level binding energies in the Co2p spectra. They were found at 779.9 and 795.1 eVs and have the spin-orbital splitting of 15.2 eV. Both of these findings mostly correspond to the Co2p spectra of stoichiometric LaCoO₃ perovskites, meaning that Co³⁺ ions are predominantly present.¹⁵¹ Low XPS signals of Co²⁺ ions are also found at ~781.1 and 782.1 eVs in the analyses of Co2p_{3/2}. Other than the core-level spectra, the Co2p satellites are observed between 792–785 eVs and show no explicit signals of Co³⁺ and/or Co²⁺ ions at different Fe content. Such satellite features were observed in reduced LaCoO₃¹⁵¹ and other Co-based compounds,¹⁵² indicating the presence of mixed oxidation state of Co^{3+/2+} surface ions.

Overall, the combined interpretation of Fe2p and Co2p spectra reveals that most of the transition metal surface ions consist of Co³⁺ and Fe³⁺. Thus, the surface composition of the heat-treated nanoparticles can be attributed to LaCo_{1-x}Fe_xO_{3±δ} perovskites. On the other hand, a small amount of Co²⁺ and Fe²⁺ ions was identified which can be related to oxygen-deficient LaCo_{1-x}Fe_xO_{3-δ} perovskites and/or La₂Co_{1-x}Fe_xO₄. Both of these perovskite-like compounds can stabilize the Co²⁺ and Fe²⁺ ions in their structure.

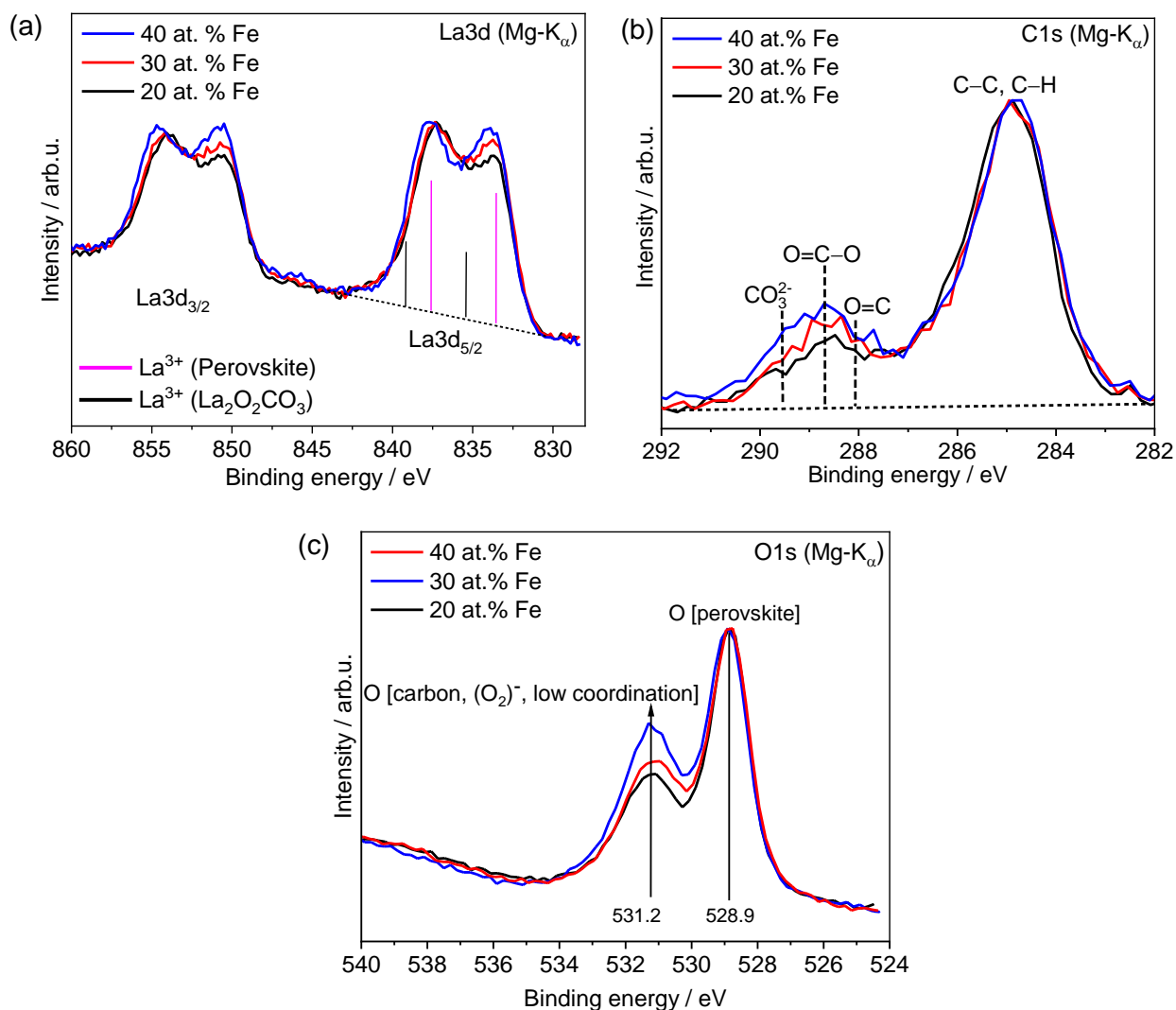


Figure 62: Mg- K_{α} XP spectra of La (a), C (b), and O (c) signals (heat-treated $\text{LaCo}_{1-x}\text{Fe}_x\text{O}_{3\pm\delta}$ perovskites). Reference lines of La3d were taken from. ¹¹³

In addition to the findings of the Fe2p and Co2p XPS spectra, the La3d core-level spectra show some considerable differences at varying Fe content (Figure 62a). They indicate a spin-orbit splitting of 16.8 eV between La3d_{3/2} (850.5 eV) and La3d_{5/2} (833.7 eV), which is a typical value for La³⁺ ions in perovskite structures.¹¹¹ With increasing Fe content, the satellite La3d signals shift towards higher binding energies and the intensity of the core-level signals increases relative to the satellite signals. These changes might originate from LaOOH identified in the XRD analyses. Kumar et al. observed in the La₂O₃ compounds that La3d satellite peaks become more intense when the La compounds were exposed to water.¹¹⁴ Hence, higher relative satellite signal intensities might be related to the increasing amount of LaOOH at decreasing Fe content as also observed for the XRD data of heat-treated materials with 30 and 20 at.% of iron.

In addition to that, there can be an influence of the CO₃²⁻ ions on the core-level signals of La3d spectra. Therefore, the C1s spectra were also investigated (Figure 62b). An increasing signal intensity for C=O, O=C-O and CO₃²⁻ was observed with increasing Fe content. The carbonate signal can be related to La compounds as the multiplet splitting of ~3.6 eV between the La3d core-level and satellites is in agreement with those of La₂O₂CO₃.¹¹³ The increasing intensity of CO₃²⁻ related C1s signals at higher Fe

content is also in accordance with the increasing signal intensities of CO_3^{2-} groups in the ATR-FTIR spectra (see Figure 55). Overall, the La3d core-level and satellite spectra can be related to the perovskite structure while specific spectral changes in the core-level spectra are likely due to the presence of LaOOH and $\text{La}_2\text{O}_2\text{CO}_3$.¹¹³

Table 11: Relative content of oxygen signals associated with carbon, superoxide, and low-coordination species as well as perovskite compounds.

	20 at.% Fe	30 at.% Fe	40 at.% Fe
O (carbon)	24.6	21.7	24.8
O (O_2^-, low-coordination)	15.5	20.7	24.1
O (perovskite)	59	57.6	51

The O1s spectra show the main oxygen signals at 528.9 eV, which can be attributed to the characteristic oxygen signal of stoichiometric perovskites (Figure 62c).¹¹⁹ The second oxygen signal at ~531.2 eV has a lower intensity and shows an increase with higher Fe content. This signal is usually attributed to hydroxyl oxygens, carbon-bonded oxygen, $(\text{O}_2)^-$, and low-coordinated oxygen species.¹⁴⁰ However, the abovementioned FT-IR analyses show that no explicit hydroxyl bands are present in heat-treated samples, suggesting ignorable effect of hydroxyl oxygen in O1s spectra. In addition to that, Table 11 indicates a similar content of carbon-bonded oxygen, being at 22–25 at.%. These findings do not clarify the increasing oxygen signal at 531.2 eV either. Therefore, increasing O1s signal at 531.2 eV can be more likely attributed to increasing content of $(\text{O}_2)^-$, and/or low-coordinated oxygen species. A previous report states that the coordination numbers of transition metal and oxygen reduce upon an increase in the oxygen vacancy concentration in Fe-based perovskite.¹⁵³ Referring to that, the amount of low-coordinated oxygen species with increasing Fe content can be likely related to those of sub-stoichiometric perovskite phases, $\text{LaCo}_{1-x}\text{Fe}_x\text{O}_{2.94}$, identified by XRD. Details of surface characteristics of heat-treated samples will be further discussed below.

5.3.3 Comparison of the OER activity of as-prepared and heated perovskites

Following the physical characterization analyses, OER catalytic activity of the as-prepared and heat-treated nanoparticles was investigated using a 3-electrode electrochemical cell in 1 M KOH (Figure 63). The potential required to attain a current density of 10 mA/cm² was used as parameter to compare the OER activity of the different samples, and the activity trends are shown in Figure 64. Surprisingly, two opposite trends are observed for the as-prepared and heat-treated samples concerning their OER activities. For the as-prepared samples, a minor decrease in OER activity is observed with increasing iron content (Figure 63a) while the OER activities of the heat-treated nanoparticles increases with the iron content (Figure 63b). Similar trends are observed, when the electrochemical surface area (ECSA) is used to normalize the current density (Figure 63c,d). However, these trends are more pronounced for the 20 at.% Fe while no significant difference is observed for the samples with higher iron content. A similar behavior was found when evaluating the stability of $\text{LaCo}_{1-x}\text{Fe}_x\text{O}_3$. Chronopotentiometric measurements applying a current density of 10 mA cm⁻² show an improved stability for the 20 at.% Fe as-prepared sample (Figure A7a) while the 20 at.% Fe heat-treated samples show a significantly lower stability (Figure A7b). The decreasing OER activity of the as-prepared samples at higher iron contents can be explained in several ways: Firstly, the abovementioned chemical structure analyses (Figure 54) revealed

that these samples contain an increasing amount of organic residuals with increasing iron content. This increase in organic residuals most likely blocks electrocatalytically active sites at the perovskite surface and may lead to decreasing OER potentials with increasing Fe content.

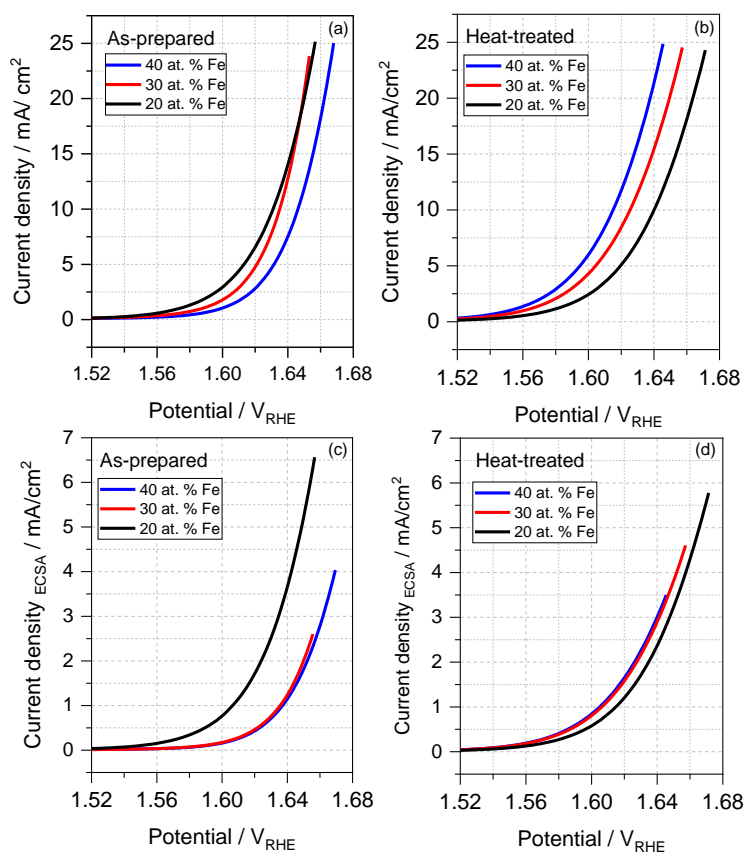


Figure 63: Linear sweep voltammograms (iR compensated) of $\text{LaCo}_{1-x}\text{Fe}_x\text{O}_3$ perovskites recorded in 1 M KOH at a scan rate of 5 mV/s and 1600 rpm electrode rotation. The graphs show the OER activities of the as-prepared and heat-treated perovskite nanoparticles normalized by the geometric area (a, b) and by the electrochemical surface area (c, d).

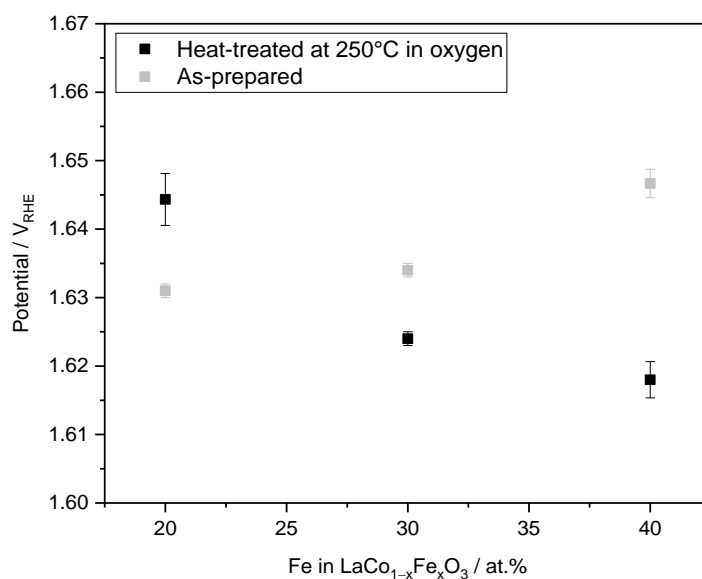


Figure 64: OER activities of $\text{LaCo}_{1-x}\text{Fe}_x\text{O}_3$ perovskites expressed as the potential at a current density of 10 mA/cm^2 . Three samples were considered and three different measurements were made for each sample. The error bars indicate the standard deviation.

Besides the organics residuals, high amounts of sub-stoichiometric perovskite compounds in the as-prepared samples also might affect the OER activity. In a previous study, it was shown that high amounts of oxygen deficiency in Co-based perovskite structures significantly decreases their electronic conductivity.¹⁵⁴ As our findings of the qualitative phase analyses indicate an increasing amount of oxygen-deficient perovskite at higher Fe content, it is highly likely that the electronic conductivity of the as-prepared samples is reduced with increasing Fe content. Together, the high content of combustion residuals, and oxygen-deficient perovskite phases at high Fe contents could explain both, the low OER activities of as-prepared samples (compared to the heat-treated ones), and their decreasing catalytic activity with increasing Fe content.

The observed increase in the OER activity of the heat-treated samples can be attributed to several factors. At first, as shown in chemical structure and phase analyses, heat-treated samples contain much less combustion residuals and oxygen-deficient perovskite phases. Therefore, their catalytic active sites may likely be much more available than the as-prepared ones. Also, as deduced from sharper infrared Co/Fe–O infrared bands, heat-treated samples show a higher crystallinity which can increase their local electronic conductivity. These findings can explain the higher activities of heat-treated samples with 30 and 40 at.% Fe also compared to as-prepared ones. On the other hand, a reduced OER activity is observed for the samples with 20 at.% Fe, also in comparison with the some of as-prepared samples. We attribute this to the fact that (i) small amounts of CoO or La_2CoO_4 are found in the as-prepared samples, which might improve their overall OER activity and (ii) the heat-treated sample shows a defect-rich surface (Figure 58).

Increasing OER activity of heat-treated samples at 30 and 40 at.% Fe can be also associated with the abovementioned physical characterization results in a variety of ways. First, the bulk properties of the catalysts are discussed. Mößbauer and infrared spectral analyses point out that octahedral coordination of Fe^{3+} ions is present in all samples and the extent of octahedral coordinated Co^{3+} and Fe^{3+} ions increases with increasing Fe content. Such an increase in the octahedral coordinated transition metal ions does not

only stabilize stoichiometric $\text{LaCo}_{1-x}\text{Fe}_x\text{O}_3$ but also oxygen-deficient $\text{LaCo}_{1-x}\text{Fe}_x\text{O}_{3-\delta}$, which is obvious from XRD. Indeed, a positive effect of Fe incorporation on the structural stability of LaCoO_3 was also stated in a previous study.¹⁵⁵ Yet, the findings on increasing amount of sub-stoichiometric oxygen in perovskite at high Fe suggests that ordered perovskite crystal observed in several crystals can be more likely due to ordering of oxygen vacancies. It is necessary to note that oxygen vacancy ordering could be related not only to oxygen-deficient perovskites but also to RP-type structures since the elemental composition analyses indicates an excess of La at high Fe contents. Overall, the results concerning the bulk characteristics indicate a positive influence of Fe incorporation on secondary phase stability and formation of oxygen-deficient perovskites.

The surface-sensitive spectroscopic analyses also show good agreement with bulk characterization results. They indicate that the particle surface contains an increasing amount of carbonate at higher Fe contents, which is also supported by infrared spectroscopy. Together with the formation of LaOOH shown by XRD, we attribute the spectral changes in La XPS measurements to an increase in carbonate with increasing Fe content. Besides that, XPS of surface oxygen species indicates an increasing number of low-coordinated oxygen with increasing Fe content, which could be associated found to be associated with an increasing covalence of the Co(Fe)-O bond.¹⁵⁶ Such an influence of Fe incorporation on the covalence of Co-O bond was also discussed for LaCoO_3 perovskites.¹⁵⁷ These findings can explain the increase of low-coordinated oxygen species with increasing Fe content. Together with that, an increasing content of oxygen vacancies, observed in the perovskite with higher Fe contents, may also lead to more vacant oxygen sites at the perovskite surface, and explain the increase in the low-coordination oxygen species.¹⁵³

Overall, the most active catalyst shows a high content of sub-stoichiometric oxygen species in its bulk structure. In addition, the surface of this catalyst contains a high number of low-coordinated oxygen species. In agreement with previous findings,¹⁵⁸ both of these characteristics can be associated with the improved OER activity of heat-treated nanoparticles with the highest Fe content.

6 Outlook

In this thesis, the spray-flame synthesis $\text{LaCo}_{1-x}\text{Fe}_x\text{O}_3$ perovskite nanoparticles, their bulk/surface characteristics, and their electrocatalytic properties for OER reactions are presented in a systematic fashion. The major challenge in the synthesis of this perovskite system was found as the suppression of the formation of secondary perovskite-like and/or single oxide nanoparticles as their presence does not allow to identify the individual effect of Fe substitution on the chemical, structural, and morphological properties of LaCoO_3 . Although the last two chapters in this thesis discuss the optimization of process parameters and precursor solution characteristics to suppress the formation of single oxide phases, other perovskite-like phases, namely Ruddlesden-Popper type and Brownmillerite compounds are still present at low amounts in all of the pristine and Fe-substituted LaCoO_3 materials. To solve this issue, several approaches should be investigated.

The formation of La-rich layered perovskites; namely Ruddlesden-Popper type phases, can be caused by the differences in the thermal decomposition temperature of La, Co, and Fe acetates and/or the precursor complexes formed within the solution. The formation of CoO , Fe_2O_3 , and La_2O_3 from acetate precursors was reported to start at about 350, 300, and 875°C ^{159,160}, respectively. Much higher thermal decomposition temperatures of the La acetates imply that gas-to-particle conversion from La acetate precursors are less likely than for Co and Fe acetates. This can explain why La-rich compositions are observed in several large particles (formed through droplet-to-particle conversion) while Co-rich compositions are found in some nanoparticle down 4 nm (formed through gas-to-particle conversion). This problem could be reduced by researching spray-flame synthesis of solely La oxide nanoparticles from different La precursor compounds and determining the most volatile low-cost precursor. Also, as shown for spray-flame made La_2O_3 from La ethylhexanoates in a previous report⁷⁸, the dispersion-gas flow could be further increased to trigger finer spray, hence faster evaporation and thus a larger fraction of gas-to-particle conversion of La acetates to La_2O_3 as intermediate oxide *en route* the formation of $\text{LaCo}_{1-x}\text{Fe}_x\text{O}_3$ perovskite formation. Besides, it is likely that CoO and Fe_2O_3 intermediates could be more volatile than the respective LaO_x intermediates due to their lower atomic masses. Therefore, they might vaporize more rapidly already at lower temperatures in the spray flame leading to the formation of La-rich oxides in the droplets and their vicinity. In order to determine if the loss of intermediate species causes non-stoichiometric chemical compositions in the as-prepared nanoparticles, increasing the concentration of Co and Fe precursors in the solution while keeping the La precursor concentration fixed could be used to compensate their loss. If this is not successful and CoFeO_x nanoparticles form in addition to $\text{LaCo}_{1-x}\text{Fe}_x\text{O}_3$ perovskites in the as-prepared material, such perovskite-oxide system could anyway be used as OER catalysts as it can show even more catalytic activity than only perovskite material system (cf. Figure A8).

The formation of the Brownmillerite phase can be more relevant to the high-temperature oxidation state of La, Co, and Fe. In this thesis, it was shown that La^{3+} and Fe^{3+} ions are present in most of the particles while Co^{2+} and Co^{3+} ions coexist at different ratios depending on the synthesis conditions. From the Co–O phase diagram, it can be deduced that Co^{2+} ions are more stable than Co^{3+} ions at temperatures above 900°C .¹⁶¹ Similarly, a high content of Co^{2+} ions could be stabilized at spray-flame temperatures, which could be confirmed by the phase composition of spray-flame made $\text{La}_2\text{CoO}_4/\text{La}_2\text{Co}_2\text{O}_5$, (cf. Figure A9).

More oxygen-rich $\text{LaCo}_{1-x}\text{Fe}_x\text{O}_3$ perovskites could potentially be generated by increasing the concentration of more capable oxidizers such as OH radicals. Thus, addition of hydrogen in methane was suggested to form higher concentration of OH radicals in combustion and therefore enhancing the oxidation rate of intermediate products.^{162,163} Otherwise, as described in this thesis, low-temperature heat treatment of the as-prepared nanoparticles in O_2 or vacuum is needed to oxidize the oxygen-deficient phase while cleaning the surface of nanoparticles, so that an increase in the catalytically active sites on the nanoparticle surface could be obtained, which leads to higher OER catalytic activities (cf. Table A4).

Overall, completely phase-pure $\text{LaCo}_{1-x}\text{Fe}_x\text{O}_3$ perovskites could be synthesized by spray-flame synthesis provided that the abovementioned conditions are well researched. For material characterization, TEM measurements at STEM mode and XPS measurement are particularly necessary to clarify chemical composition and elemental mapping of individual perovskite crystallite, surface atomic structure while revealing the surface oxidation state and chemistry of the constituent elements.

7 Summary and Conclusions

Environmentally friendly water splitting plays a key role in the development of clean energy technologies. However, large-scale utilization requires low-cost, efficient, and robust electrode materials for the electrochemically most important step, the oxygen evolution reaction (OER). The main challenge of the OER is to increase the kinetics of this four-electron transfer reaction as it suffers from high overpotentials. For this reason, alongside with conventionally used catalysts based on Ru, Ir, and Pt nanoparticles, a great deal of research has been concentrated on perovskite structured compounds to develop noble-metal free highly active and selective catalysts. Owing to their flexible crystal structure, tunable electronic configuration and high chemical versatility, the focus is particularly on transition-metal-based perovskites as they can enable synergetic effects of different oxidation states of transition metals to improve the catalytic oxidation properties. Having sufficiently high electrical conductivity as well as mechanical and chemical stability, this class of compounds are put forward as promising OER catalysts. Among them, transition-metal-based perovskites such as $\text{SrCoO}_{2.7}$, $\text{Ba}_{0.5}\text{Sr}_{0.5}\text{Co}_{0.8}\text{Fe}_{0.2}\text{O}_{3-\delta}$, $\text{SrCo}_{1-x}\text{Fe}_x\text{O}_{2.5}$ are known to be highly active OER catalysts, where the importance of oxygen-vacancy defects and Fe substitution further enhances the activity.¹⁶⁴

The addition of La as A-site cations either as host or substituted ions were found to also increase the catalytic stability of these perovskites against surface amorphization and corrosion under OER conditions.¹⁶⁵ La-based cobalt ferrite perovskites have been identified as both active and stable OER catalysts, and the relationship of their electronic structure with OER activity has been elucidated. The combined analyses of surface and bulk structure/composition of these perovskite still need to be unveiled.¹⁵⁷

Spray-flame synthesis has been successfully applied to produce nanoscale transition-metal-based $\text{La}_{0.6}\text{Sr}_{0.4}\text{Co}_{0.8}\text{Fe}_{0.2}\text{O}_{3-\delta}$ and $\text{Ba}_{0.5}\text{Sr}_{0.5}\text{Co}_{0.8}\text{Fe}_{0.2}\text{O}_{3-\delta}$ perovskites⁵ but systematic research on comparably low-cost, sustainable, and available mixed oxides with perovskite structures, especially La, Fe, and Co in quasi-ternary systems, is rarely reported for spray-flame made nanoparticles. Therefore, the objective of this thesis was to find out the fundamental aspects of the relationship between synthesis conditions and generated material on the one hand and material and its catalytic activity on the other hand for spray-flame-synthesized $\text{LaCo}_{1-x}\text{Fe}_x\text{O}_3$ perovskites to develop synthesis routes for active low-cost OER catalysts.

With the first systematic research on spray-flame syntheses of $\text{LaCo}_{1-x}\text{Fe}_x\text{O}_3$ perovskite using Fe/(Fe+Co) precursor ratios of 0, 20, 40, and 60 at.% while keeping the La/(Co+Fe) ratio constant, the influence of Fe-substitution on the as-prepared nanoparticles could be determined in terms of chemical and phase composition, surface oxidation, and electrocatalytic activity. Energy-dispersive X-ray spectroscopy (EDX) measurements in the scanning transmission electron microscopy mode (STEM) reveal that Co atoms were well substituted by Fe while excess La concentration was found in the chemical composition of as-prepared nanoparticles. Irrespective of the Fe content, qualitative phase analyses by XRD measurements indicate that the as-prepared materials contain multiple phases of perovskite, Ruddlesden–Popper-type, and Brownmillerite phases, as well as minor contents of La and Co single-oxide phases. All Fe-substituted materials could be produced with a similar nanoparticle size-distribution with average diameters of around 6–7 nm, while the LaCoO_3 perovskite synthesis led to average particle sizes

around 14 nm. Complementary analyses by FTIR and XPS revealed the presence of carbonaceous impurities on the catalyst surface. For all catalysts, Co^{2+} and Fe^{3+} ions were predominantly found as surface oxidation states of Co and Fe atoms, while the surface chemistry of La, Co, and O was found to be influenced by secondary Co and La single-oxide phases.

Rotating disk electrode measurements showed that increasing Fe substitution decreased the catalytic activity in the OER, and a 40 mV higher overpotential was additionally required to obtain a current density of 10 mA/cm^2 in case of the 60 at.% Fe material compared to the catalysts with no Fe. A similar trend is observed also in the case of the electrocatalytic EtOH oxidation. Using *operando* electrochemistry/ATR-FTIR spectroscopy, the product acetaldehyde could be detected at potentials lower than 1.78 V vs. RHE for the 60 at.% Fe nanoparticles while just acetate was detected with LaCoO_3 as the catalyst, independent of the applied potential. On the whole, this research showed that the as-prepared spray-flame-made nanoparticles having Fe content lower than 60 at.% could exhibit promising OER and EtOR activities. Following to the initial research on the $\text{LaCo}_{1-x}\text{Fe}_x\text{O}_3$ materials system with Fe/(Fe+Co) precursor ratios of 0, 20, 40, and 60 at.%, the focus is given on spray-flame synthesis process parameters (i.e., the ratio between precursor solution flow rate (PFR) and dispersion O_2 gas) and solvent characteristics such as the volumetric ratio of alcohol to organic acid to find out the best conditions that lead to an increase in the fraction of stoichiometric perovskite in the as-prepared material. By increasing the dispersion gas flow from 4 to 5 slm at 3 ml/min of precursor solution flow rate and using the volume ratio of propionic acid/1-propanol of 40/60, not only the phase content of secondary oxide and perovskite-like phase could be reduced, but also combustion residuals on the particle surface could be considerably reduced.

Heat-treatment of as-prepared particles at increasing heating temperatures (i.e., at 250, 450, and 600°C) in O_2 enabled a further reduction of the content of the remaining secondary phases and diminish carbonaceous impurities while forming carbonate groups. As a result of increasing Fe content at heat-treated particles, higher contents of Brownmillerite phases, magnetically-ordered antiferromagnetic domains, and surface Co^{2+} ions, and octahedrally-coordinated Co/Fe could be detected. Increasing the heating temperature at constant Fe substitution resulted in a phase transformation of the Brownmillerite to perovskite phases and the conversion of surface Co^{2+} ions to Co^{3+} ions while also leading to an increase in the average particle size from ~8 up to ~18 nm; also particle sintering increased. The OER activity tests show that increasing the Fe substitution induces a slightly increasing catalytic activity for the materials heat-treated at 250°C, while increasing the heat-treatment temperature did not have a significant effect on the catalyst activity. In summary, the highest OER activities were found at 60 at.% Fe-substituted nanoparticles heat-treated at 250°C, which is most likely related to the high content of oxygen-deficient phases and surface Co^{2+} ions.

The last part of the thesis focused on synthesizing $\text{LaCo}_{1-x}\text{Fe}_x\text{O}_3$ perovskites with Fe/(Fe+Co) precursor ratios of 20, 30, and 40 at.% in such a way that the phase content of stoichiometric perovskite in the as-prepared nanoparticles could be as much as those of the heat-treated nanoparticle at 450 and 600°C in the previous chapter. By replacing propionic acid with octanoic acid, heating the precursor solution during the spray-flame synthesis and increasing the volume flow of the pilot-flame feed gases, the perovskite phase content could be increased while secondary phases of single-oxide particles could be eliminated from the as-prepared material. Heating the as-prepared nanoparticle only at 250°C in O_2 enabled the oxidative removal of hydrocarbon residuals from the catalyst surface. Electron microscopy

reveals that heat-treated samples have small nanoparticle sizes ranging between 10–15 nm with a defective crystal structure at low Fe content while displaying highly ordered crystal structures at higher Fe concentration. Fe^{3+} and Co^{3+} ions with octahedral coordination were found to be dominant, and increasing octahedral coordination was found in the infrared and Mößbauer analyses. Both bulk and surface analyses of heat-treated perovskites show an increasing content of sub-stoichiometric oxygen content with increasing iron concentration. Surface-sensitive analyses reveal higher content of low-coordinated oxygen species with increasing Fe content, which is assumed to be associated with an increasing covalence of the $\text{Co(Fe)}\text{-O}$ bond and high amount of surface oxygen vacancies. Overall, the most active catalysts were found to have the highest sub-stoichiometric composition and low-coordinate oxygen species.

To summarize, the results in this thesis indicate that $\text{LaCo}_{1-x}\text{Fe}_x\text{O}_3$ perovskite nanoparticles can be produced by spray-flame synthesis in both their multiphase and near-single phase composition. In multiphase system and as-prepared nanoparticles, the most active OER catalyst were found as the LaCoO_3 perovskite and the underlying reason is mainly attributed to the activity of not only perovskite but also cobalt oxide nanoparticles, which form at low or no Fe content. Low-temperature heat treatment is found to be a suitable for post treatment to clean undesired hydrocarbon residual while increasing the content of the stoichiometric perovskite phase.

For the heat-treated nanoparticles, the OER catalytic activity of the perovskite nanoparticles improved with higher Fe substitution, which is attributed to increasing crystallinity and phase content of the stoichiometric perovskite leading to a larger fraction of the electronically-conductive perovskite structure and therefore enhancing the overall OER activity. Also, a higher content of low-coordinated oxygen species, surface carbonates, and a lower degree of surface-defective structures could be associated with the increasing OER activity at higher Fe contents.

Overall, the results in this thesis highlight that not only nanosized perovskites but also Brownmillerites, Ruddlesden–Popper-type phase and other complex perovskite can be synthesized with spray-flame method based on the synthesis–material and material–property relationships suggested in the individual chapters.

8 References

1. Izadkhah, B., Niaei, A., Illán-Gómez, M. J., Salari, D., Tarjomannejad, A. & Albaladejo-Fuentes, V. LaBO_3 (B = Mn, Fe, Co, Ni, Cu, and Zn) catalysts for CO + NO reaction. *Industrial and Engineering Chemistry Research* **56**, 3880–3886 (2017).
2. Chiarello, G. L., Rossetti, I., Lopinto, P., Migliavacca, G. & Forni, L. Preparation by flame spray pyrolysis of ABO_3 catalysts for the flameless combustion of methane. *Catalysis Today* **117**, 549–553 (2006).
3. Chiarello, G. L., Grunwaldt, J. D., Ferri, D., Krumeich, F., Oliva, C., Forni, L. & Baiker, A. Flame-synthesized LaCoO_3 -supported Pd. 1. Structure, thermal stability and reducibility. *Journal of Catalysis* **252**, 127–136 (2007).
4. Chiarello, G. L., Ferri, D., Grunwaldt, J. D., Forni, L. & Baiker, A. Flame-synthesized LaCoO_3 -supported Pd. 2. Catalytic behavior in the reduction of NO by H_2 under lean conditions. *Journal of Catalysis* **252**, 137–147 (2007).
5. Heel, A., Holtappels, P., Hug, P. & Graule, T. Flame spray synthesis of nanoscale $\text{La}_{0.6}\text{Sr}_{0.4}\text{Co}_{0.2}\text{Fe}_{0.8}\text{O}_{3-\delta}$ and $\text{Ba}_{0.5}\text{Sr}_{0.5}\text{Co}_{0.8}\text{Fe}_{0.2}\text{O}_{3-\delta}$ as cathode materials for intermediate temperature solid . *Fuel Cells* **10**, 419–432 (2010).
6. Heel, A., Holtappels, P. & Graule, T. On the synthesis and performance of flame-made nanoscale $\text{La}_{0.6}\text{Sr}_{0.4}\text{CoO}_{3-\delta}$ and its influence on the application as an intermediate temperature solid oxide fuel cell cathode. *Journal of Power Sources* **195**, 6709–6718 (2010).
7. Lu, Y., Eyssler, A., Otal, E. H., Matam, S. K., Brunko, O., Weidenkaff, A. & Ferri, D. Influence of the synthesis method on the structure of Pd-substituted perovskite catalysts for methane oxidation. *Catalysis Today* **208**, 42–47 (2013).
8. Lu, Y., Michalow, K. A., Matam, S. K., Winkler, A., Maegli, A. E., Yoon, S., Heel, A., Weidenkaff, A. & Ferri, D. Methane abatement under stoichiometric conditions on perovskite-supported palladium catalysts prepared by flame spray synthesis. *Applied Catalysis B: Environmental* **144**, 631–643 (2014).
9. Karageorgakis, N. I., Heel, A., Bieberle-Hütter, A., Rupp, J. L. M., Graule, T. & Gauckler, L. J. Flame spray deposition of $\text{La}_{0.6}\text{Sr}_{0.4}\text{CoO}_{3-\delta}$ thin films: Microstructural characterization, electrochemical performance and degradation. *Journal of Power Sources* **195**, 8152–8161 (2010).
10. Nakayama, S. LaFeO_3 perovskite-type oxide prepared by oxide-mixing, co-precipitation and complex synthesis methods. *Journal of Materials Science* **36**, 5643–5648 (2001).
11. Colomer, M. T., Fumo, D. A., Juradoa, J. R. & Segadaes, A. M. Non-stoichiometric $\text{La}_{(1-x)}\text{NiO}_{(3-d)}$ perovskites produced by combustion synthesis. *Journal of Materials Chemistry* **9**, 2505–2510 (1999).
12. Gupta, A., Ifeacho, P., Schulz, C. & Wiggers, H. Synthesis of tailored WO_3 and WO_x ($2.9 < x < 3$) nanoparticles by adjusting the combustion conditions in a $\text{H}_2/\text{O}_2/\text{Ar}$ premixed flame reactor. *Proceedings of the Combustion Institute* **33**, 1883–1890 (2011).
13. Tilley, R. J. D. *Perovskites and Related Mixed Oxides Concepts and Applications*. (John Wiley & Sons, Ltd, 2016).
14. Sun, Q., Weng, B., Yin, W.-J., Li, Z., Ge, J. & Yan, Y. Oxide perovskites, double perovskites and derivatives for electrocatalysis, photocatalysis, and photovoltaics. *Energy & Environmental Science* **12**, (2018).
15. Giddey, S. S., Badwal, S. P. S., Hollenkamp, A. F., Bhatt, A. I. & Munnings, C. Emerging electrochemical energy conversion and storage technologies. *Frontiers in Chemistry* **2**, 1–28 (2014).

16. Maris, G. A. Structural transitions induced by charge and orbital ordering in transition metal oxides. (2004).
17. Vullum, P. E., Lein, H. L., Einarsrud, M. A., Grande, T. & Holmestad, R. TEM observations of rhombohedral and monoclinic domains in LaCoO₃-based ceramics. *Philosophical Magazine* **88**, 1187–1208 (2008).
18. Vullum, P. E., Holmestad, R., Lein, H. L., Mastin, J., Einarsrud, M. A. & Grande, T. Monoclinic ferroelastic domains in LaCoO₃-based perovskites. *Advanced Materials* **19**, 4399–4403 (2007).
19. Phelan, D. Constraints on the possible long-range orbital ordering in LaCoO₃. *Journal of Magnetism and Magnetic Materials* **350**, 183–187 (2014).
20. Liu, G., Li, X., Wang, Y., Liang, W., Liu, B., Feng, H., Yang, H., Zhang, J. & Sun, J. Nanoscale domains of ordered oxygen-vacancies in LaCoO₃ films. *Applied Surface Science* **425**, 121–129 (2017).
21. Vasala, S. & Karppinen, M. A₂B'B''O₆ perovskites: A review. *Progress in Solid State Chemistry* **43**, 1–36 (2015).
22. Li, J. Q., Matsui, Y., Park, S. K. & Tokura, Y. Charge ordered states in La_{1-x}Sr_xFeO₃. *Physical Review B* **79**, 297–300 (1997).
23. Lein, H. L., Grande, T., Vullum, P. E., Holmestad, R. & Einarsrud, M. A. TEM observations of rhombohedral and monoclinic domains in LaCoO₃-based ceramics. *Philosophical Magazine* **88**, 1187–1208 (2008).
24. Hansteen, O. H., Fjellvåg, H. & Hauback, B. J. Crystal structure, thermal and magnetic properties of La₃Co₃O₈. Phase relations for LaCoO_{3-δ} (0.00 ≤ δ ≤ 0.50) at 673 K. *Journal of Materials Chemistry* 3–10 (2007).
25. Nowroozi, M. A., Ivlev, S., Rohrer, J. & Clemens, O. La₂CoO₄: A new intercalation based cathode material for fluoride ion batteries with improved cycling stability. *Journal of Materials Chemistry A* **6**, 4658–4669 (2018).
26. Hansteen, O. H., Fjellvåg, H. & Hauback, B. C. Crystal structure and magnetic properties of La₂Co₂O₅. *Journal of Solid State Chemistry* **141**, 411–417 (1998).
27. Britten, J. F., Garlea, V. O., Cranswick, L. M. D., Greedan, J. E., Ramezanipour, F. & Grosvenor, A. P. Intralayer cation ordering in a brownmillerite superstructure: Synthesis, crystal, and magnetic structures of Ca₂FeCoO₅. *Chemistry of Materials* **22**, 6008–6020 (2010).
28. El Shinawi, H., Marco, J. F., Berry, F. J. & Greaves, C. LaSrCoFeO₅, LaSrCoFeO₅F and LaSrCoFeO_{5.5}: new La–Sr–Co–Fe perovskites. *Journal of Materials Chemistry* **20**, 3253 (2010).
29. Tomkiewicz, A. C., Tamimi, M., Huq, A. & McIntosh, S. Oxygen transport pathways in Ruddlesden–Popper structured oxides revealed via in situ neutron diffraction. *Journal of Materials Chemistry A* **3**, 21864–21874 (2015).
30. Jantsky, L., Okamoto, H., Demont, A. & Fjellvåg, H. Tuning of water and hydroxide content of intercalated ruddlesden-popper- type oxides in the PrSr₃Co_{1.5}Fe_{1.5}O_{10-δ} system. *Inorganic Chemistry* **51**, 9181–9191 (2012).
31. Gu, X. K. & Nikolla, E. Design of Ruddlesden-Popper oxides with optimal surface oxygen exchange properties for oxygen reduction and evolution. *ACS Catalysis* **7**, 5912–5920 (2017).
32. Roger, A., Bedel, L., Zimmermann, Y., Kiennemann, A. & Rehspringer, J. La_{1-y}Co_{0.4}Fe_{0.6}O_{3-x} perovskite oxides as catalysts for Fischer–Tropsch synthesis. *Journal of Catalysis* **235**, 279–294 (2005).
33. Druce, J., Téllez, H., Burriel, M., Sharp, M. D., Fawcett, L. J., Cook, S. N., McPhail, D. S., Ishihara, T., Brongersma, H. H. & Kilner, J. A. Surface termination and subsurface restructuring of perovskite-based solid oxide electrode materials. *Energy & Environmental Science* **7**, 3593–3599 (2014).

34. Neagu, D., Tsekouras, G., Miller, D. N., Ménard, H. & Irvine, J. T. S. In situ growth of nanoparticles through control of non-stoichiometry. *Nature Chemistry* **5**, 916–923 (2013).
35. Mueller, D. N., MacHala, M. L., Bluhm, H. & Chueh, W. C. Redox activity of surface oxygen anions in oxygen-deficient perovskite oxides during electrochemical reactions. *Nature Communications* **6**, 1–8 (2015).
36. Jalili, H., Han, J. W., Kuru, Y., Cai, Z. & Yildiz, B. Strain effects on the surface chemistry and electronic structure of $\text{La}_{0.7}\text{Sr}_{0.3}\text{MnO}_3$. *ECS Transactions* **35**, 2097–2104 (2011).
37. Yildiz, B. Stretching the energy landscape of oxides - Effects on electrocatalysis and diffusion. *MRS Bulletin* **39**, 147–156 (2014).
38. Riva, M., Kubicek, M., Hao, X., Franceschi, G., Gerhold, S., Schmid, M., Hutter, H., Fleig, J., Franchini, C., Yildiz, B. & Diebold, U. Influence of surface atomic structure demonstrated on oxygen incorporation mechanism at a model perovskite oxide. *Nature Communications* **9**, 1–9 (2018).
39. Bard, A. J. & Faulkner, L. R. *Electrochemical methods : Fundamentals and applications*. (John Wiley & Sons).
40. Suen, N., Hung, S., Quan, Q., Zhang, N., Xu, Y. & Chen, H. M. Electrocatalysis for the oxygen evolution reaction: Recent development and future perspectives. *Chemical Society Reviews* **46**, 337–365 (2017).
41. Dau, H., Limberg, C., Reier, T., Risch, M., Roggan, S. & Strasser, P. The mechanism of water oxidation: From electrolysis via homogeneous to biological catalysis. *ChemCatChem* **2**, 724–761 (2010).
42. Park, S., Shao, Y., Liu, J. & Wang, Y. Oxygen electrocatalysts for water electrolyzers and reversible fuel cells: Status and perspective. *Energy and Environmental Science* **5**, 9331–9344 (2012).
43. Song, F., Bai, L., Moysiadou, A., Seunghwa, Hu, C., Liardet, L. & Hu, X. Transition metal oxides as electrocatalysts for the oxygen evolution reaction in alkaline solutions: An application-inspired renaissance. *Journal of the American Chemical Society* **140**, 7748–7759 (2018).
44. Suntivich, J., May, K. J., Gasteiger, H. A., Goodenough, J. B. & Shao-Horn, Y. A perovskite oxide optimized for oxygen evolution catalysis from molecular orbital principles. *Science* **334**, 1383–1385 (2011).
45. Hwang, J., Rao, R. R., Giordano, L., Katayama, Y., Yu, Y. & Shao-Horn, Y. Perovskites in catalysis and electrocatalysis. *Science* **358**, 751–756 (2017).
46. Man, I. C., Su, H. Y., Calle-Vallejo, F., Hansen, H. A., Martínez, J. I., Inoglu, N. G., Kitchin, J., Jaramillo, T. F., Nørskov, J. K. & Rossmeisl, J. Universality in oxygen evolution electrocatalysis on oxide surfaces. *ChemCatChem* **3**, 1159–1165 (2011).
47. Morales-Guio, C. G., Liardet, L. & Hu, X. Oxidatively electrodeposited thin-film transition metal (oxy)hydroxides as oxygen evolution catalysts. *Journal of the American Chemical Society* **138**, 8946–8957 (2016).
48. Zhu, H., Zhang, P. & Dai, S. Recent advances of lanthanum-based perovskite oxides for catalysis. *ACS Catalysis* **5**, 6370–6385 (2015).
49. Mefford, J. T., Rong, X., Abakumov, A. M., Hardin, W. G., Dai, S., Kolpak, A. M., Johnston, K. P. & Stevenson, K. J. Water electrolysis on $\text{La}_{1-x}\text{Sr}_x\text{CoO}_{3-\delta}$ perovskite electrocatalysts. *Nature Communications* **7**, 11053 (2016).
50. Stevenson, K. J., Iyer, H., Filimonov, D., Hardin, W. G., Rong, X., Kolpak, A. M., Alexander, C. T., Johnston, K. P., Forslund, R. P., Mefford, J. T. & Abakumov, A. M. Exceptional electrocatalytic oxygen evolution via tunable charge transfer interactions in $\text{La}_{0.5}\text{Sr}_{1.5}\text{Ni}_{1-x}\text{Fe}_x\text{O}_{4\pm\delta}$ Ruddlesden-Popper oxides. *Nature Communications* **9**, 1–11 (2018).

51. Zhang, Q., Doyle, B., Yoo, S., Ding, Y., Xiong, X., Chen, Y., Chen, D., Zhang, L., Zhao, B., Liu, M. & Zhen, D. A tailored double perovskite nanofiber catalyst enables ultrafast oxygen evolution. *Nature Communications* **8**, 14586 (2017).
52. An, L., Zhao, T. S. & Li, Y. S. Carbon-neutral sustainable energy technology: Direct ethanol fuel cells. *Renewable and Sustainable Energy Reviews* **50**, 1462–1468 (2015).
53. Sedighi, M., Ali, A. & Alizadeh, E. Enhanced electro-oxidation of ethanol using Pt-CeO₂ electrocatalyst prepared by electrodeposition technique. *International Journal of Hydrogen Energy* **42**, 4998–5005 (2016).
54. Lavacchi, A., Miller, H. & Vizza, F. *Nanotechnology in Electrocatalysis for Energy*. (Springer-Verlag New York, 2013).
55. Lan, A. & Mukasyan, A. S. Complex SrRuO₃-Pt and LaRuO₃-Pt catalysts for direct alcohol fuel cells. *Industrial & Engineering Chemistry Research* **47**, 8989–8994 (2008).
56. Alvarenga, G. M. & Villullas, H. M. Transition metal oxides in the electrocatalytic oxidation of methanol and ethanol on noble metal nanoparticles. *Current Opinion in Electrochemistry* **4**, 39–44 (2017).
57. López-Atalaya, M., Morallón, E., Cases, F., Vázquez, J. L. & Pérez, J. M. Electrochemical oxidation of ethanol on Pt(hkl) basal surfaces in NaOH and Na₂CO₃ media. *Journal of Power Sources* **52**, 109–117 (1994).
58. Monyoncho, E. A., Ntais, S., Brazeau, N., Wu, J. J., Sun, C. L. & Baranova, E. A. Role of the metal-Oxide support in the catalytic activity of Pd nanoparticles for ethanol electrooxidation in alkaline media. *ChemElectroChem* **3**, 218–227 (2016).
59. Ekrami-Kakhki, M. S., Farzaneh, N. & Fathi, E. Superior electrocatalytic activity of Pt-SrCoO₃ nanoparticles supported on functionalized reduced graphene oxide-chitosan for ethanol oxidation. *International Journal of Hydrogen Energy* **42**, 21131–21145 (2017).
60. Kudas, T. T. & Hampden-Smith, M. J. *Aerosol processing of materials*. (Wiley-VCH, 1999).
61. Menser, J., Kluge, S., Wiggers, H., Dreier, T. & Schulz, C. Approach to standardize a spray-flame nanoparticle synthesis burner. *Proceedings of European Combustion Meeting* **2**, 1–4 (2015).
62. Schneider, F., Suleiman, S., Menser, J., Borukhovich, E., Wlokas, I., Kempf, A., Wiggers, H. & Schulz, C. SpraySyn - A standardized burner configuration for nanoparticle synthesis in spray flames. *Review of Scientific Instruments* **90**, 085108 (2019).
63. Eslamian, M. & Shekarriz, M. Recent advances in nanoparticle preparation by spray and microemulsion methods. *Recent Patents on Nanotechnology* **3**, 99–115 (2009).
64. Teoh, W. Y., Amal, R. & Mädler, L. Flame spray pyrolysis: An enabling technology for nanoparticles design and fabrication. *Nanoscale* **2**, 1324 (2010).
65. Strobel, R. & Pratsinis, S. E. Effect of solvent composition on oxide morphology during flame spray pyrolysis of metal nitrates. *Physical Chemistry Chemical Physics* **13**, 9246–9252 (2011).
66. Grass, R. N. & Stark, W. J. Gas phase synthesis of fcc-cobalt nanoparticles. *Journal of Materials Chemistry* **16**, 1825–1830 (2006).
67. Athanassiou, E. K., Grass, R. N. & Stark, W. J. Large-scale production of carbon-coated copper nanoparticles for sensor applications. *Nanotechnology* **17**, 1668–1673 (2006).
68. Azurdia, J., Marchal, J. & Laine, R. M. Synthesis and characterization of mixed-metal oxide nanopowders along the CoO_x-Al₂O₃ tie line using liquid-feed flame spray pyrolysis. *Journal of the American Ceramic Society* **89**, 2749–2756 (2006).
69. Bickmore, C. R., Waldner, K. F., Treadwell, D. R. & Laine, R. M. Ultrafine spinel powders by flame spray pyrolysis of a magnesium aluminum double alkoxide. *Journal of the American Ceramic Society* **79**, 1419–1423 (1996).

70. Marchal, J., John, T., Baranwal, R., Hinklin, T. & Laine, R. M. Yttrium aluminum garnet nanopowders produced by liquid-feed flame spray pyrolysis (LF-FSP) of metalloorganic Precursors. *Chemistry of Materials* **16**, 822–831 (2004).
71. Chiarello, G. L., Rossetti, I. & Forni, L. Flame-spray pyrolysis preparation of perovskites for methane catalytic combustion. *Journal of Catalysis* **236**, 251–261 (2005).
72. Chiarello, G. L., Rossetti, I., Forni, L., Lopinto, P. & Migliavacca, G. Solvent nature effect in preparation of perovskites by flame-pyrolysis. 1. Carboxylic acids. *Applied Catalysis B: Environmental* **72**, 218–226 (2007).
73. Konnov, A. A. & Dyakov, I. V. Experimental study of adiabatic cellular premixed flames of methane (ethane, propane) + oxygen + carbon dioxide mixtures. *Combustion Science and Technology* **179**, 747–765 (2007).
74. Mueller, R., Mädler, L. & Pratsinis, S. E. Nanoparticle synthesis at high production rates by flame spray pyrolysis. *Chemical Engineering Science* **58**, 1969–1976 (2003).
75. Gröhn, A. J., Pratsinis, S. E., Sánchez-Ferrer, A., Mezzenga, R. & Wegner, K. Scale-up of nanoparticle synthesis by flame spray pyrolysis: The high-temperature particle residence time. *Industrial and Engineering Chemistry Research* **53**, 10734–10742 (2014).
76. Mueller, R., Jossen, R., Pratsinis, S. E., Watson, M. & Kamal Akhtar, M. Zirconia nanoparticles made in spray flames at high production rates. *Journal of the American Ceramic Society* **87**, 197–202 (2004).
77. Gröhn, A. J., Pratsinis, S. E. & Wegner, K. Fluid-particle dynamics during combustion spray aerosol synthesis of ZrO₂. *Chemical Engineering Journal* **191**, 491–502 (2012).
78. Estruch Bosch, C., Copley, M. P., Eralp, T., Bilbé, E., Thybaut, J. W., Marin, G. B. & Collier, P. Tailoring the physical and catalytic properties of lanthanum oxycarbonate nanoparticles. *Applied Catalysis A: General* **536**, 104–112 (2017).
79. Angel, S., Neises, J., Dreyer, M., Friedel Ortega, K., Behrens, M., Wang, Y., Arandiyan, H., Schulz, C. & Wiggers, H. Spray-flame synthesis of La(Fe, Co)O₃ nano-perovskites from metal nitrates. *Inorganic Materials: Synthesis and Processing* **66**, 1–12 (2019).
80. Rosebrock, C. D., Wriedt, T., Mädler, L. & Wegner, K. The role of microexplosions in flame spray synthesis for homogeneous nanopowders from low-cost metal precursors. *Advances in Materials: Inorganic Materials: Synthesis and Processing* **62**, 381–391 (2016).
81. Chiarello, G. L., Rossetti, I., Forni, L., Lopinto, P. & Migliavacca, G. Solvent nature effect in preparation of perovskites by flame pyrolysis. 2. Alcohols and alcohols + propionic acid mixtures. *Applied Catalysis B: Environmental* **72**, 227–232 (2007).
82. Robert M. Silverstein, Francis X. Webster, D. J. K. *Spectrometric identification of organic compounds*. *Journal of Molecular Structure* (Wiley, 2005).
83. Bruker. Attenuated Total Reflection (ATR) – A versatile tool for FT-IR spectroscopy. (2011).
84. Alkan, B., Cychy, S., Varhade, S., Muhler, M., Schulz, C., Schuhmann, W., Wiggers, H. & Andronescu, C. Spray-flame synthesized LaCo_{1-x}Fe_xO₃ perovskite nanoparticles as electrocatalysts for water and ethanol oxidation. *ChemElectroChem* **6**, 4266–4274 (2019).
85. Hiltrop, D., Masa, J., Botz, A. J. R., Lindner, A., Schuhmann, W. & Muhler, M. Micrometer-precise determination of the thin electrolyte layer of a spectroelectrochemical cell by microelectrode approach curves. *Analytical Chemistry* **89**, 4367–4372 (2017).
86. No Author. A short introduction to XRD. (2020). at <<http://www.angstrom-advanced.com/index.asp?page=IntroXRD>>
87. Attfield, M., Barnes, P., Cockcroft, J. K. & Driessen, H. Choice of X-ray Target. (2020). at <<http://pd.chem.ucl.ac.uk/pdnn/inst1/anode.htm>>
88. Atkins, P. & De Paula, J. *Physical Chemistry*. (Oxford University Press, 2006).

89. No Author. X-ray photoemission spectroscopy. (2015). at <<http://www.alux.lu.se/research/synchrotron-radiation-sources/x-ray-photoemission-spectroscopy-xps/>>
90. Mayence, A. *Design and characterization of nanoparticles and their assemblies*. (2016). at <<https://www.diva-portal.org/smash/get/diva2:923226/FULLTEXT01.pdf>>
91. Perrin, C., Menguy, N., Bidault, O., Zahra, C. Y., Zahra, A.-M., Caranoni, C., Hilczer, B. & Stepanov, A. Influence of B-site chemical ordering on the dielectric response of the $\text{Pb}(\text{Sc}_{1/2}\text{Nb}_{1/2})\text{O}_3$ relaxor. *Journal of Physics: Condensed Matter* **13**, 10231–10245 (2001).
92. No Author. Introduction to Mössbauer spectroscopy. (2019). at <<https://www.rsc.org/Membership/Networking/InterestGroups/MossbauerSpect/Intropart1.asp>>
93. McCammon, C. Hyperfine parameters. (2012). at <https://serc.carleton.edu/download/images/35326/hyperfine_parameters.v4.jpg>
94. Gütlich, P. Mössbauer spectroscopy – Principles and applications (lecture). (2005). at <http://www.ak-guetlich.chemie.uni-mainz.de/Dateien/Moessbauer_Lectures.pdf>
95. Fagerlund, G. Determination of specific surface by the BET method. *Matériaux et Constructions* **6**, 239–245 (1973).
96. Waffel, D., Alkan, B., Fu, Q., Chen, Y., Schmidt, S., Schulz, C., Wiggers, H., Muhler, M. & Peng, B. Towards mechanistic understanding of liquid-phase cinnamyl alcohol oxidation with tert-Butyl hydroperoxide over noble-metal-free $\text{LaCo}_{1-x}\text{Fe}_x\text{O}_3$ perovskites. *ChemPlusChem* **84**, 1155–1163 (2019).
97. Parker, V. D. Linear sweep and cyclic voltammetry. *Comprehensive Chemical Kinetics* **26**, 145–202 (1986).
98. Volz, T. J., Hanson, G. R. & Fleckenstein, A. E. Measurement of kinetically resolved vesicular dopamine uptake and efflux using rotating disk electrode voltammetry. *Journal of Neuroscience Methods* **155**, 109–115 (2006).
99. McCrory, C. C. L., Jung, S., Peters, J. C. & Jaramillo, T. F. Benchmarking heterogeneous electrocatalysts for the oxygen evolution reaction. *Journal of the American Chemical Society* **135**, 16977–16987 (2013).
100. Hardt, S., Wlokas, I., Schulz, C. & Wiggers, H. Impact of ambient pressure on titania nanoparticle formation during spray-Flame synthesis. *Journal of Nanoscience and Nanotechnology* **15**, 9449–9456 (2015).
101. Proskurina, N. V., Cherepanov, V. A., Golynets, O. S. & Voronin, V. I. Phase equilibria and structure of solid solutions in the La–Co–Fe–O system at 1100 °C. *Inorganic Materials* **40**, 1093–1097 (2004).
102. Karpinsky, D. V., Troyanchuk, I. O., Bärner, K., Szymczak, H. & Tovar, M. Crystal structure and magnetic ordering of the $\text{LaCo}_{1-x}\text{Fe}_x\text{O}_3$ system. *Journal of Physics: Condensed Matter* **17**, 7219–7226 (2005).
103. Landgrebe, J. D. & Pratsinis, S. E. Gas-phase manufacture of particulates: Interplay of chemical reaction and aerosol coagulation in the free-molecular regime. *Industrial and Engineering Chemistry Research* **28**, 1474–1481 (1989).
104. Momma, K. & Izumi, F. VESTA 3 for three-dimensional visualization of crystal, volumetric and morphology data. *Journal of Applied Crystallography* **44**, 1272–1276 (2011).
105. Busca, G., Finocchio, E., Lorenzelli, V., Trombetta, M. & Rossinib, A. IR study of alkene allylic activation on magnesium ferrite and alumina catalysts. *Journal of the Chemical Society, Faraday Transactions* **92**, 4687–4693 (1996).
106. Teoh, K. H., Ramesh, S. & Arof, A. K. Investigation on the effect of nanosilica towards corn

- starch-lithium perchlorate-based polymer electrolytes. *Journal of Solid State Electrochemistry* **16**, 3165–3170 (2012).
107. Chen, H. S., Kumar, R. V. & Glowacki, B. A. Chemical solution deposited lanthanum zirconium oxide thin films: Synthesis and chemistry. *Materials Chemistry and Physics* **122**, 305–310 (2010).
 108. Sudheendra, L., Seikh, M., Raju, A. R. & Narayana, C. An infrared spectroscopic study of the low-spin to intermediate-spin state ($^1 A_1 - ^3 T_1$) transition in rare earth cobaltates, LnCoO_3 ($\text{Ln} = \text{La}, \text{Pr}$ and Nd). *Chemical Physics Letters* **340**, 275–281 (2001).
 109. Santos, A. F. M., Macedo, L. J. A., Chaves, M. H., Espinoza-Castañeda, M., Merkoçi, A., Limac, F. D. C. A. & Cantanhêde, W. Hybrid self-assembled materials constituted by ferromagnetic nanoparticles and tannic acid: A theoretical and experimental investigation. *Journal of the Brazilian Chemical Society* **27**, 727–734 (2016).
 110. Xu, J., Liu, J., Zhao, Z., Zheng, J., Zhang, G., Duan, A. & Jiang, G. Three-dimensionally ordered macroporous $\text{LaCo}_x\text{Fe}_{1-x}\text{O}_3$ perovskite-type complex oxide catalysts for diesel soot combustion. *Catalysis Today* **153**, 136–142 (2010).
 111. Ngamou, P. H. T., Kohse-Höinghaus, K. & Bahlawane, N. CO and ethanol oxidation over LaCoO_3 planar model catalysts: Effect of the thickness. *Catalysis Communications* **12**, 1344–1350 (2011).
 112. Pegoraro, S., Natile, M. M., Galenda, A. & Glisenti, A. $\text{La}_2\text{Cu}_{0.8}\text{Co}_{0.2}\text{O}_{4+\delta}$ by Pechini Method. *Surface Science Spectra* **16**, 75 (2009).
 113. Milt, V. G., Spreiz, R., Ulla, M. A., Lombardo, E. A. & Fierro, J. L. G. The nature of active sites for the oxidation of methane on La-based perovskites. *Catalysis Letters* **42**, 57–63 (1996).
 114. Kumar, R., Mintz, M. H. & Rabalais, J. W. Surface recoiling, XPS and UPS study of chemisorption of H_2 , O_2 and H_2O on lanthanum. *Surface Science* **147**, 37–47 (1984).
 115. Biesinger, M. C., Payne, B. P., Grosvenor, A. P., Lau, L. W. M., Gerson, A. R. & Smart, R. S. C. Resolving surface chemical states in XPS analysis of first row transition metals, oxides and hydroxides: Cr, Mn, Fe, Co and Ni. *Applied Surface Science* **257**, 2717–2730 (2011).
 116. Yamashita, T. & Hayes, P. Analysis of XPS spectra of Fe^{2+} and Fe^{3+} ions in oxide materials. *Applied Surface Science* **254**, 2441–2449 (2008).
 117. Grosvenor, A. P., Kobe, B. A., Biesinger, M. C. & McIntyre, N. S. Investigation of multiplet splitting of Fe 2p XPS spectra and bonding in iron compounds. *Surface and Interface Analysis* **36**, 1564–1574 (2004).
 118. Bocquet, A. E., Fujimori, A., Mizokawa, T., Saitoh, T., Namatame, H., Suga, S., Kimizuka, N., Takeda, Y. & Takano, M. Electronic structure of $\text{SrFe}^{4+}\text{O}_3$ and related Fe perovskite oxides. *Physical Review B* **45**, 1561–1570 (1992).
 119. Van Der Heide, P. A. W. Systematic x-ray photoelectron spectroscopic study of $\text{La}_{1-x}\text{Sr}_x$ -based perovskite-type oxides. *Surface and Interface Analysis* **33**, 414–425 (2002).
 120. Wu, Y., Cordier, C., Berrier, E., Nuns, N., Dujardin, C. & Granger, P. Surface reconstructions of $\text{LaCo}_{1-x}\text{Fe}_x\text{O}_3$ at high temperature during N_2O decomposition in realistic exhaust gas composition: Impact on the catalytic properties. *Applied Catalysis B: Environmental* **140–141**, 151–163 (2013).
 121. Popescu, I., Wu, Y., Granger, P. & Marcu, I. C. An in situ electrical conductivity study of LaCoFe perovskite-based catalysts in correlation with the total oxidation of methane. *Applied Catalysis A: General* **485**, 20–27 (2014).
 122. Barbosa, A. F. B., Oliveira, V. L., Van Drunen, J. & Tremiliosi-Filho, G. Ethanol electro-oxidation reaction using a polycrystalline nickel electrode in alkaline media: Temperature influence and reaction mechanism. *Journal of Electroanalytical Chemistry* **746**, 31–38 (2015).

123. Zhou, Z. Y., Wang, Q., Lin, J. L., Tian, N. & Sun, S. G. In situ FTIR spectroscopic studies of electrooxidation of ethanol on Pd electrode in alkaline media. *Electrochimica Acta* **55**, 7995–7999 (2010).
124. Hiltrop, D., Masa, J., Botz, A. J. R., Lindner, A., Schuhmann, W. & Muhler, M. Micrometer-Precise Determination of the Thin Electrolyte Layer of a Spectroelectrochemical Cell by Microelectrode Approach Curves. *Analytical Chemistry* **89**, 4367–4372 (2017).
125. Lin, J. L., Ren, J., Tian, N., Zhou, Z. Y. & Sun, S. G. In situ FTIR spectroscopic studies of ethylene glycol electrooxidation on Pd electrode in alkaline solution: The effects of concentration. *Journal of Electroanalytical Chemistry* **688**, 165–171 (2013).
126. Ahmed, M. A., Khafagy, R. M. & El-Sayed, O. Laser-induced down-conversion and infrared phosphorescence emissivity of novel ligand-free perovskite nanomaterials. *Journal of Molecular Structure* **1062**, 133–140 (2014).
127. Ferby, V. A. & Raj, A. M. E. Structural and optical properties of LaCoO₃ nanoparticles prepared through auto-combustion. *Journal of Applied Science and Computations* **5**, 190–198 (2018).
128. Wang, X., Huang, K., Ma, W., Cong, Y., Ge, C. & Feng, S. Defect engineering, electronic structure, and catalytic properties of perovskite oxide La_{0.5}Sr_{0.5}CoO_{3-δ}. *Chemistry - A European Journal* **23**, 1093–1100 (2017).
129. Gholizadeh, A. La_{1-x}Ca_xCo_{1-y}Mg_yO₃ nano-perovskites as CO oxidation catalysts: Structural and catalytic properties. *Journal of the American Ceramic Society* **100**, 859–866 (2017).
130. Farmer, V. C. Differing effects of particle size and shape on the infrared and Raman spectra of kaolinite. *Clay Minerals* **33**, 601–604 (1998).
131. Vallina, B., Rodriguez-Blanco, J. D., Brown, A. P., Blanco, J. A. & Benning, L. G. The role of amorphous precursors in the crystallization of La and Nd carbonates. *Nanoscale* **7**, 12166–12179 (2015).
132. Luisetto, I., Pepe, F. & Bemporad, E. Preparation and characterization of nano cobalt oxide. *Journal of Nanoparticle Research* **10**, 59–67 (2008).
133. Tascón, J. M. D. & Gonzalez Tejuca, L. Adsorption of CO on the perovskite-type oxide LaCoO₃. *Zeitschrift für Physikalische Chemie* **121**, 63–78 (1980).
134. Gangwar, B. P., Palakollu, V., Singh, A., Kanvah, S. & Sharma, S. Combustion synthesized La₂O₃ and La(OH)₃: Recyclable catalytic activity towards Knoevenagel and Hantzsch reactions. *RSC Advances* **4**, 55407–55416 (2014).
135. Tejuca, L. G., Rochester, C. H., Fierro, J. L. G. & Tascón, J. M. D. Infrared spectroscopic study of the adsorption of pyridine, carbon monoxide and carbon dioxide on the perovskite-type oxides LaMO₃. *Journal of the Chemical Society, Faraday Transactions 1* **80**, 1089 (1984).
136. Shannon, R. D. Revised effective ionic radii and systematic studies of interatomic distances in halides and chalcogenides. *Acta Crystallographica Section A* **32**, 751–767 (1976).
137. Vasala, S., Lehtimäki, M., Huang, Y. H., Yamauchi, H., Goodenough, J. B. & Karppinen, M. Degree of order and redox balance in B-site ordered double-perovskite oxides, Sr₂MMoO_{6-δ} (M=Mg, Mn, Fe, Co, Ni, Zn). *Journal of Solid State Chemistry* **183**, 1007–1012 (2010).
138. Rui, X., Chung, D., Papa Lopes, P., Zheng, H., Mitchell, J., Markovic, N. M. & Klie, R. Identical Location STEM analysis on La_{1-x}Sr_xCoO₃ Oxygen-Evolution Catalysts. *Microscopy and Microanalysis* **25**, 2052–2053 (2019).
139. Dhankhar, S., Gupta, K., Bhalerao, G., Shukla, N., Chandran, M., Francis, B., Tiwari, B., Baskar, K. & Singh, S. Anomalous room temperature magnetoresistance in brownmillerite Ca₂Fe₂O₅. *RSC Advances* **5**, 92549–92553 (2015).
140. Rousseau, S., Lorient, S., Delichere, P., Boreave, A., Deloume, J. P. & Vernoux, P. La_(1-x)Sr_xCo_{1-y}Fe_yO₃ perovskites prepared by sol-gel method: Characterization and relationships

- with catalytic properties for total oxidation of toluene. *Applied Catalysis B: Environmental* **88**, 438–447 (2009).
141. Zheng, X. G., Xu, C. N., Nishikubo, K., Nishiyama, K., Higemoto, W., Moon, W. J., Tanaka, E. & Otake, E. S. Finite-size effect on Néel temperature in antiferromagnetic nanoparticles. *Physical Review B - Condensed Matter and Materials Physics* **72**, 1–8 (2005).
 142. Diehm, P. M., Ágoston, P. & Albe, K. Size-dependent lattice expansion in nanoparticles: Reality or anomaly? *ChemPhysChem* **13**, 2443–2454 (2012).
 143. Gu, D., Jia, C. J., Weidenthaler, C., Bongard, H. J., Spliethoff, B., Schmidt, W. & Schüth, F. Highly ordered mesoporous cobalt-containing oxides: Structure, catalytic properties, and active Sites in oxidation of carbon monoxide. *Journal of the American Chemical Society* **137**, 11407–11418 (2015).
 144. Matsumoto, Y. & Sato, E. Electrocatalytic properties of transition metal oxides for oxygen evolution reaction. *Materials Chemistry and Physics* **14**, 397–426 (1986).
 145. Binet, C., Badri, A., Boutonnet-Kizling, M. & Lavalley, J. FTIR study of carbon monoxide adsorption on ceria : CO₂²⁻ carbonate dianion adsorbed species. *Journal of the Chemical Society, Faraday Transactions* **90**, 1023–1028 (1994).
 146. Villalobos, M. & Leckie, J. O. Surface complexation modeling and FTIR study of carbonate adsorption to goethite. *Journal of Colloid and Interface Science* **235**, 15–32 (2001).
 147. Lebedev, O. I., Turner, S., Caignaert, V., Cherepanov, V. A. & Raveau, B. Exceptional layered ordering of cobalt and iron in perovskites. *Chemistry of Materials* **28**, 2907–2911 (2016).
 148. Kundu, A. K., Lebedev, O. I., Volkova, N. E., Seikh, M. M., Caignaert, V., Cherepanov, V. A. & Raveau, B. Quintuple perovskites Ln₂Ba₃Fe_{5-x}Co_xO_{15-y}: Nanoscale ordering and unconventional magnetism. *Journal of Materials Chemistry C* **3**, 5398–5405 (2015).
 149. Kondakindi, R. R., Kundu, A., Karan, K., Peppley, B. A., Qi, A., Thurgood, C. & Schurer, P. Characterization and activity of perovskite catalysts for autothermal reforming of dodecane. *Applied Catalysis A: General* **390**, 271–280 (2010).
 150. Nennung, A., Opitz, A. K., Rameshan, C., Rameshan, R., Blume, R., Hävecker, M., Knop-Gericke, A., Rupprechter, G., Klötzer, B. & Fleig, J. Ambient pressure XPS study of mixed conducting perovskite-type SOFC cathode and anode materials under well-defined electrochemical polarization. *Journal of Physical Chemistry C* **120**, 1461–1471 (2016).
 151. Armelao, L., Bettinelli, M., Bottaro, G., Barreca, D. & Tondello, E. LaCoO₃ Nanopowders by XPS. *Surface Science Spectra* **8**, 24–31 (2001).
 152. Enslin, D., Cherkashinin, G., Schmid, S., Bhuvaneshwari, S., Thissen, A. & Jaegermann, W. Nonrigid band behavior of the electronic structure of LiCoO₂ thin film during electrochemical Li deintercalation. *Chemistry of Materials* **26**, 3948–3956 (2014).
 153. Grenier, J., Pouchard, M. & Hagenmuller, P. Vacancy ordering in oxygen-deficient perovskite-related ferrites. *Structure and Bonding* **47**, 1–25 (1981).
 154. Tambunan, O. T., Parwanta, K. J., Acharya, S. K., Lee, B. W., Jung, C. U., Kim, Y. S., Park, B. H., Jeong, H., Park, J.-Y., Cho, M. R., Park, Y. D., Choi, W. S., Kim, D.-W., Jin, H., Lee, S., Song, S. J., Kang, S.-J., Kim, M. & Hwang, C. S. Resistance switching in epitaxial SrCoO_x thin films. *Applied Physics Letters* **105**, 63507 (2014).
 155. Merino, N. A., Barbero, B. P., Ruiz, P. & Cadús, L. E. Synthesis, characterisation, catalytic activity and structural stability of LaCo_{1-y}Fe_yO_{3±λ} perovskite catalysts for combustion of ethanol and propane. *Journal of Catalysis* **240**, 245–257 (2006).
 156. Jiménez, V. M., Fernández, A., Espinós, J. P. & González-Elipe, A. R. The state of the oxygen at the surface of polycrystalline cobalt oxide. *Journal of Electron Spectroscopy and Related Phenomena* **71**, 61–71 (1995).

157. Duan, Y., Sun, S., Xi, S., Ren, X., Zhou, Y., Zhang, G., Yang, H., Du, Y. & Xu, Z. J. Tailoring the Co 3d-O 2p covalency in LaCoO₃ by Fe substitution to promote oxygen evolution reaction. *Chemistry of Materials* **29**, 10534–10541 (2017).
158. Yan, D., Dong, C.-L., Huang, Y.-C., Zou, Y., Xie, C., Wang, Y., Zhang, Y., Liu, D., Shen, S. & Wang, S. Engineering the coordination geometry of metal–organic complex electrocatalysts for highly enhanced oxygen evolution reaction. *Journal of Materials Chemistry A* **6**, 805–810 (2018).
159. Laurikėnas, A., Barkauskas, J., Reklaitis, J., Niaura, G., Baltrūnas, D. & Kareiva, A. Formation peculiarities of iron (III) acetate: potential precursor for iron metal-organic frameworks (MOFs). *Lithuanian Journal of Physics* **56**, 35–41 (2016).
160. Edwards, D. A. & Hayward, R. N. Transition metal acetates. *Canadian Journal of Chemistry* **46**, 3443–3446 (1968).
161. Petrov, A. N., Cherepanov, V. A. & Zuev, A. Y. Thermodynamics, defect structure, and charge transfer in doped lanthanum cobaltites: An overview. *Journal of Solid State Electrochemistry* **10**, 517–537 (2006).
162. Wang, J., Huang, Z., Tang, C. & Zheng, J. Effect of hydrogen addition on early flame growth of lean burn natural gas-air mixtures. *International Journal of Hydrogen Energy* **35**, 7246–7252 (2010).
163. Dandy, D. S. & Vosen, S. R. Numerical and experimental studies of hydroxyl radical chemiluminescence in methane-air flames. *Combustion Science and Technology* **82**, 131–150 (1992).
164. Lim, T., Niemantsverdriet, J. W. H. & Gracia, J. Layered antiferromagnetic ordering in the most active perovskite catalysts for the oxygen evolution reaction. *ChemCatChem* **8**, 2968–2974 (2016).
165. Grimaud, A., May, K. J., Carlton, C. E., Lee, Y.-L., Risch, M., Hong, W. T., Zhou, J. & Shao-Horn, Y. Double perovskites as a family of highly active catalysts for oxygen evolution in alkaline solution. *Nature Communications* **4**, 1–7 (2013).

9 Appendix

9.1 Characterization results

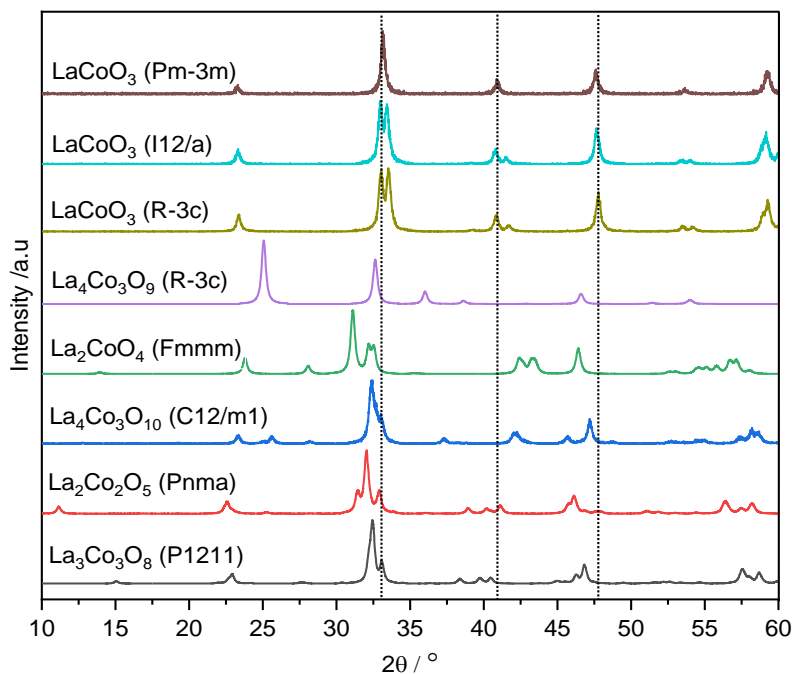


Figure A1: The XRD patterns of perovskite, Ruddlesden Popper and Brownmillerite structures. Space group of each crystallographic phase is given in parenthesis. Despite overlapping of the most diffraction peaks, those at 42.0–45.0 ° can be separately attributed to Ruddlesden Popper structures. Also, the diffraction peaks at about 22.5–23.0° can be separately attributed to Brownmillerite structures.

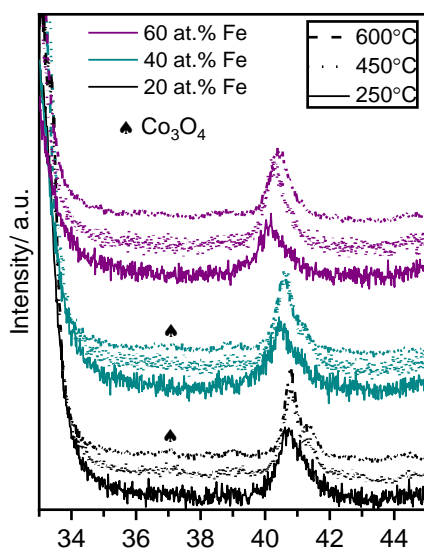
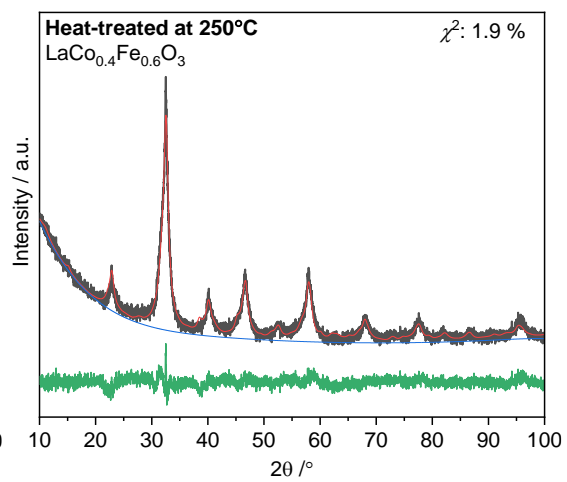
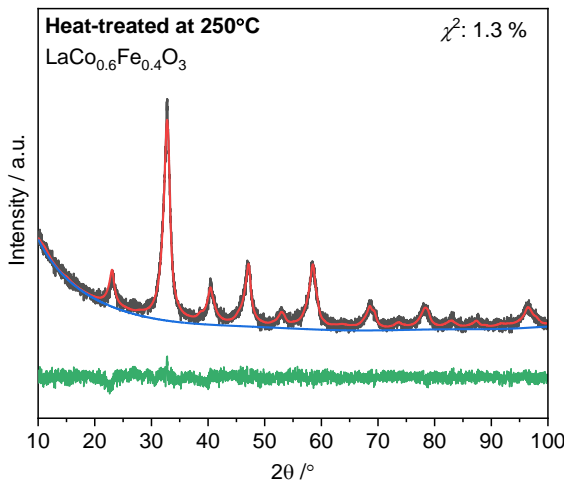


Figure A2: Magnified XRD patterns between 2θ of 35 and 45° in Figure 37b, showing weak diffraction peak of Co₃O₄ phase (ICSD no: 27497) detectable at ~37 °.

Table A1: The reference list of possible crystal structures of perovskite, Ruddlesden-Popper and Brownmillerite phases. The lattice parameter and interplanar spacing values taken from the crystallographic information file of the relevant phases. Note that Fe-substituted Brownmillerite and Ruddlesden-Popper phases are not shown as their crystallographic data is not specified in the database. The abbreviations of O, R, C, M stands for orthorhombic, rhombohedral, cubic and monoclinic crystal structures. The doublet peaks in rhombohedral structures are given as an interval. All information is taken from the ICSD database.

Phases	Crystal structure	Interplanar spacings (d)					
LaCoO _{2.865}	Rh.	2.7587	2.7396	3.8871	1.9442	2.2500	1.5888
LaCoO _{2.982}	Rh.	2.7112	2.6713	3.8066	1.9036	2.2094	1.5581
LaCoO ₃	Cubic	2.7010	-	3.8179	1.9099	2.2052	1.5595
LaCoO ₃	Mono.	2.7154	2.6798	3.8120	1.9077	2.2125	1.5609
La ₂ Co ₂ O ₅	Orth.	2.7938	2.7218	3.9350	1.9672	2.8458	1.5851
La ₃ Co ₃ O ₈	Orth.	2.7560	2.7074	3.8780	1.9396	2.7794	1.5728
La ₄ Co ₃ O ₉	Orth.	2.5522	2.7437	3.5519	1.9490	2.4938	-
La ₄ Co ₃ O ₁₀	Orth.	2.7618	2.7085	3.8130	1.9256	2.7375	1.5858
La ₂ CoO _{4.09}	Orth.	2.8743	2.7519	3.7387	1.9561	2.7811	1.6115
LaCo _{0.8} Fe _{0.2} O ₃	Rh.	2.7249	2.6930	3.8310	1.9155	2.2205	1.5670
LaCo _{0.75} Fe _{0.25} O ₃	Rh.	2.7279	2.6972	3.8360	1.9180	2.2231	1.5690
LaCo _{0.5} Fe _{0.5} O ₃	Rh.	2.7461	2.7155	3.8618	1.9309	2.2380	1.5795
LaCo _{0.5} Fe _{0.5} O ₃	Orth.	2.7265		3.8608	1.9271	2.2270	1.5710
LaCo _{0.4} Fe _{0.6} O ₃	Rh.	2.7535	2.7234	3.8720	1.9368	2.2446	1.5843
LaCo _{0.4} Fe _{0.6} O ₃	Orth.	2.7372		3.8704	1.9368	2.2409	1.5779
LaFeO ₃	Orth.	2.7760 - 2.7695		3.9250	1.9607	2.2658	1.6025



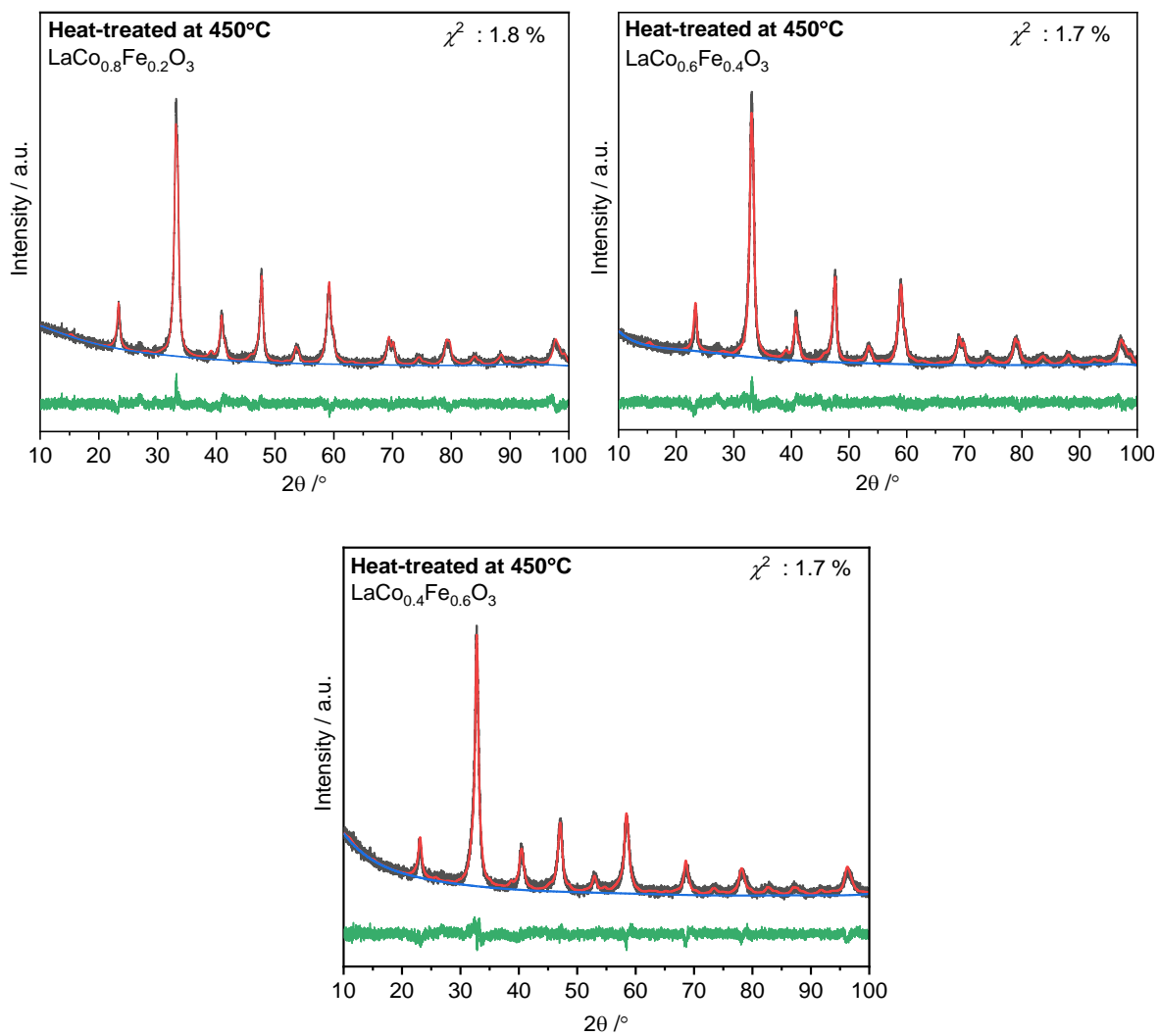


Figure A3: The Rietveld refinement plots of the powder XRD data of 20, 40, and 60 at.% Fe-substituted samples heat-treated at 250 and 450°C. Experimental data was shown as black dots while red, blue and green colors represent the simulated XRD patterns, background and difference curves, respectively. χ^2 represents the goodness-of-fit, which is used to measure convergence of the refinement.

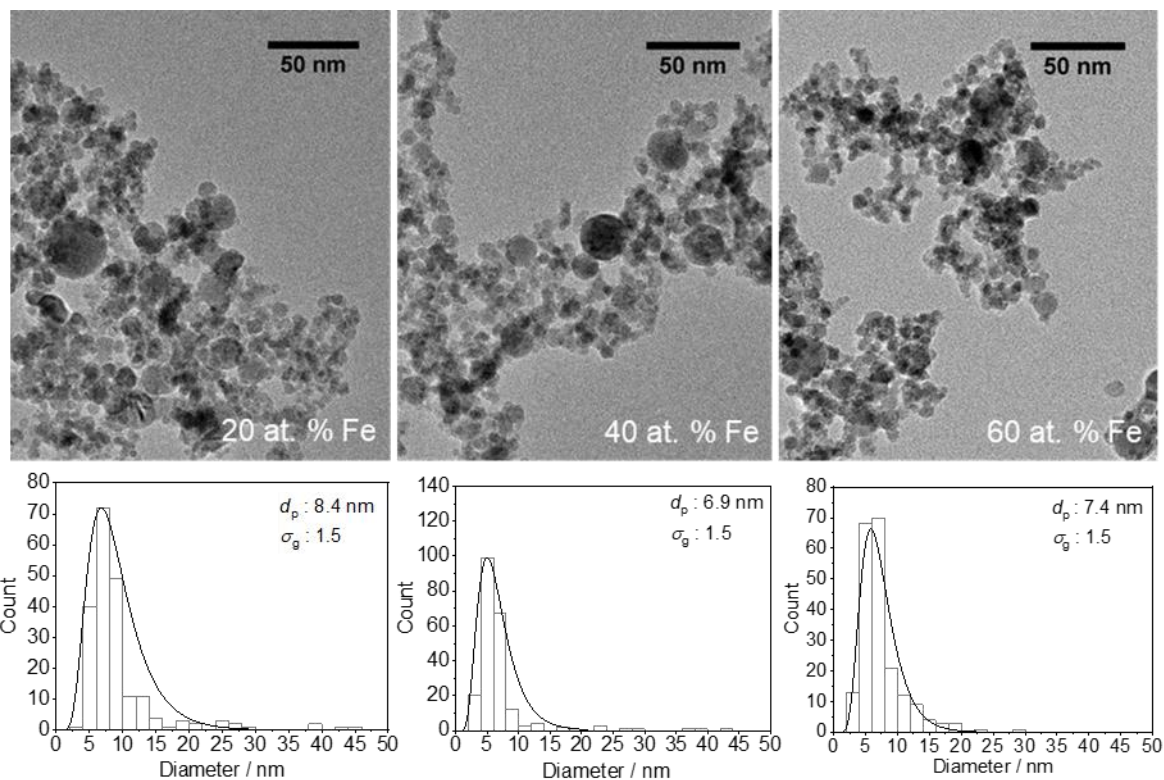


Figure A4: TEM images of the as-prepared nanoparticles at 20, 40, and 60 at.% Fe, showing the agglomerated state of the analyzed nanoparticles. Lognormal fitting of the size distribution histograms shows the number mean particle size and the geometric standard deviations.

Table A2: EDX measurements of the heated samples on single particles using dark-field STEM were made for 15 selected crystallites per sample.

x , $\text{LaCo}_{1-x}\text{Fe}_x\text{O}_3$	TEM	
	Fe/(Fe+Co)	La/(Co+Fe)
0.2	0.19	1.11
0.3	0.28	1.19
0.4	0.39	1.20

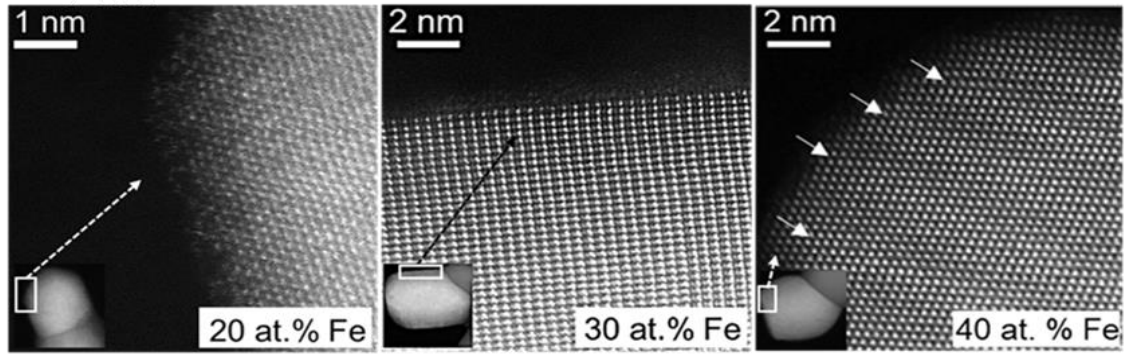


Figure A5: AADF-STEM images showing the atomic arrangements of the bulk and the surface region (heat-treated samples). The white rectangles in the insets indicate the near-surface regions where the atomic structure of perovskites with different Fe content were analyzed. The white solid arrows (right) highlight the nanoscale ordering of a crystallite with 40 at.% Fe.

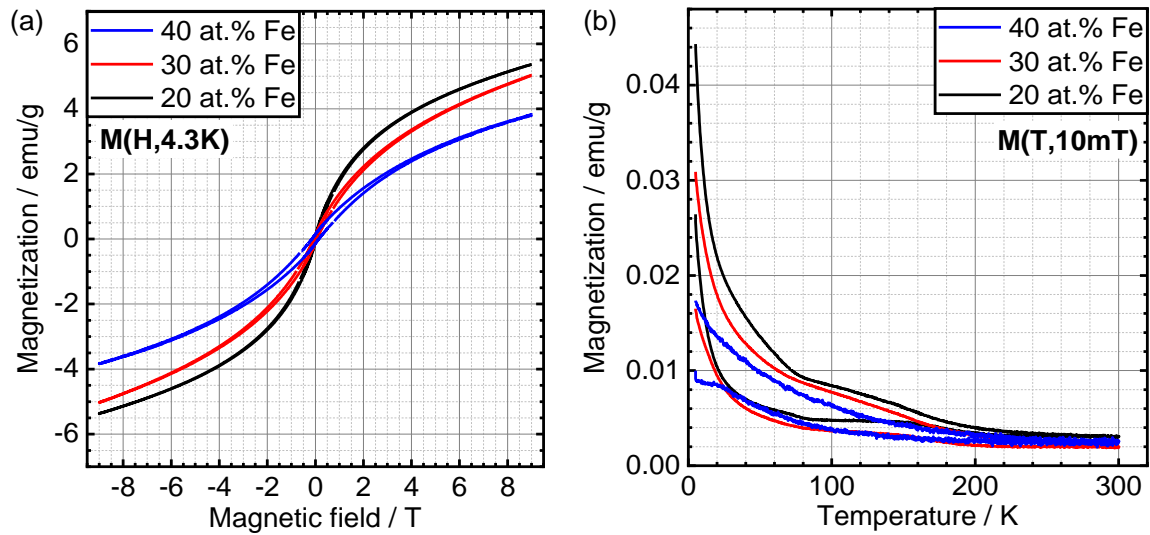


Figure A6: Magnetic field- and temperature-dependent magnetization curves were shown in bottom (a) and (b), respectively. Both curves mainly indicate decreasing magnetization values at increasing Fe contents when they are analyzed at the same magnetic field or heating temperature.

Table A3: The fitted hyperfine parameters calculated from Mößbauer spectra at 4.3K.

$\text{LaCo}_{1-x}\text{Fe}_x\text{O}_{3\pm\delta}$, x	Isomer shift / (mm/s)	Quadrupole splitting / (mm/s)	Magnet hyperfine field, median, / T
0.3 – As-prepared	0.37 (1)	-0.04 (2)	45.5
0.4 – As-prepared	0.36 (1)	-0.03 (1)	47.3
0.2 – heated	0.33(2)	-0.10(4)	39.3
0.3 – heated	0.36(1)	-0.04(2)	44.7
0.4 – heated	0.33(1)	-0.08(3)	46.8

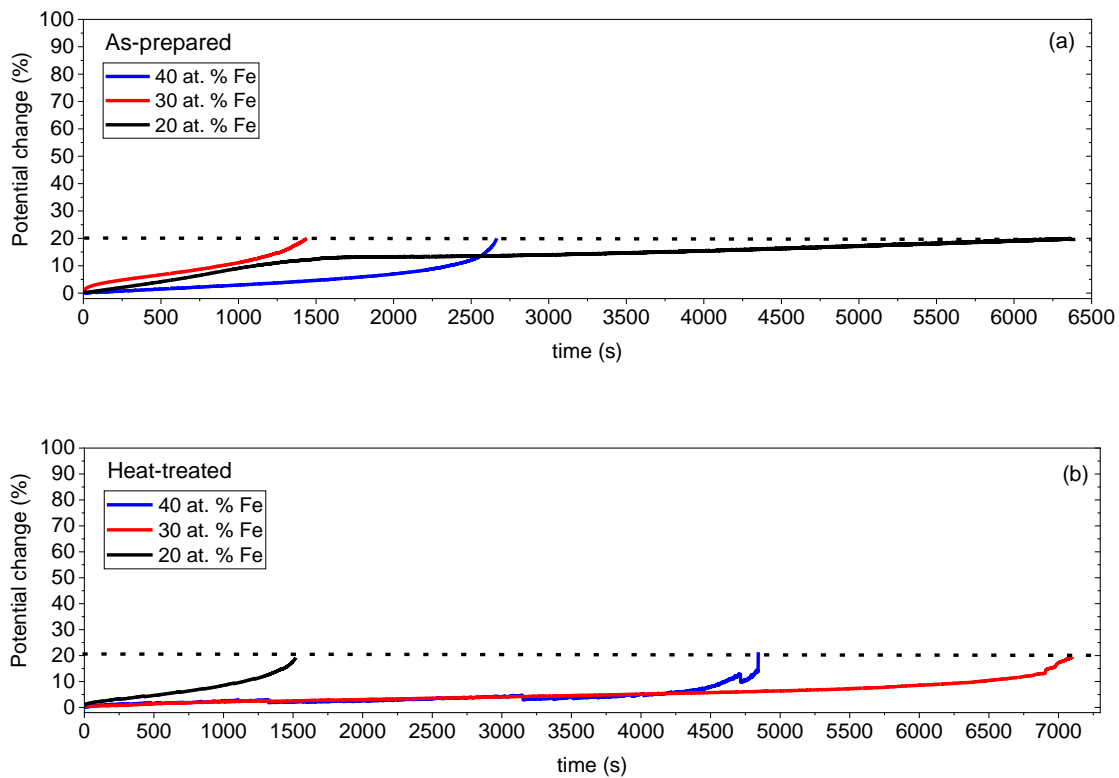


Figure A7: Chronopotentiometric measurement of the as-prepared and heat-treated LaCo_{1-x}Fe_xO₃ perovskites recorded in 1 M KOH using a rotation speed of 1600 rpm and a current density of 10 mA cm⁻².

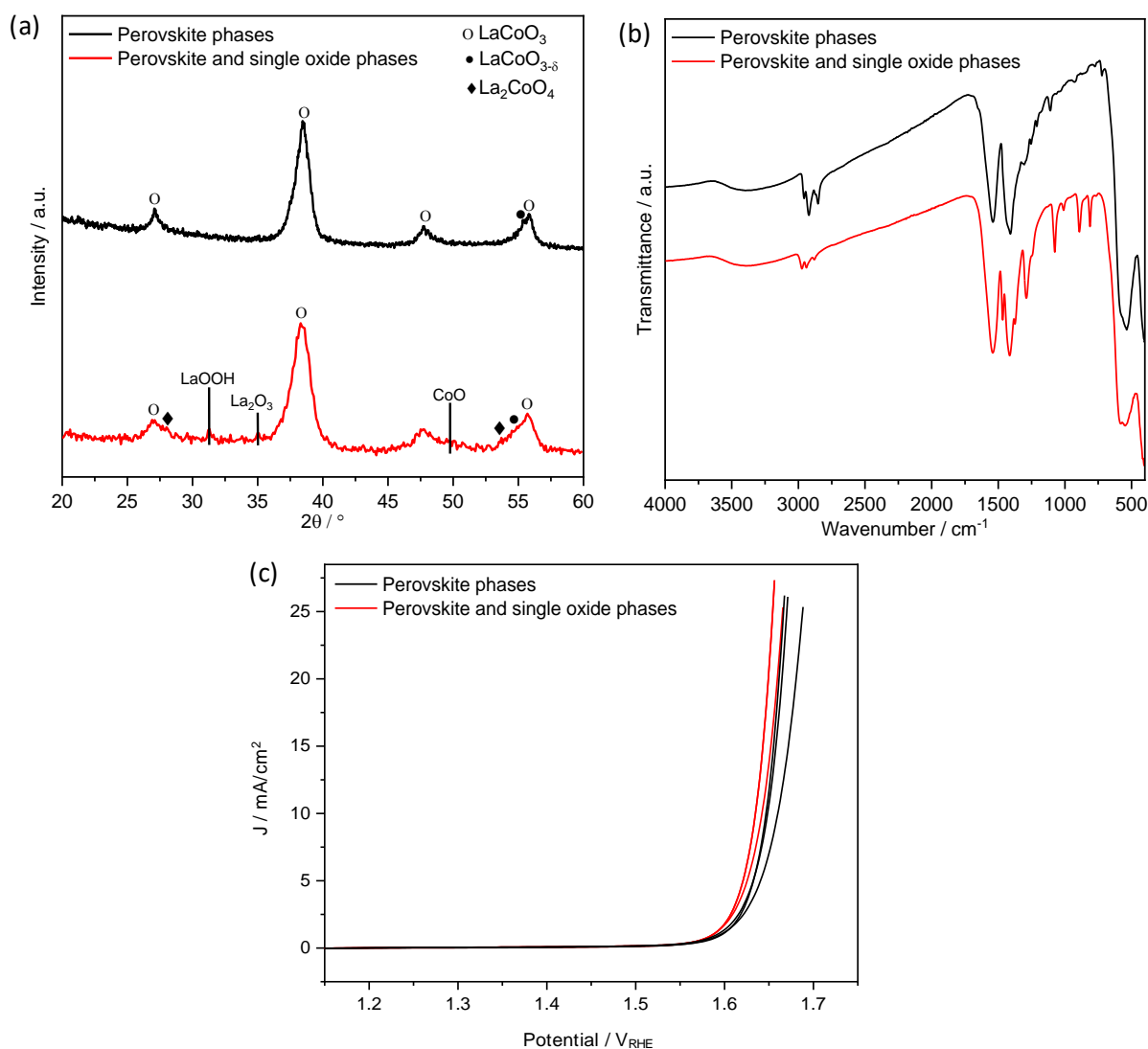


Figure A8: Comparative Co K_α based X-ray diffractograms, FTIR spectra and OER polarization curves of LaCoO₃ nanoparticles. Three curves in the OER plots are visible as a result of the measurement of the samples at three different electrodes. Multiphase LaCoO₃ nanoparticles were synthesized from the propionic acid-based precursor solution studied in Chapter 5.1 whereas perovskite LaCoO₃ nanoparticles were produced from octanoic acid-based solution in Chapter 5.3. Both multiple and perovskite LaCoO₃ samples show the count-mean diameter of approximately 14 nm and the all measurements were made at the same experimental conditions for comparison purposes. Although the perovskite single-oxide phase system shows more carbon impurities based on FTIR patterns (i.e., the band intensity of carbonaceous groups relative to those of metal oxide band is higher in the multiphase system), they exhibit higher OER activity than perovskite-based LaCoO₃ nanoparticles. Due to the similar mean particle size in both material systems, the increase in the OER activity can be originated from the activity of single oxide phases (i.e., most likely from CoO phases as Co-based species are considered active centers).

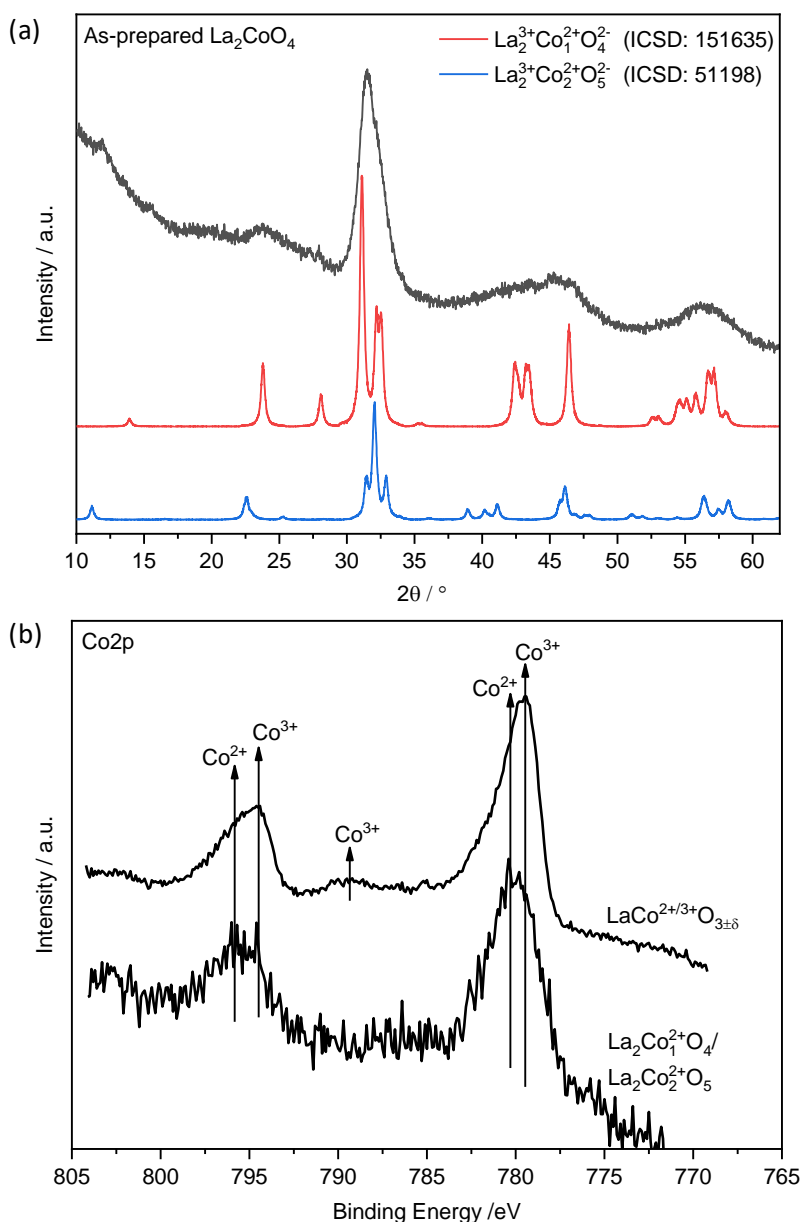


Figure A9: Cu K_α based XRD diffractograms (a) and XPS spectra (b) of as-prepared La_2CoO_4 . To qualitatively compare surface $\text{Co}^{2+}/\text{Co}^{3+}$ ratios, XPS spectra of near-stoichiometric, as-prepared LaCoO_3 is also given in (b). For the synthesis of La_2CoO_4 nanoparticles, precursor solution characteristics were selected as given in Table 10 except that the La/Co precursor ratio was doubled. Process parameters used in the synthesis are the followings; 1 slm of CH_4 and 2 slm of O_2 in pilot flame, 6 slm of dispersion O_2 gas, 170 slm of sheath gas (compressed air), and 170 slm of quench gas (compressed air). The precursor solution was delivered to the reactor with 3 ml/min of flow rate and the pressure inside reactor was kept at 900 mbar. As for the synthesis of near-stoichiometric LaCoO_3 nanoparticles, the propionic acid/1-propanol precursor solution with the total concentration of 0.45 M was used. In the process parameters, the dispersion O_2 gas flow of 8 slm was used at precursor flow rate of 3 ml/min, and all the other synthesis parameters were selected the same to those of La_2CoO_4 . The XRD measurement shows that the as-prepared La_2CoO_4 nanoparticles consist of two main phases, both of which stabilize the Co^{2+} ions in their structure. The high content of surface Co^{2+} ions in $\text{La}_2\text{CoO}_4/\text{La}_2\text{Co}_2\text{O}_5$, as found in the Co 2p spectra, also confirm that Co^{2+} ions are mostly present in this material system.

Table A4: Comparison of the OER activity of $\text{LaCo}_{0.7}\text{Fe}_{0.3}\text{O}_3$ perovskites at as-prepared, and heat-treated state. The OER activity of the perovskites are expressed as the potential at a current density of $+10 \text{ mA/cm}^2$ (E_{OER} at $+10 \text{ mA cm}^{-2}$ vs. reversible hydrogen electrode (V_{RHE})) showing that heating the as-prepared sample at 250°C under O_2 and vacuum has a positive effect on the OER activity. Note that as-shown $\text{LaCo}_{0.7}\text{Fe}_{0.3}\text{O}_3$ perovskites were synthesized with the same process parameters and process parameters shown in Table 10 except that total concentration of La, Co and Fe was selected as 0.45 M.

Perovskite composition (post-treatment)	E_{OER} at + 10 mA cm^{-2} (vs. V_{RHE})	E_{OER} at + 10 mA cm^{-2} (vs. V_{RHE})	E_{OER} at + 10 mA cm^{-2} (vs. V_{RHE})	Average E_{OER} at + 10 mA cm^{-2} (vs. V_{RHE})	Error (V_{RHE})
$\text{LaCo}_{0.7}\text{Fe}_{0.3}\text{O}_3$ (as-prepared)	1.617	1.622	1.623	1.621	0.00321
$\text{LaCo}_{0.7}\text{Fe}_{0.3}\text{O}_3$ (heat-treated at 250°C in O_2)	1.611	1.612	1.611	1.611	0.00058
$\text{LaCo}_{0.7}\text{Fe}_{0.3}\text{O}_3$ (heated-treated at 270°C in vacuum $\sim 10 \text{ mbar}$)	1.613	1.605	1.605	1.608	0.00462

Acknowledgement

This work was done at the Institute for Combustion and Gas Dynamics – Reactive Fluids (IVG-RF) at the University of Duisburg-Essen and funded by the Deutsche Forschungsgemeinschaft (DFG, German Research Foundation) within the collaborative research center/transregio 247 “Heterogeneous Oxidation Catalysis in the Liquid Phase”. I was additionally supported by the International Max Planck Research School for Interface Controlled Materials for Energy Conversion (IMPRS-SURMAT).

Without the help of countless people at the University of Duisburg-Essen and the Ruhruniversität Bochum, this work would not have been possible. I would like to take this opportunity to express my sincere thanks. I would like to emphasize a few people in particular.

I would like to thank the head of the IVG-RF and the first supervisor for my work, Prof. Dr. Christof Schulz, for the opportunity to write this work at his institute and the freedom I was able to enjoy. I would also like to thank Prof. Dr. Hartmut Wiggers, the head of the IVG’s nanoparticle group and the supervisor of my work for the good cooperation and everything he has made possible for me in recent years. I would also like to thank both of them for providing excellent equipment at the institute.

I want to thank my second supervisor, Prof. Dr. Martin Muhler, and Prof. Dr. Wolfgang Schuhmann for giving me great insight through discussions in scientific meetings and for their guidance during the progress of my research. Similarly, I thank Dr. Karina Elumeeva, Prof. Dr. Corina Andronescu and Danae Medina at the Ruhruniversität Bochum for their good cooperation and enabling the electrochemical studies of spray-flame-synthesized nanoparticles. I would like to thank Prof. Dr. Heiko Wende, Dr. Joachim Lander, and Dr. Soma Salamon in Experimental Physics Department at the University of Duisburg-Essen for their excellent collaboration in the magnetic characterization studies of the nanoparticles within this project. I also thank Alexander Tarasov (IVG-RF) for enabling heat-treatment of nanoparticles in oxygen atmosphere.

I gratefully thank Dr. Markus Heidelmann, and Dr. Ulrich Hagemann and the all other members of the Interdisciplinary Center for Analytics on the Nanoscale (ICAN) for their help in the TEM and XPS measurements and analyses. Likewise, I thank Prof. Dr. Markus Winterer and his working group for enabling XRD measurements in the Nanoparticle Process Technology laboratory (NPPT) at the University of Duisburg-Essen. I thank Benjamin Breitbach for the XRD measurement at the Max Planck Institute for Iron Research.

I also thank Dipl.-Phys.-Ing. Ludger Jerig (IVG-RF) and the staff of the workshops for design and manufacturing of parts of the experimental facility. I thank Dr.-Ing. Erdal Akyildiz, Dr. Mohaned Hammad, Beate Endres and all other colleagues at IVG-RF for friendship, guidance, and scientific discussions. I also thank all my friends and colleagues at IMPRS-SURMAT as well as those in the collaborative research center/transregio 247 for all sorts of amusements besides my work. Above all, I thank my family for their patience, for always making me feel welcome, and for the one or other piece of advice for life.

DuEPublico

Duisburg-Essen Publications online

UNIVERSITÄT
DUISBURG
ESSEN

Offen im Denken

ub | universitäts
bibliothek

Diese Dissertation wird über DuEPublico, dem Dokumenten- und Publikationsserver der Universität Duisburg-Essen, zur Verfügung gestellt und liegt auch als Print-Version vor.

DOI: 10.17185/duepublico/71937

URN: urn:nbn:de:hbz:464-20200708-074548-0

Alle Rechte vorbehalten.